Effects of SDS and PEO-PPO Block Copolymer on Morphology of ZnO Particles and Its Optical Properties

Nureeyah Samaele

A Thesis Submitted in Partial Fulfillment of the Requirements

for the Degree of Master of Science in Chemical Studies

Prince of Songkla University

2010

Copyright of Prince of Songkla University

Thesis Title	Effects of SDS and PEO-PPO Block Copolymer on Morphology of ZnO Particles and Its Optical Properties
Author	Miss Nureeyah Samaele
Major Program	Chemical Studies

Major Advisor:

…….....
(Asst. Prof. Dr.Pongsaton Amornpitoksuk)

Co-advisor:

…….....
(Asst. Prof. Dr.Sumetha Suwanboon)

Examining Committee:

……..……...Chairperson
(Dr.Tanakorn Ratana)

…..…….....
(Asst. Prof. Dr.Pongsaton Amornpitoksuk)

…..…….....
(Asst. Prof. Dr.Sumetha Suwanboon)

…..…….....
(Dr.Nararak Leesakul)

The Graduate School, Prince of Songkla University, has approved this thesis as partial fulfillment of the requirement for the Master of Science Degree in Chemical Studies.

….…….....
(Assoc. Prof. Dr.Krerkchai Thongnoo)
Dean of Graduate School

ชื่อวิทยานิพนธ์	อิทธิพลของ SDS และบล๊อคโคพอลิเมอร์ PEO-PPO ต่อสัณฐานของอนุภาค ZnO และสมบัติเชิงแสง
ผู้เขียน	นางสาวนูรียะห์ สะมะแอ
สาขาวิชา	เคมีศึกษา
ปีการศึกษา	2552

บทคัดย่อ

งานวิจัยนี้ได้ทำการเตรียมอนุภาคซิงค์ออกไซด์จากสารละลายซิงค์อะซิเตตไดไฮเดรตในสภาวะที่มีการเติมโซเดียมโดเดซิลซัลเฟต ซึ่งเป็นสารลดแรงตึงผิวที่มีประจุลบหรือโพลี(เอทีลีนออกไซด์)-บล็อค-โพลี(โพรพีลีนออกไซด์) โคพอลิเมอร์ และโซเดียมไฮดรอกไซด์ที่อุณหภูมิ 70 องศาเซลเซียส โดยทำการศึกษาผลของการเปลี่ยนแปลงสัณฐานในช่วงพีเอช 8 ถึง 12 จากการทดลองพบว่าเมื่อใช้ SDS เป็นสารลดแรงตึงผิว ผงที่เตรียมได้แสดงเฟสซิงค์ออกไซด์บริสุทธิ์เมื่อเตรียมจากสารละลายที่มีพีเอช 12 เท่านั้น หลังจากทำการเผาแคลไซน์ที่อุณหภูมิ 900 องศาเซลเซียส ซิงค์ออกไซด์ที่เตรียมจากสารละลายที่พีเอช 8 และ 10 มีรูปร่างเป็นพีระมิดหกเหลี่ยม เนื่องจากการยับยั้งการเติบโตในแนวแกนซี ในขณะที่ซิงค์ออกไซด์รูปร่างคล้ายแท่งจะปรากฏเมื่อพีเอชของสารละลายเพิ่มขึ้นเป็น 12 กรณีที่ใช้ PEO-*b*-PPO บล็อคโคพอลิเมอร์เป็นสารเพิ่มเสถียรภาพ พบว่าซิงค์ออกไซด์มีรูปร่างเป็นพีระมิดคู่ฐานหกเหลี่ยม รูปร่างคล้ายรักบี้โคน และรูปร่างคล้ายสามเหลี่ยมเมื่อเตรียมผงซิงค์ออกไซด์จากสารละลายที่มีค่าพีเอช 8, 10 และ 12 ตามลำดับ นอกจากนี้ยังพบว่าค่าช่องว่างระหว่างแถบพลังงานและพีกของการแปล่งแสงจะขึ้นกับรูปร่างและขนาดของอนุภาคซิงค์ออกไซด์

Thesis Title	Effects of SDS and PEO-PPO Block Copolymer on Morphology of ZnO Particles and Its Optical Properties
Author	Miss Nureeyah Samaele
Major Program	Chemical Studies
Academic Year	2009

ABSTRACT

ZnO particles were synthesized from an aqueous solution of zinc acetate dihydrate ($Zn(C_2H_3O_2)_2.2H_2O$) in a presence of sodium dodecyl sulfate (SDS) as an anionic surfactant or poly(ethylene oxide)-*b*-poly(propylene oxide) (PEO-*b*-PPO) copolymer, and sodium hydroxide at 70 ^oC. The morphological changes were investigated in the range of pH 8 - 12. In case of SDS used, only a single phase of ZnO formed when preparing the powder from the solution with a pH value of 12. After calcining at 900 ^oC, ZnO particles prepared from the precursor solution at pH 8 and 10 had a hexagonal prism-like shape owing to an inhibition of growth along *c*-direction, whereas a small rod-like structure was shaped when the pH value of precursor solution was increased to 12. In case of PEO-*b*-PPO copolymer used, ZnO structure tended to form a biprimatic, rugby cone and triangle-like structure when preparing ZnO particles from the precursor solution with a pH value of 8, 10 and 12, respectively. Furthermore, it had been found that the estimated band gap value and the emission peak were dependent upon the geometrical shape and size of the ZnO particles.

CONTENTS

CONTENTS (CONTINUED)

Page

LIST OF TABLES

Table **Page**

LIST OF FIGURES

LIST OF FIGURES (CONTINUED)

LIST OF FIGURES (CONTINUED)

LIST OF FIGURES (CONTINUED)

LIST OF FIGURES (CONTINUED)

Figure **Page**

LIST OF FIGURES (CONTINUED)

LIST OF FIGURES (CONTINUED)

CHAPTER 1

INTRODUCTION

1.1. Nanomaterials

Nanotechnology is a collective definition referring to design, characterization, production and application of structures, devices and systems by controlling shape and size at nanometer scale. The prefix "nano" which is derived from the Greek word for dwarf, means a one thousand millionth of a meter or 10^{-9} meters. Generally, nanomaterials have structured the components with at least one dimension less than 100 nm (Holister *et al*., 2003).

Nanostructures can be classified into three groups depending upon the confinement of particles in a particular crystallographic direction within a structure. The three groups are (Cao, 2004):

1. Zero-dimensional (0D) nanostructure: the materials that confine electrons in three dimensions or the structure does not permit free particle motion in any direction. Semiconductor quantum dots, nanoparticles and colloidal particles are some examples in this group.

2. One-dimensional (1D) nanostructure: the materials that confine electrons in two dimensions or the structure does not permit free particle motion in two dimensions. Some examples are nanorods, nanowires, nanotubes and nanofilaments etc.

3. Two-dimensional (2D) nanostructure: the materials exhibit a confinement of electrons in one dimension or the structure does not permit free particle motion in one dimension, such as nano discs or platelets, thin film on a surface and multilayered material.

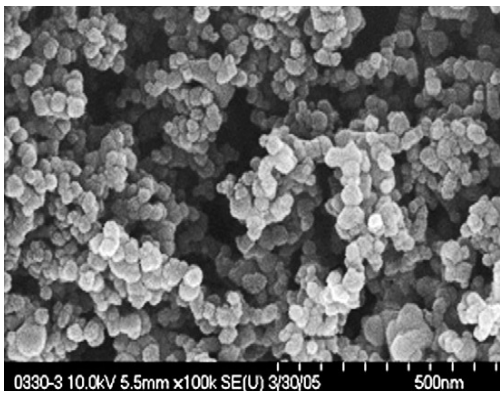

(a)

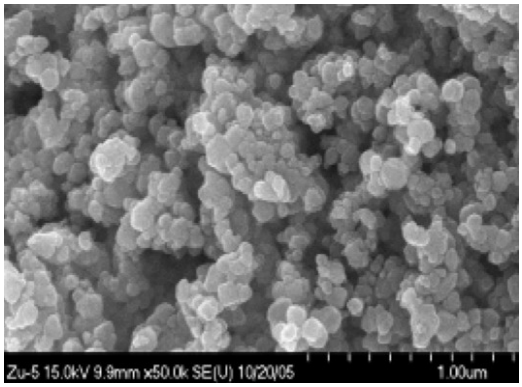

(Kim *et al*., 2006)

(Wahab *et al*., 2008)

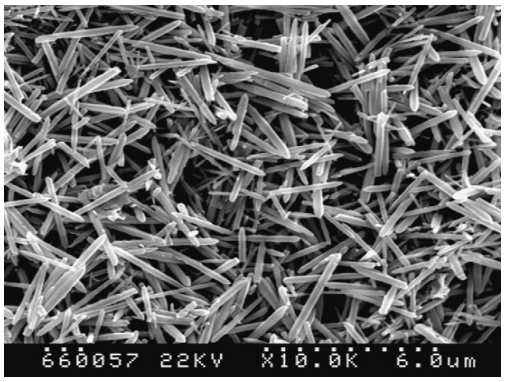

(b)

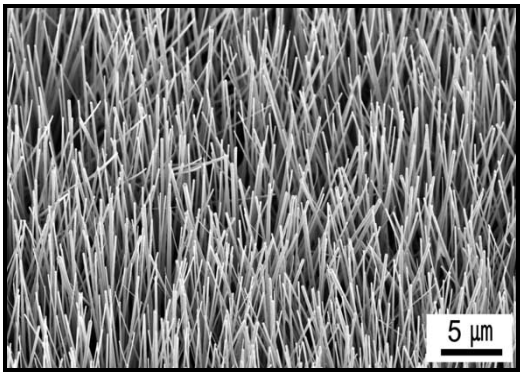

(Li *et al*., 2003)

(Lyu *et al*., 2002)

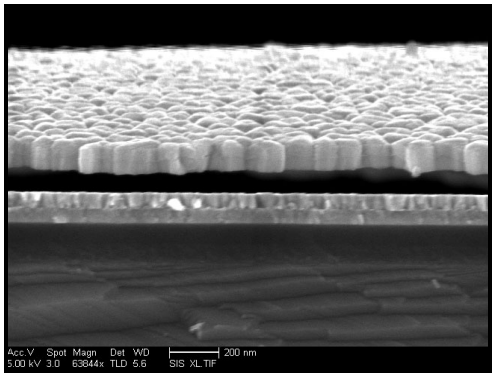

(c)

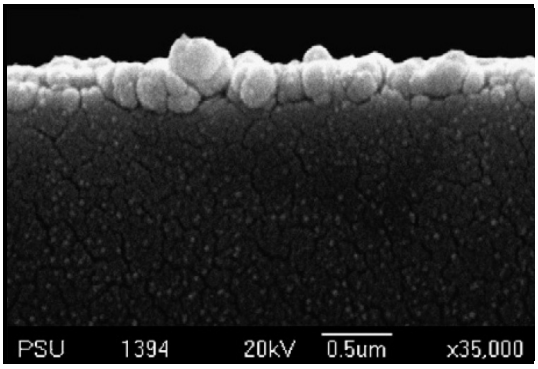

(Chen *et al*., 2007)

(Ratana *et al*., 2009)

Figure 1. Examples of (a) zero-dimentional (0D), (b) one-dimentional (1D) and (c) two-dimentional (2D) nanostructures.

1.2. General description of ZnO

As far as nanomaterial is concerned, ZnO is one of the candidate which has been attracting attention due to its numerous interested properties.

Zinc oxide is a chemical compound with the formula ZnO. It is produced by two main different processes. In the direct or American method, zinc ores (or residues) are heated in air with a coke or anthracite, and the resulting zinc vapour is subjected to controlled oxidation. In the indirect or French method, the zinc vapour to be oxidized is obtained by boiling zinc (http://en.wikipedia.org/wiki/zinc-oxide).

ZnO is nearly insoluble in acids and bases. It characterizes as a white powder commonly known as zinc white. It occurs in nature as the mineral zincite. Crystalline ZnO exhibits the piezoelectric effect and ZnO performs a thermochrome characteristic by changing from white to yellow when heating, and vice versa. The ZnO has been widely studied since 1935. ZnO is a well-known semiconductor with a wide direct band gap (3.37 eV) and large exciton binding energy of about 60 meV at room temperature (http://en.wikipedia.org/wiki/zinc-oxide).

ZnO powder has been commonly used for over a hundred years in a wide range of applications, for example,

1. Pigment

Over the past century, the paint industry (in its constant development of improved products) has utilized various aspects of those properties to high degree. Manufacturers discovered that they could produce the coatings of brushing consistency and good suspension properties by incorporation of ZnO into their pastes.

Zinc white is used as a pigment in paints. In general, zinc white is more opaque than lithopone, but it is less opaque than titanium dioxide. It is also used in coating for paper. Chinese white is a special grade of zinc white used in artists' pigments, because it can absorb both UVA and UVB rays of ultraviolet light. Interestingly, the current state-of-the-art thermal control coatings (TCCs) system utilizes ZnO pigment to maintain solar reflectance over a long exposure time (http://cat.inist.fr/?aModele=afficheN&cpsidt=15369294).

2. Medical applications

A mixture of ZnO and 0.5% Fe_2O_3 (calamine) is used in calamine lotion and a mixture of ZnO and eugenol (zinc oxide eugenol) has restorative and prosthodontic applications in dentistry (http://en.wikipedia.org/wiki/zinc-oxide). Moreover, the ZnO nanopowders can use as antimicrobial agent (Mungkornasawakul *et al*., 2005).

3. Cosmetic applications

ZnO is applied in cosmatics to protect the UV radiation for human (Samontha *et al*). ZnO can be used in ointments, creams, and lotions to protect against sunburn and other damages to the skin caused by ultraviolet light. It is the broadest spectrum UVA and UVB absorber that is approved for use as a sunscreen by the Food and Drug Administration (FDA), and is completely photostable and it is also a main ingredient of mineral make up (http://www.goldbamboo.com/topic-t4989-a1-6Zinc_Oxide.html).

4. Rubber manufacture

ZnO proved the most effective activator to speed up the rate of cure with the new accelerators. It provides a reinforcement in natural rubber, and in some synthetic elastomers such as polysulfides and chloroprenes. The degree of reinforcement depends upon a combination of the particle size, the finest size being

the most effective. ZnO is the chemical reactivity that utilized to activate the organic accelerator. The unreacted portion of ZnO remains available as a basic reserve to neutralize the sulfur-bearing acidic decomposition products formed during vulcanization. Adequate levels of ZnO contribute markedly to chemical reinforcement, scorch control, resistance to heat-aging and compression fatigue. Additional ZnO also provides heat conduction to more rapidly dissipate the heat and thereby provides lower operating temperatures. In addition, it imparts heat stabilization by reacting with acidic decomposition products (http://navbharat.co.in/clients.htm).

5. Plastic applications

Zinc compounds can provide a variety of properties in plastic field. Heat resistance and mechanical strength are imparted to acrylic composites by ZnO. Addition of ZnO to epoxy resins cured with aliphatic polyamines imparts higher tensile strength and water resistance. ZnO is also useful in the preparation of nylon polymers and in increasing their resistance and ZnO react can with unsaturated polyesters to form a higher viscosity and a thixotropic body. ZnO increases the transparency of poly (chlorofluoro ethylene) molding resin. Polyolefin's are improved in color, tensile strength, and vulcanization properties by addition of ZnO. Applications in development for zinc oxide-stabilized polypropylene and high-density polyethylene include safety helmets, stadium seating, insulation, pallets, bags, fibers and filaments agricultural and recreational equipments (http://navbharat.co.in/clients.htm).

6. Food additives

ZnO is added to many breakfast cereals acting as a source of zinc that is a necessary nutrient for ZnO based medicament for preventing and treating diarrhea in farm animals (http://www.freepatentsonline.com/EP1593381.html). (http://en.wikipedia.org/wiki/zinc-oxide).

7. Electronic applications

The most common applications of ZnO are in laser diodes and light emitting diodes (LEDs) since it has an exciton and biexciton binding energies of 60 meV and 15 meV, respectively. Additional it is inexpensive. Most ZnO is an *n*-type semiconductor even in the absence of intentional doping. The native defects such as oxygen vacancies or zinc interstitials are often assumed to be the origin of this, but the subject remains controversial. The *n*-type doped films are often used in the thin film technology, where ZnO serves as a transparent conducting oxide (TCO). The *n*-type doping is possible by introduction of group III elements such as Al, Ga or In. These group III elements can generate the donor state near the conduction band and they can generate the excess electrons at the bottom of conduction band. On the contrary, it is difficult to dope ZnO as a *p*-type semiconductor due to the high activation energy of acceptor, low solubility of acceptor dopants and self-compensating process on acceptor doping caused by intrinsic defects. Recently, the strategy of *p*-type ZnO semiconductor is an active area of research. Thin-film solar cells, liquid crystal display (LCD) and flat panel displays are typical applications of *p*-type ZnO semiconductor material. Appropriately doped ZnO may be transparent and conductive, and they can therefore be used as a transparent conducting oxide in some important devices in place of indium doped tin oxide (ITO) material. Beside, conducting ZnO material is a good infrared reflectors and can be used as energy efficent windows that require high reflective index and high transmittance in the visible range. (http://www.eurekalert/pab.releases/2007.01/uoc--clfo10207.html) (http://en.wikipedia.org/wiki/zinc-oxide)

8. Sensor applications

ZnO can use for pyroelectric sensors. It possesses the advantages of being integrable with on-chip circuitry, un-cooled detecting, room-temperature operation, fast and wide spectral response with high sensitivity and low cost (Hsiao *et al*., 2008).

ZnO material can be used in ensing and/or monitoring the different types of gases both toxic and harmful gases as chlorine (Cl_2) due to it low cost, high sensitivity, excellent selectivity quick response behavior, sulfur hexafluoride, butane, ethanol and gasoline (Majumder *et al*., 2003; Xu *et al*., 2000; Xinshu *et al*., 2004).

1.3. Crystallographic data of ZnO

ZnO exists in three forms depending on pressure. At ambient pressure, ZnO is in the stable hexagonal wurtzite (ZnO_W) form and some ZnO is in the metastable cubic zinc-blend (ZnO_{ZB}) form. At moderate and high pressure (8-10 GPa), ZnO is in the rock-salt (ZnO_{RS}) form. The difference between the critical pressure for the ZnO_{ZB} to ZnO_{RS} and ZnO_W to ZnO_{RS} transition is very small and so the energy difference between ZnO_W and ZnO_{RS} is also very small. Thus, the ZnO_W to ZnO_{RS} transition can occur due to the topotactic transformation based on the network of oxygen and zinc (Qteish, 2000; Serrano *et al*., 2004)

At ambient pressure and temperature, ZnO crystallizes in the wurtzite (*B4* type) structure whose underlying the Bravais lattice in hexagonal (space group $P6_3mc = C^4_{6v}$). The structure of ZnO is illustrated in figure 2. Under ambient condition, the lattice parameters are a = 3.2489 (1) Å and c = 5.2053 (4) Å. Both kinds of atoms are located in Wyckoff position:

$$2(b) = \frac{1}{3}\frac{2}{3}v,\ \frac{2}{3}\frac{1}{3}\ v+\frac{1}{2}$$

and the arrangements are in the positions:

$$\text{Zn: } 000,\ \frac{1}{3}\frac{2}{3}\frac{1}{2}$$

$$\text{O: } 00u,\ \frac{1}{3}\frac{2}{3}u+\frac{1}{2}$$

In an ideal wurtzite crystal, the axial ratio $c/a = (8/3)^{1/2}$ and $u = 3/8$. Experimentally, the real values of u and c/a of wurtzite ZnO were, however, determined in the range of $u = 0.3817$ to 0.3856 and $c/a = 1.593$ to 1.6035.

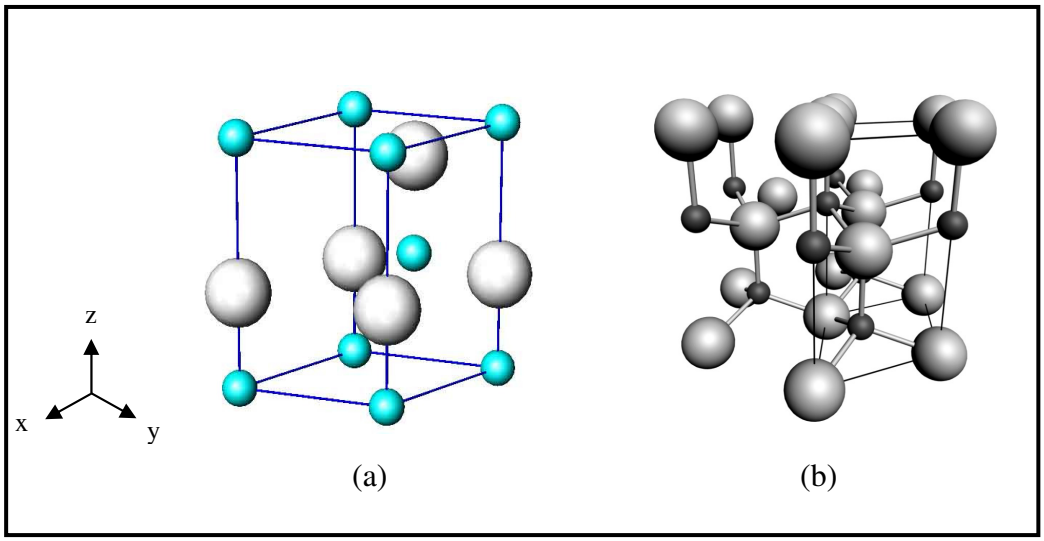

Figure 2. A drawing shows; (a) unit cell of ZnO and (b) tetrahedral coordination in ZnO. Big and small spheres represent oxygen and zinc atoms, respectively.
Source: http://www.geocities.jp/ohba_lab_ob_page/Structure/ZnO_Wurtzite.jpg
Source: Jagadish and Pearton (2006)

ZnO wurtzite structure is characterized by tetrahedral coordination of ion of one kind (e.g. Zn^{2+}) by the ions of another kind (e.g. O^{2-}) as composed of ZnO_4, or OZn_4, tetrahedral (Figure 2b). They are stacked in a hexagonal close-packed array with the tetrahedral edges of alternate layers rotated through 180° around the *c*-axis. The tetrahedral coordination of this compound is also a common indicator of sp^3 covalent bonding (the Zn *d*-electrons hybidrize with the O *p*-electrons). However, the bonding between the Zn atoms and O atoms are highly ionic, due to the large difference in their electronegative values (1.65 for Zn and 3.44 for O) thus ZnO lies on the borderline between being classed as a covalent and ionic compound.

It is well known that ZnO is a polar crystal, whose polar axis is the *c*-axis, and consists of a positive polar (0001) plane rich in Zn^{2+} ions and a negative polar $(000\bar{1})$ plane rich in O^{2-} ions. In coordination structure of ZnO crystal, the coordination number of Zn is four; all the tetrahedrons are connected together by corner sharing. So, the terminal vertex of a cornor of coordination polyhedron can still bond with three growth unit. The orientation of the Zn-O_4^{6-} tetrahedron in every sheet is obtained by rotating the adjacent sheet by 180º around the *c*-axis of the hexagonal lattices as shown in figure 3 (Li *et al*., 1999).

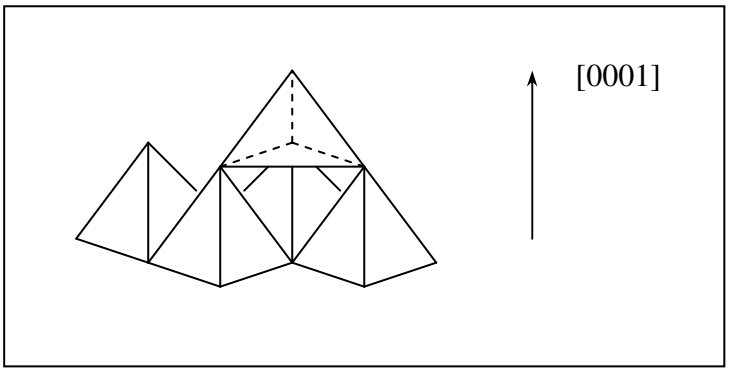

Figure 3. Idealized interface structure image of ZnO crystal in [0001] direction.
Source: Li *et al*., (1999)

Figure 3 shows that the terminal vertex of the cornor of the coordination of the polyhedron has the strongest bonding force, the terminal vertex of the edge of the coordination polyhedron has the second strongest binding force and the terminal vertex of face of the coordination polyhedron has the smallest binding force. So, the crystal force with the corner of the coordination polyhedron present at the interface has the fastest growth rate; the crystal face with the edge of the coordination polyhedron present at the interface has the second fastest growth rate and the crystal face with the face of coordination polyhedron present at the interface has the slowest growth rate. For this reason, the growth velocities in different directions are reported to be $V_{[0001]} > V_{[\bar{1}01\bar{1}]} > V_{[\bar{1}010]} > V_{[\bar{1}011]} > V_{[000\bar{1}]}$ when a hydrothermal route is employed (Hi *et al*., 2005). Accordingly, the most stable crystal structure is a regular prismatic hexagonal elongated along the *c*-axis as seen in figure 4.

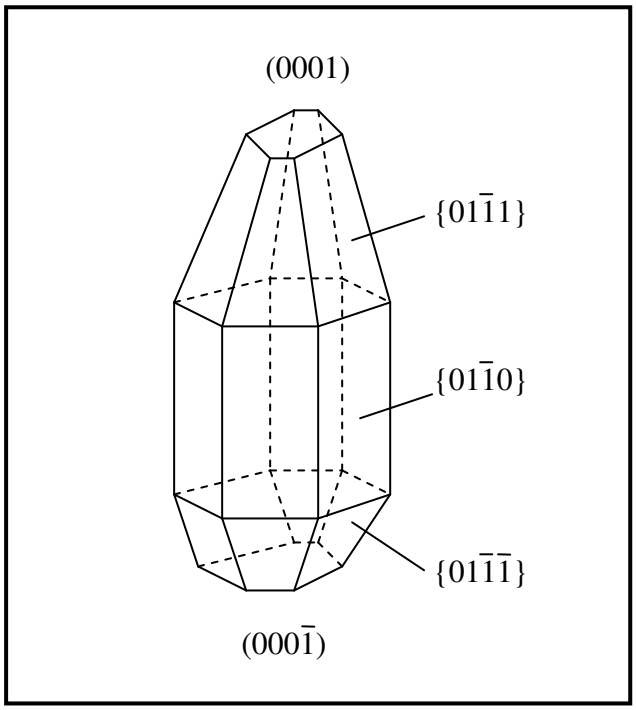

Figure 4. The facets in ZnO crystal.

Source: Li *et al*., (1999)

1.4. Review of literatures

Under chemical methods, stabilizers and capping agents were used to control the morphology of ZnO particles. In this work, only the former studies to investigate the morphological control by SDS and block copolymer are reviewed.

1.4.1. SDS as stabilizer

Li *et al*., (2005) studied the influence of SDS on formation of ZnO microcrystals from aqueous solution. 48 mL of 2 M NaOH was dropped into 20 mL of 1 M aqueous zinc nitrate. Then this mixture was transferred to a round-bottomed flask and 10 mL of 0.1 M SDS was subsequently dropped into a milky solution. The certain mixture was heated under stirring to reflux at 101 ^{o}C for 50-55 min. The white powders show the XRD pattern of ZnO wurtzite structure. After the $Zn(OH)_2$ precursor in an aqueous media was heated, the nut-like ZnO crystals were shaped as shown in figure 5.

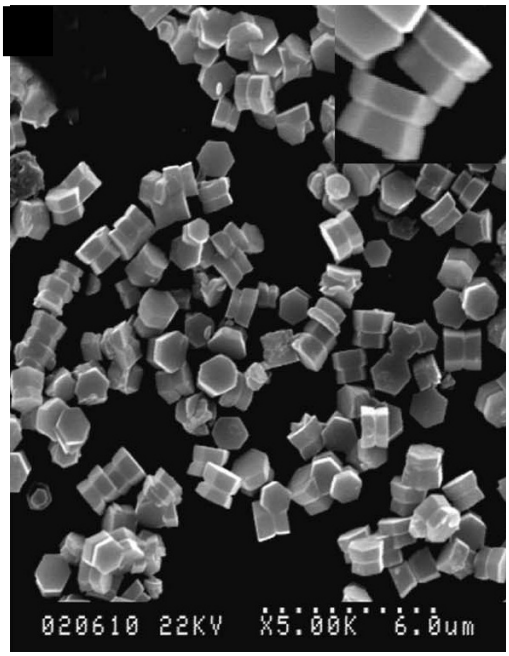

Figure 5. SEM image of ZnO microparticles prepared from 0.1 M SDS.
Source: Li *et al*., (2005)

The formation of this shape was suggested that it is due to an adsorption of SDS on a polar plane (0001) of ZnO crystal and thus inhibits the growth along the *c*-axis. The sulfonate group of each SDS molecule can simultaneously adsorb two ZnO nuclei on the (0001) plane. The growth along the *c*-axis is then retarded and it can grow only along the $(000\bar{1})$ face which is a slowest growth rate. For this reason, nut-like ZnO with twin-structure is formed as shown in figure 6.

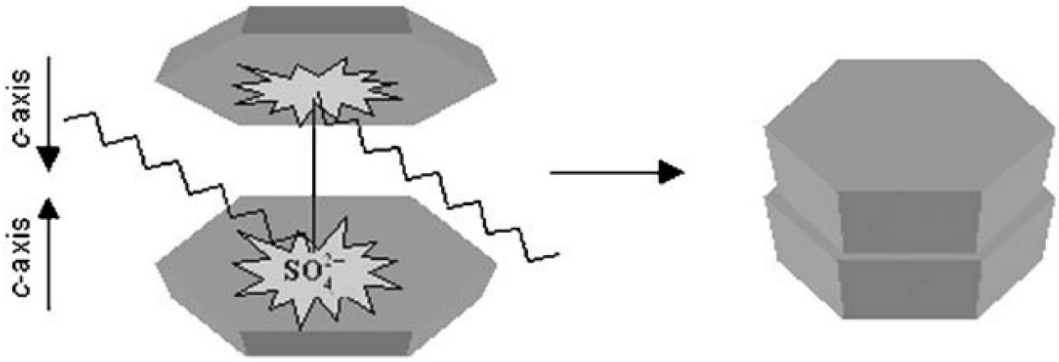

Figure 6. The model of SDS modifying the habit of ZnO crystal.
Source: Li *et al*., (2005)

Yin *et al*., (2005) studied the assemblage of ZnO nanorods into chrysanthemum-like crystals. These crystals were synthesized from a mixture of 0.4 g of $Zn(C_2H_3O_2)_2.2H_2O$ and 20 mL of SDS solution. Then 10 mL of 0.5 M NaOH solution was dropped into a previous solution and was transferred into a Teflon-lined autoclave. The autoclave was heated at 160 ^{o}C for 24 h. The white precipitates were collected and dried in air at 60 ^{o}C. The products show the chrysanthemum-like ZnO crystals that are composed of many ZnO nanorods as shown in figure 7. From electron diffraction study, the spots can be indexed as the hexagonal ZnO phase. These results suggest that the ZnO nanorod may grow along the [0001] direction. The process of assembling ZnO nanorods into chrysanthemum-like shape can be described in figure 8.

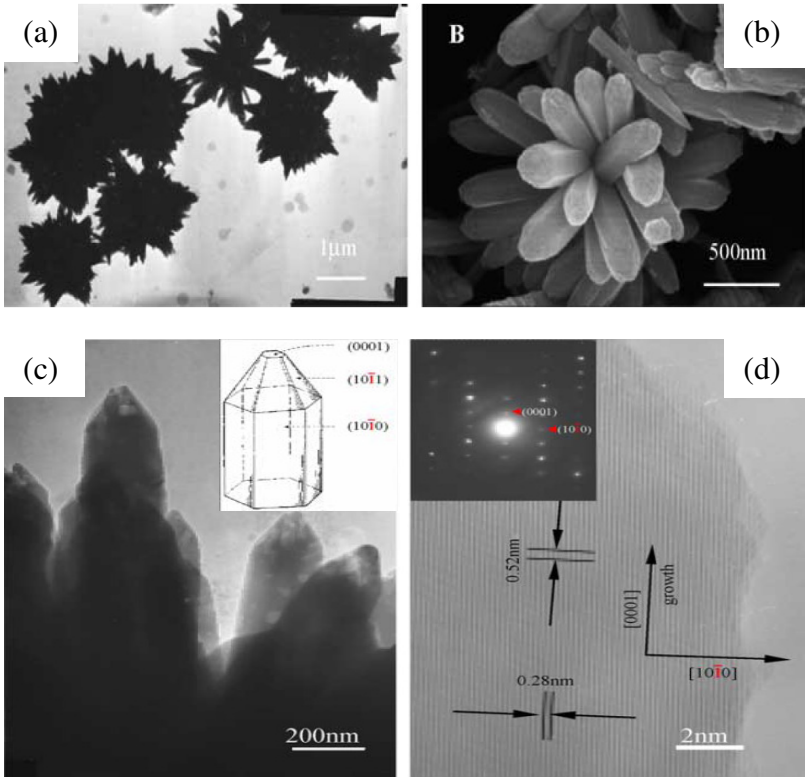

Figure 7. (a) TEM, (b) SEM and (c) as well as (d) HRTEM images of chrysanthemum like ZnO crystals.

Source: Yin *et al*., (2005)

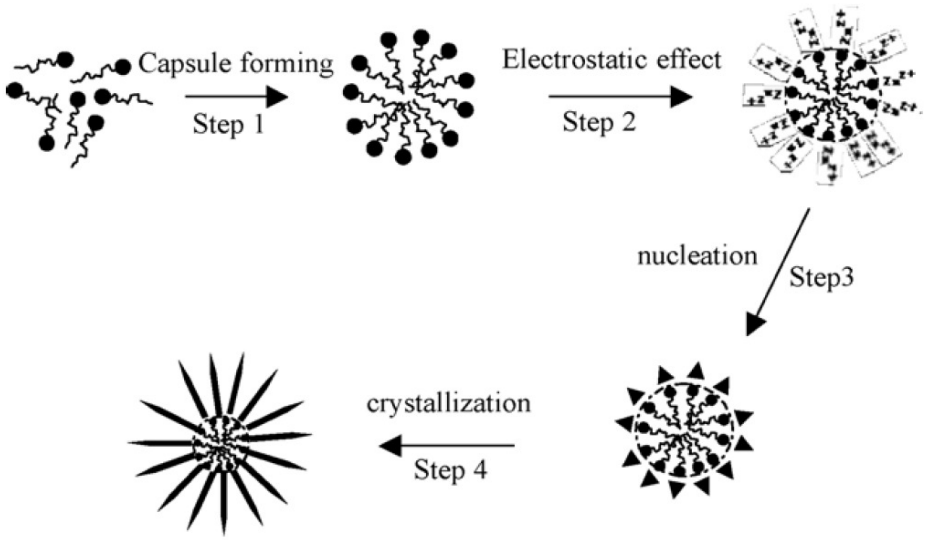

Figure 8. Illustration of assembled process of the chrysanthemum-like ZnO crystals.

Source: Yin *et al*., (2005)

The supersaturated SDS solution maybe generates the micro spherical capsules (step 1). In an aqueous solution, the sulfonic group that acts as a hydrophilic part will point to the outer surface while a hydrophobic end points to the inner. The Zn^{2+} ions interact with sulfonic groups at the outer surface of the capsules (step 2). The adsorbed Zn^{2+} ions then convert into ZnO nuclei during the hydrothermal process (step 3). These SDS capped ZnO nuclei grow along the *c*-axis to form nanorods due to the anisotropic growth. When an aging time was prolonged, a longer ZnO nanorod was produced resulting in the formation of chrysanthemum-like ZnO crystals (step 4).

Sun *et al*., (2006) investigated the effect of molar ratio between NaOH and $Zn(C_2H_3O_2)_2$ on variation of the aspect ratio of ZnO nanowire synthesized by microemulsion-mediated hydrothermal process. Zinc acetate and NaOH solutions were mixed under a constant stirring. This solution was added into the SDS solution which was prepared in a mixture of heptane and hexanol. After it was heated at 140 ^oC in autoclave for 12 h, the white precipitates were dried in vacuum at 60 ^oC for 12 h. The aspect-ratio (length to diameter, L/D ratio) of an as-obtained ZnO nanowire is sensitive to the $[NaOH]/[Zn(C_2H_3O_2)_2]$ molar ratio (w) as shown in figure 9. A possible mechanism for formation of ZnO nanowire is presented in figure 10.

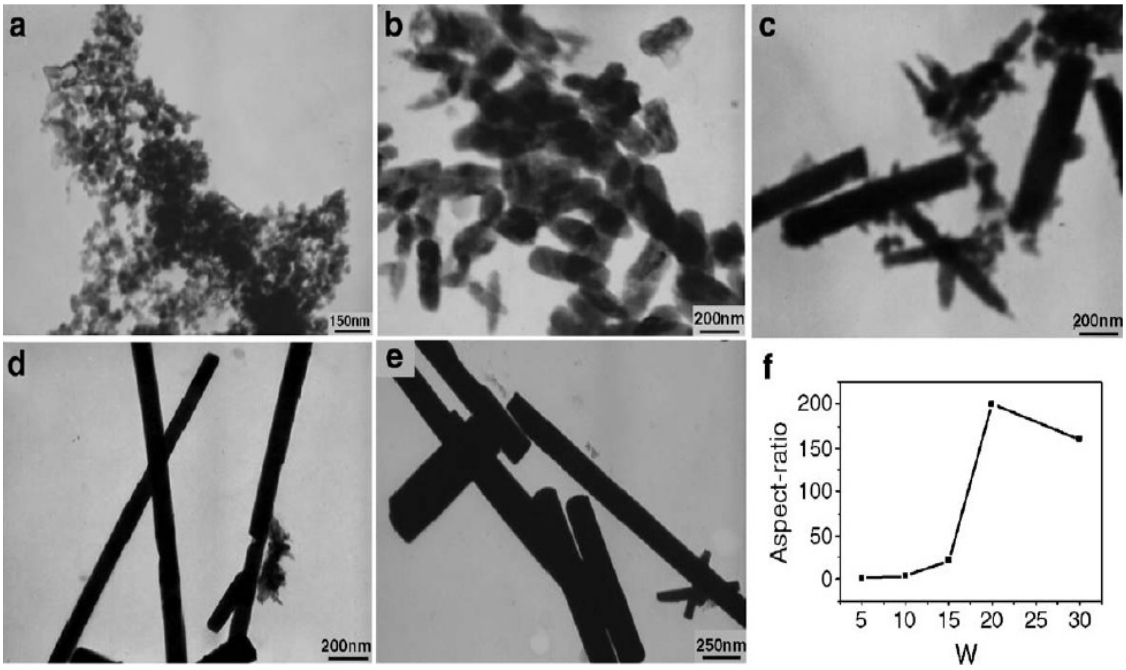

Figure 9. TEM images of as-prepared ZnO nanowires at different w values: (a) w = 5, (b) w =10, (c) w = 15, (d) w = 20, (e) w = 30 and (f) the variation of the aspect ratio of ZnO nanowires.

Source: Sun *et al*., (2006)

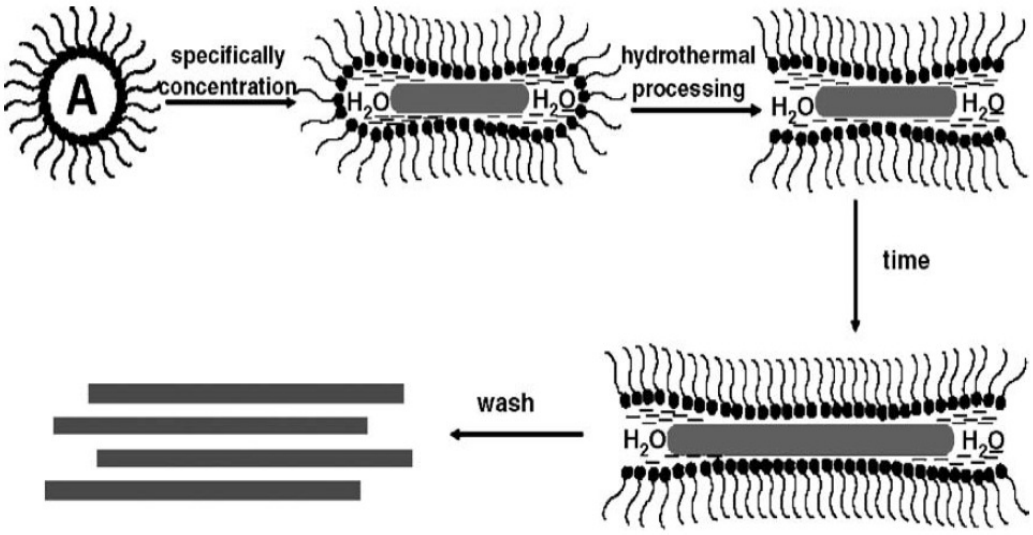

Figure 10. Schematic illustration of the formation mechanism of ZnO nanowires in microemulsion. "A" stands for the retants.

Source: Sun *et al*., (2006)

It had been well known that the aspect ratio strongly affected the optical properties. In this report, the emission in visible region increases when the aspect ratio (L/D) or w was increased as shown in figure 11. The intensity of visible emission band at 530 nm enhance with increasing the aspect ratio of nanowires. This is due the increase of the surface defect when the length of nanowires increased.

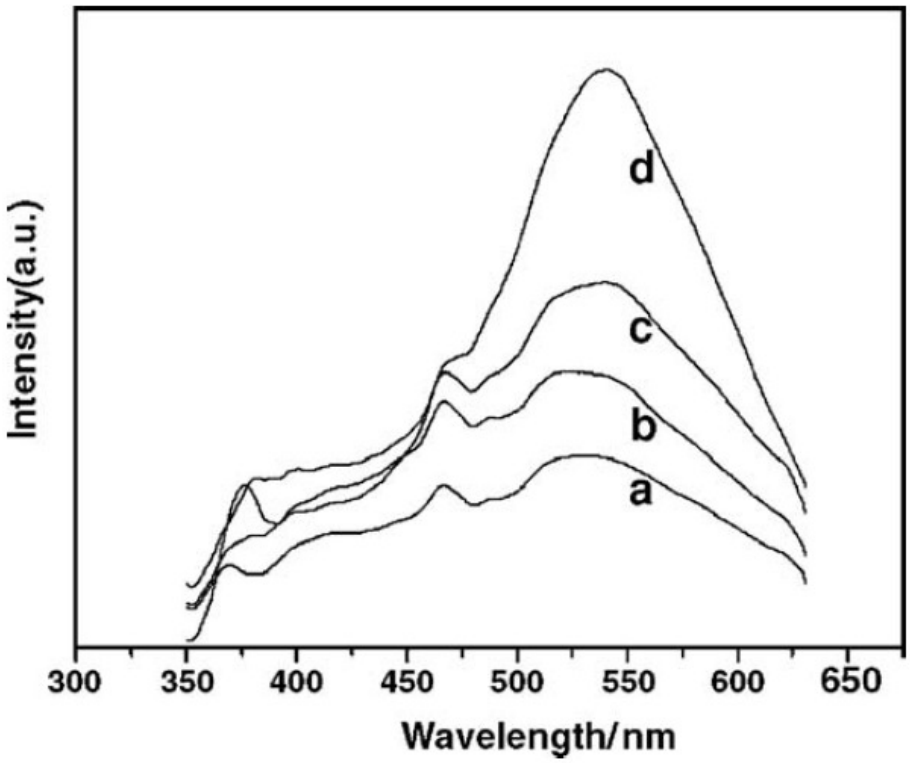

Figure 11. Photoluminescence spectra of as-prepared ZnO nanowires at different w values: (a) w = 10, (b) w = 15, (c) w = 30 and (d) w = 20.

Source: Sun *et al*., (2006)

Ni *et al*., (2008) reported the successfully synthesized the flower-like ZnO nanoparticles via a simple hydrothermal route in the presence of SDS. 0.005 mole of $Zn(C_2H_3O_2)_2$ and 0.02 mole of KOH were dissolved in distilled water. After 0.10 g of SDS was added, the mixture was transferred into a Teflon-lined stainless steel autoclave. The solution was heated at 150 ^{o}C for 10 h. White precipitates were collected and dried in air at 60 ^{o}C for 5 h. Figure 12 shows the SEM images of ZnO obtained from the solution at various SDS concentrations.

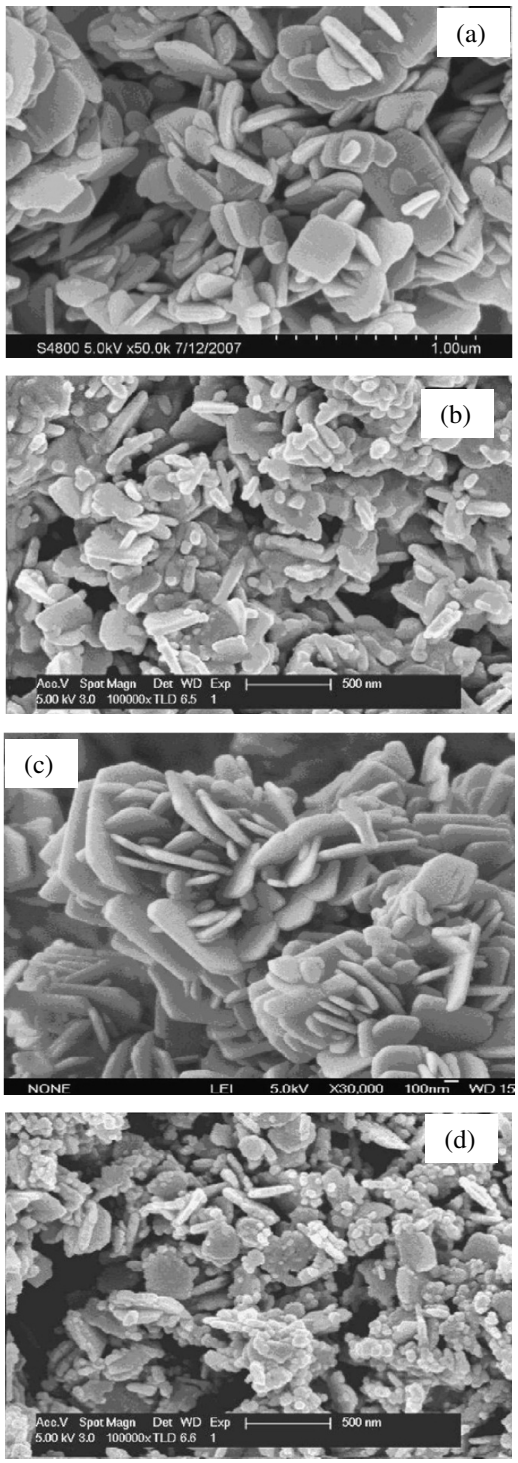

Figure 12. SEM images of ZnO obtained from the systems with different concentrations of SDS: (a) 0 mol/L, (b) 0.725 x 10^{-2} mol/L, (c) 1.45 x 10^{-2} mol/L and (d) 2.90 x 10^{-2} mol/L.

Source: Ni *et al*., (2008)

The formation of nanoflakes should also be attributed to the basicity of the solution although the molar ratio of OH^-/Zn^{2+} reduced to 4. The interaction between SDS and nanoflakes was too weak to cause the self-assembly of ZnO nanoflakes at a low concentration of SDS. At high concentration, SDS served as a protector to prevent particles from aggregation which led to the formation of many ZnO nanoparticles. Only when certain concentration of SDS was used, flowerlike ZnO crystals were formed via the self-assembly of nanoflakes due to a proper interaction.

Yang *et al*., (2008) synthesized the ZnO quantum dots through a thermal decomposition at low temperature. The solution of NH_4HCO_3 and SDS were mixed together. The $ZnCl_2$ solution was then added dropwise into a previous solution. White precipitates were gradually formed in the solution during the dropping process. Finally, ZnO quntum dots were obtained after annealing at 200 ^oC for 1 h in air. The as-prepared samples show that all diffraction peaks could be identified to ZnO with hexagonal wurtzite structure. The photoluminescence spectrum of as-synthesized ZnO quautum dots shows an emission peak at 385 nm in a UV region and a broad band emission in a range of 420-700 nm as shown in figure 13. The sharp peak at 650 nm is a scattering emission peak of excitation source.

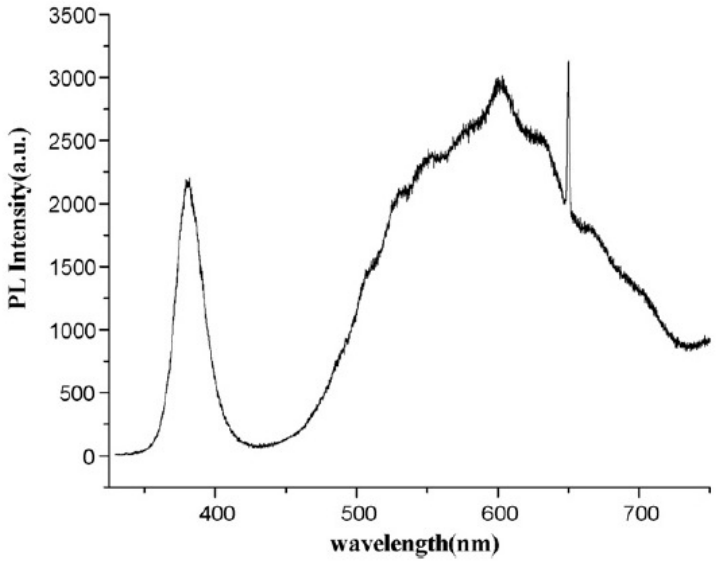

Figure 13. Room temperature photoluminescence spectrum of ZnO quantum dots.
Source: Yang *et al*., (2008)

Li *et al*., (2008) investigated the controllable growth of ZnO nanowhiskers prepared by a simple solution route. 30 mL of NaOH followed by 5 mL of SDS solution was added dropwise into 20 mL of $ZnCl_2$ solution under vigorous stirring at 3 ^{o}C and subsequently transferred into a conical flask and aged at 85 ^{o}C for 5 h. Finally, the ZnO powders were obtained and dried in air. It is obvious that the addition of 0.01 M SDS in the solution could increase the aspect ratios of a whisker, in other words, it could promote the crystal growth along the *c* axis and finally leads to the formation of a needle-like shape as shown in figure 14.

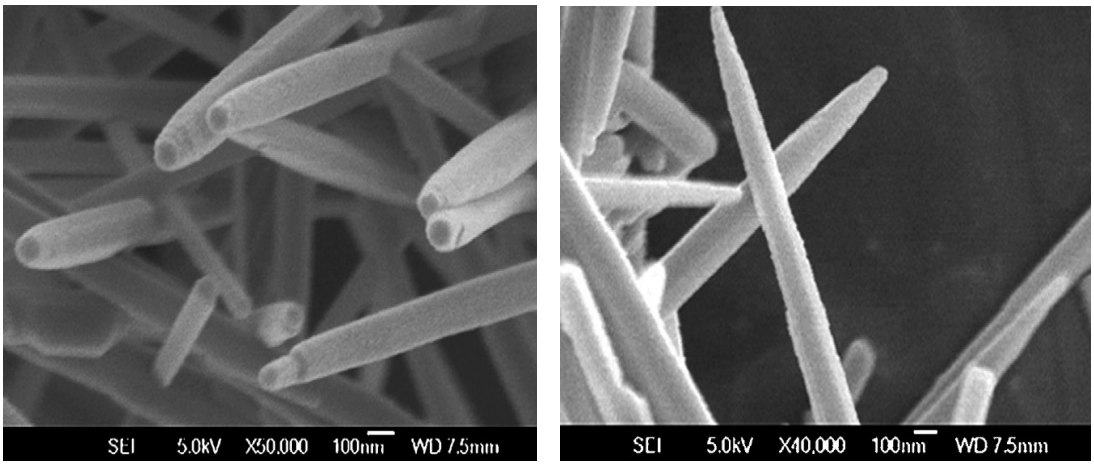

Figure 14. FESEM images of ZnO nanowhiskers.
Source: Li *et al*., (2008)

Usui H. (2009) studied the surfactant concentrations dependence of structure and photocatlytic properties of ZnO rods prepared through a chemical synthesis in an aqueous solution. Firstly, 50 mL of 0.2 M $ZnSO_4.7H_2O$ aqueous solution was mixed with the SDS solution within a concentration range of 0-0.1 M. This solution was adjusted to pH 7-13.5 by NaOH solution. The mixed solution was stirred for 90 min at room temperature and continuous by heated at 85 ^{o}C for 5 h. The colloidal suspensions were repeatedly centrifuged and washed with distilled water. Only at a pH value of 13, the products exhibit diffraction patterns of wurtzite ZnO without any impurity phase. At pH of 9-12, the mixed phase between $Zn(OH)_2$ and ZnO was observed as shown in figure 15.

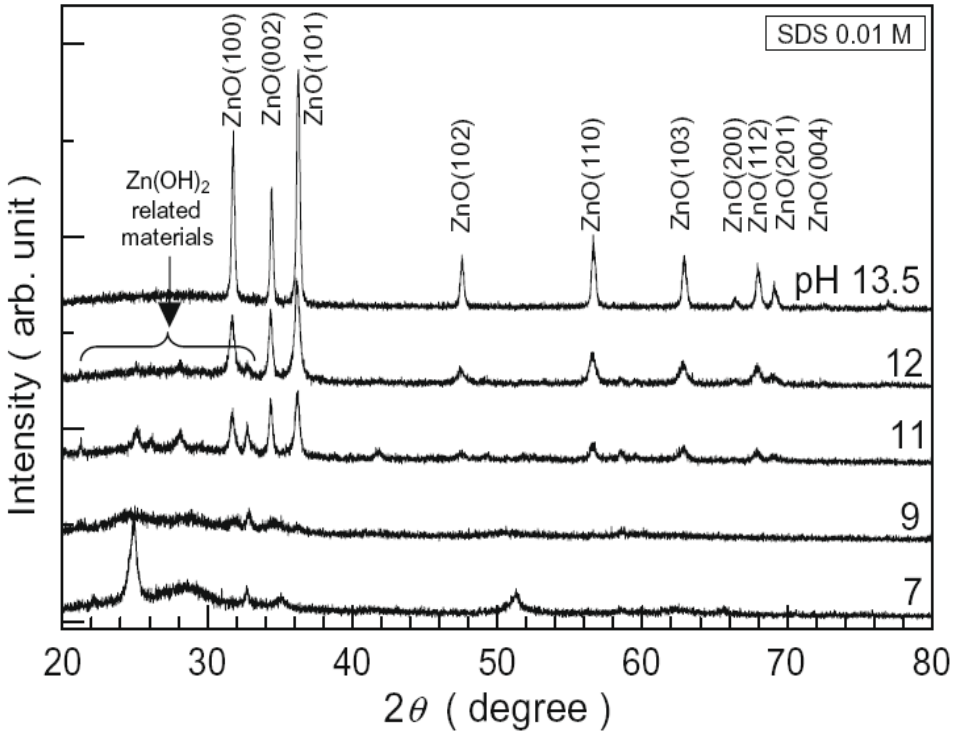

Figure 15. XRD patterns of products prepared in an aqueous solution containing 0.01 M SDS solution at various pH values.

Source: Usui H, (2009)

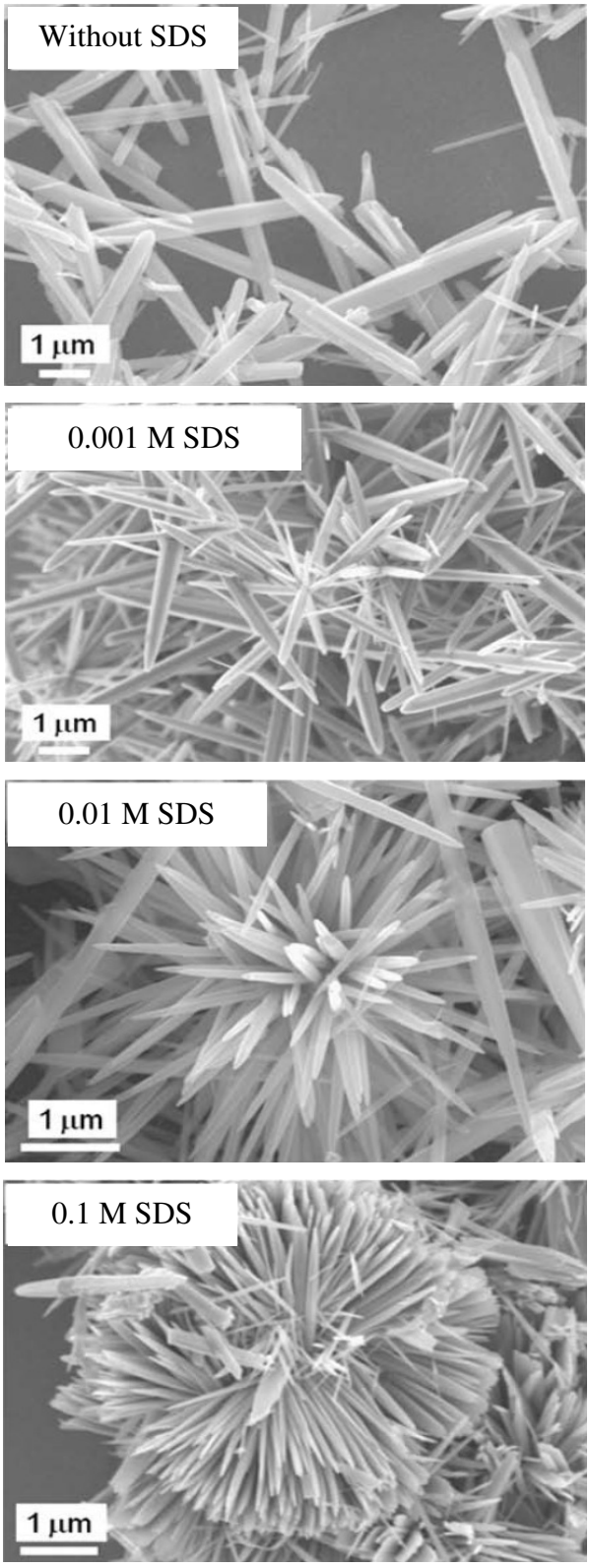

Figure 16. FESEM images of ZnO powder prepared in an aqueous solution with different SDS concentrations.

Source: Usui H, (2009)

Figure 16 shows FESEM images of ZnO prepared from different SDS concentrations. At 0 M SDS, the morphology of ZnO crystal was a single straight rod. At 0.001 M SDS, ZnO particles show a single straight rod and connected rods. At 0.01 M and 0.1 M SDS, almost products were radial-shaped rods. A possible mechanism of crystal growth of ZnO in this system is shown in figure 17.

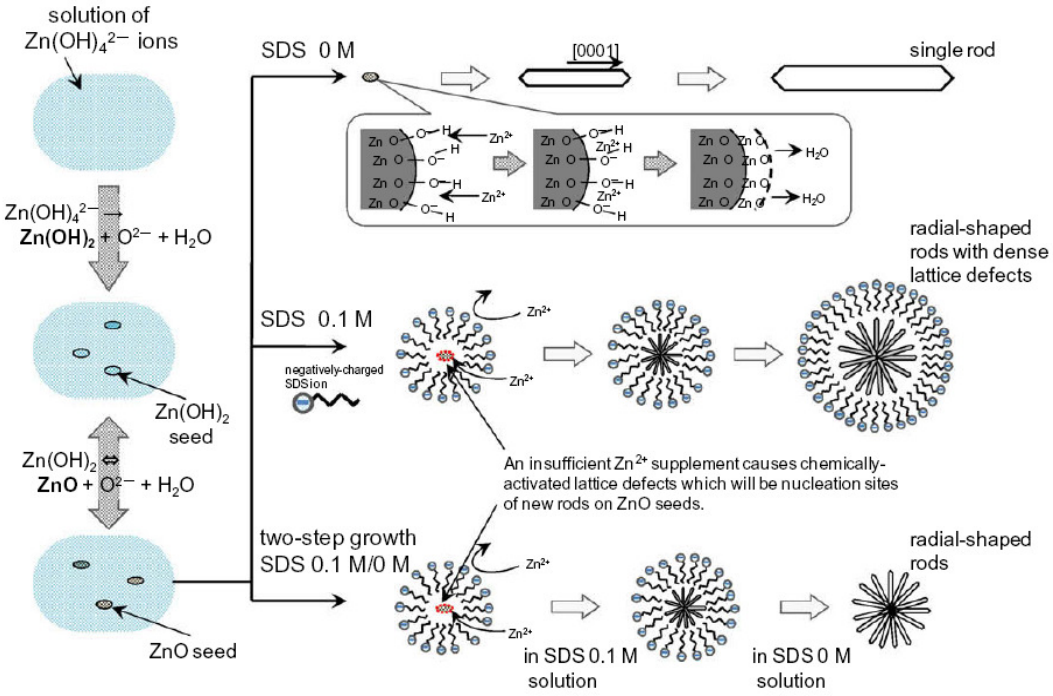

Figure 17. Schematic configuration of ZnO rod growth under different surfactant concentrations.

Source: Usui H, (2009)

1.4.2. Block copolymer as a stabilizer

Oner M., (1998) used a poly (ethylene oxide) -block -poly(methyl-acrylic acid) (PEO-*b*-PMMA) diblock copolymer to control the crystallization of ZnO. Zinc nitrate solution was mixed with hexamethylenetetramine (HMT) and polymer solution at room temperature. To study the effect of polymer on crystallization, its concentration was varied from 30 to 300 ppm. The pH value of the mixture was adjusted to 3 by the addition of HNO_3. Then this solution was heated at 95 ^oC for 45 min. The suspension of ZnO was filtered through a membrane with a pore size of 0.22 μm. The residue was washed with deionized water and dried in vacuum at 50 ^oC. The morphologies of synthesized ZnO particles are shown in figure 18.

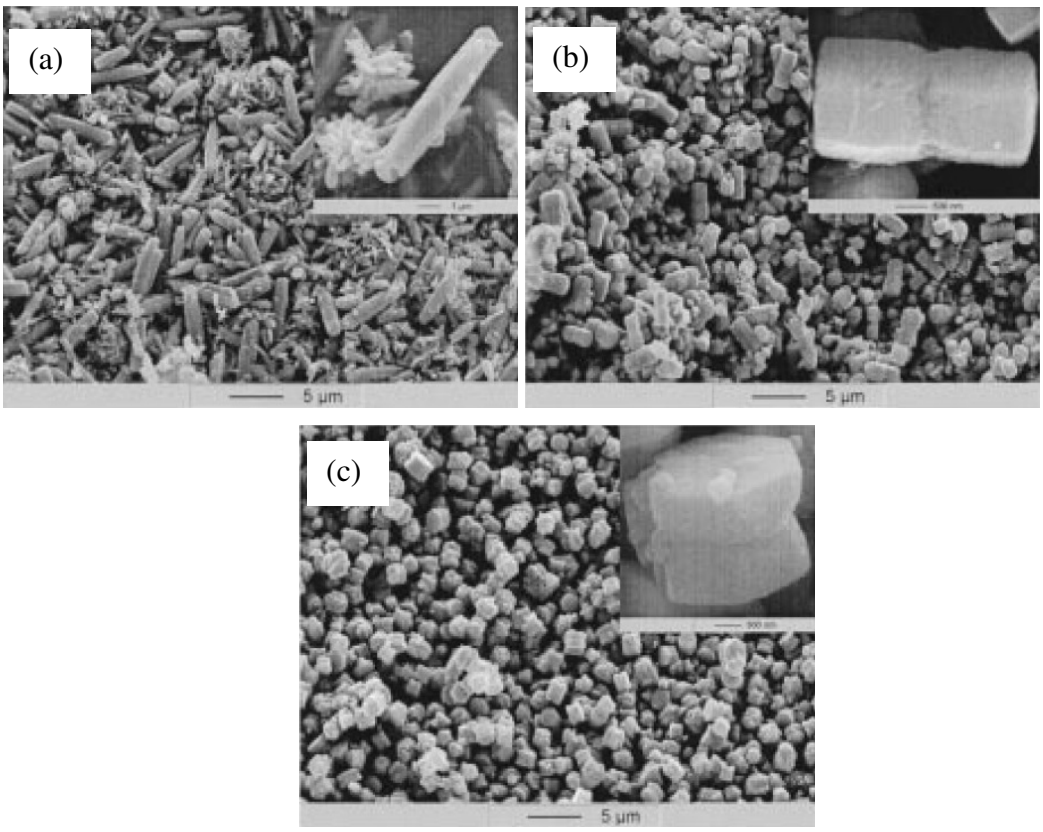

Figure 18. SEM micrographs of ZnO particles grown with various PEO-*b*-PMMA concentrations: (a) 0, (b) 60 and (c) 300 ppm.

Source: Oner M, (1998)

From the figure 18, the aspect ratio (L/D) is thus strongly dependent on a concentration of diblock copolymer and the ZnO crystal becomes smaller as the polymer concentration increases. However, the mechanism of ZnO crystal growth was not discussed yet.

Bai *et al*., (2007) reported a self-assembly of clew-like ZnO superstructures in the presence of $(PEO)_{20}$-$(PPO)_{70}$-$(PEO)_{20}$ (P123, MW = 5800). 5.95 g of $Zn(NO_3)_2.6H_2O$ and 2.32 g of P123 were dissolved in deionized water. After that, 7.2 g of urea was added and the final mixture was transferred into a Teflon-lined stainless steel autoclave and heated at 100 ^oC for 24 h. The white precipitates were calcined in air at 500 ^oC for 2 h. The morphology of samples prepared from a low P123 concentration ($P123/Zn(NO_3)_2$ = 0.005 – 0.01) showed a mixture of clew-like spheres and large rods with triangle-cone-shaped heads as shown in figure 19 (a-d).

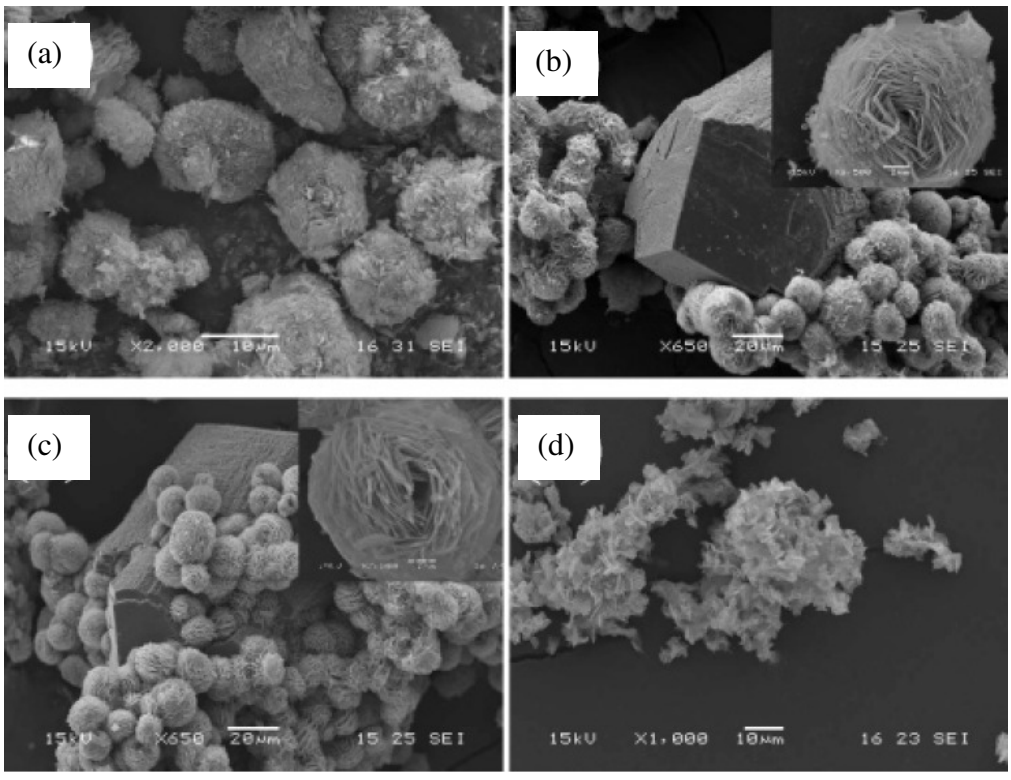

Figure 19. SEM images of samples prepared with different P123 concentrations, and different molar ratios of $P123/Zn(NO_3)_2$ (a) 0, (b) 0.005, (c) 0.01 and (d) 0.04.

Source: Bai *et al*., (2007)

The clew-like sphere ZnO superstructure is made up of the thin ZnO nanotips as shown in figure 20. As a molar ratio of P123/$Zn(NO_3)_2$ = 0.04, only nanoflakes without well defined morphology were formed as shown in figure 19(d).

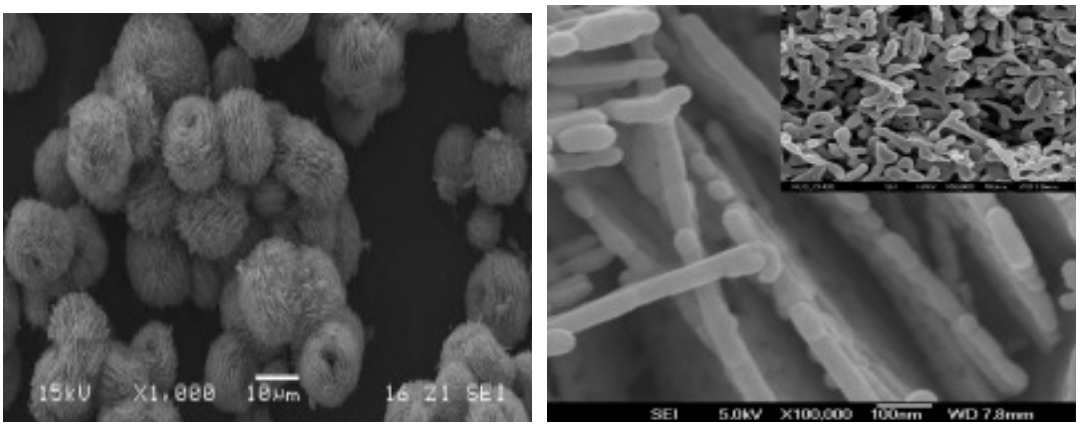

Figure 20. SEM images at high magnification of ZnO superstructure.
Source: Bai *et al*., (2007)

Zhang *et al*., (2007) reported the formation of ZnO nanobundles by hydrothermal method when PEO-PPO-PEO block copolymer was used as stabilizer. 5 mmol of $Zn(C_2H_3O_2)_2.2H_2O$ and 100 mmol of NaOH were mixed in 10 mL of distilled water. The solution was then filled with 3 g of polyesters (L64 : $EO_{13}PO_{30}EO_{13}$ and F68 : $EO_{80}PO_{30}EO_{80}$) and heated at 160 ^oC for 15 h in an autoclave. The precipitates were filled off and dried in a vacuum desiccator at 60 ^oC for 4 h. The SEM and TEM of the products prepared under L64 and F68 systems are presented in figure 21.

.

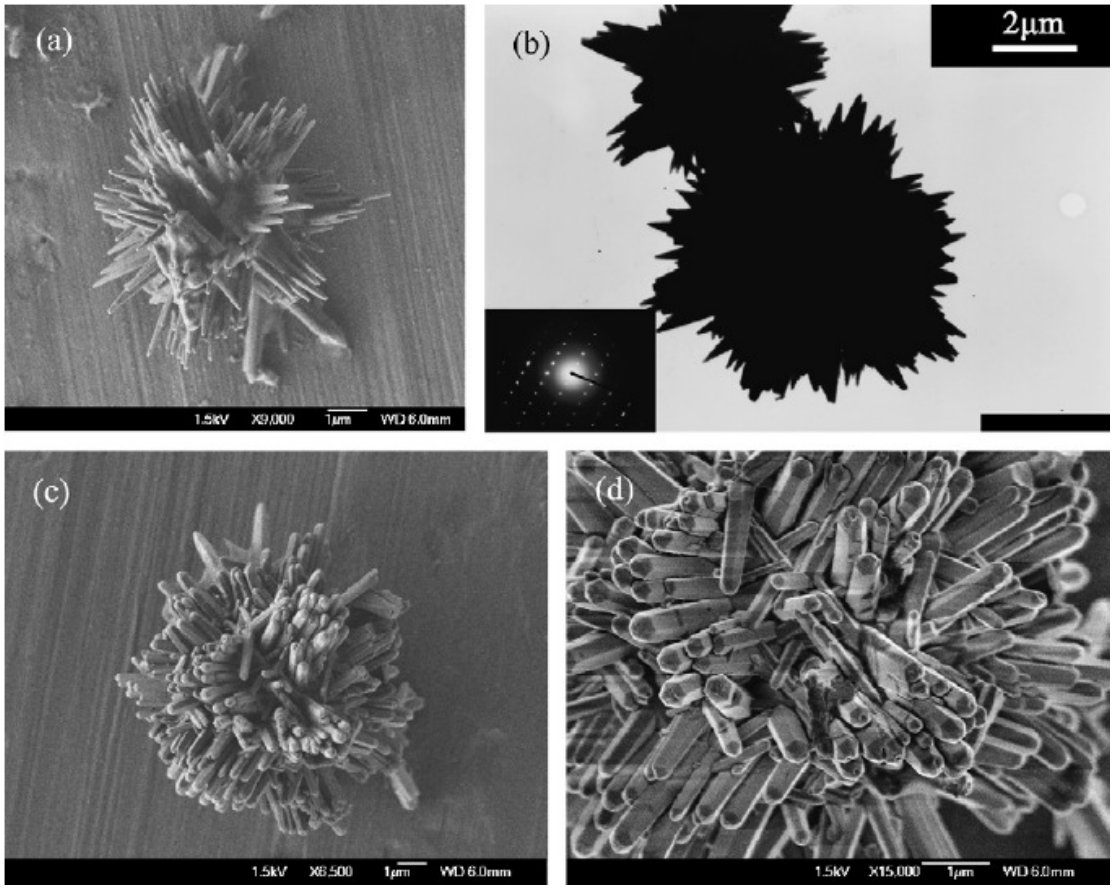

Figure 21. SEM and TEM images of ZnO homocentric bundles obtained from block copolymers systems: (a and b) L64 and (c and d) F68.

Source: Zhang *et al*., (2007)

The evaluated average diameter and length of the ZnO nanorods are about 150 nm and 1.5 μm in the L64 system and about 300 nm and 1.8 μm in the F68 system, respectively. Furthermore, the ends of rods evolve into a pyramid-like shape in L64 and a prism-like shape in F68 system. The ZnO formation in this study can be proposed as seen in figure 22.

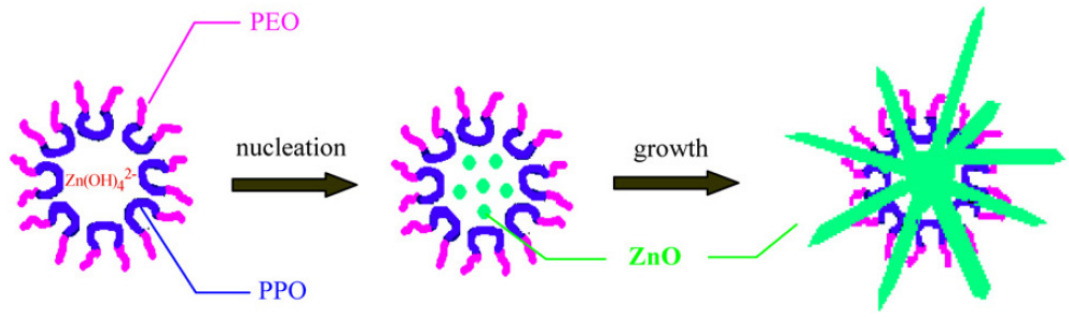

Figure 22. Proposed mechanism for the formation of ZnO homocentric bundles. Source: Zhang *et al*., (2007)

The size of ZnO homocentric bundle structure increases when a size of the macromolecular micelles increases. At the same concentration, the aggregation size of the F68 micelle is larger due to its longer PEO chain. A room temperature photoluminescence spectra of ZnO products showed a sharp ultraviolet emission located around 360 nm.

Tao *et al*., (2008) described the systematical preparation of ZnO hollow microsphere by triblock copolymer. 0.05 mmol of $Zn(C_2H_3O_2)_2.2H_2O$ and 0.5 mL of diethanolamine (DEA) were added into the 0.36 mmol of P123 (PEO-PPO-PEO) solution in 25 mL of ethanol. After the mixed solution was aged for 3 h, it was transferred into a Teflon-lined autoclave and heated at 120-200 ^{o}C for 24 h in an oven. The synthesized ZnO powder shows a microsphere with a hollow structure as seen in figure 23.

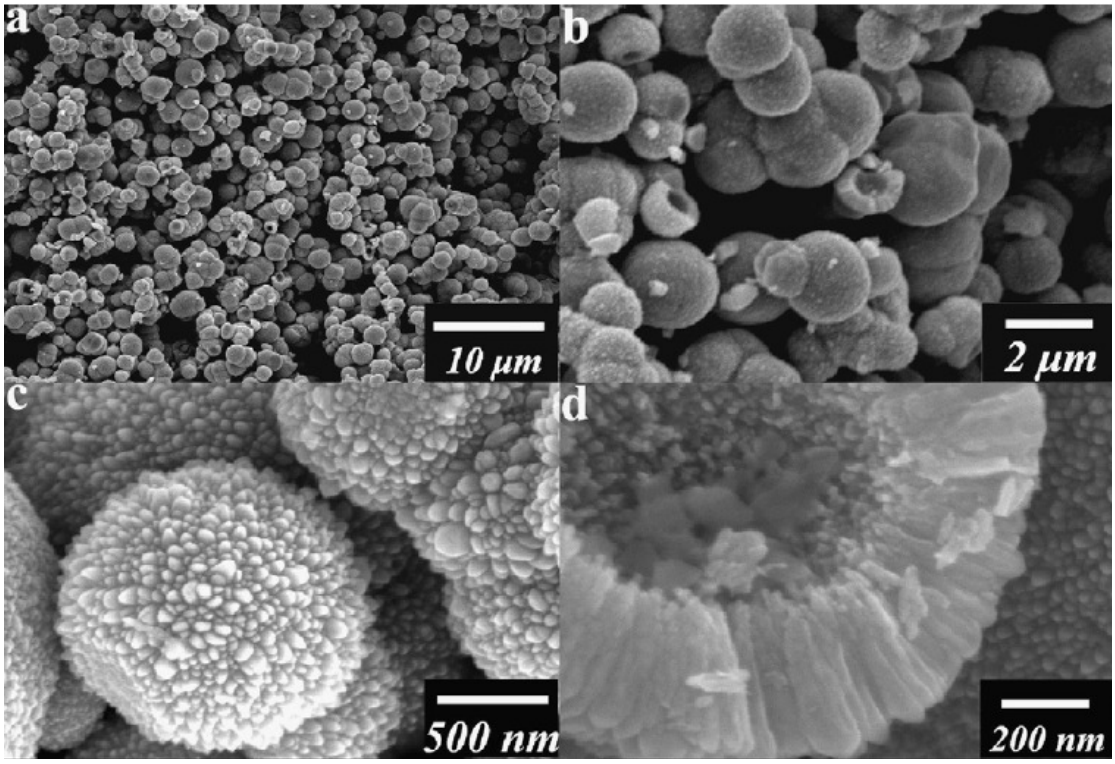

Figure 23. SEM image of ZnO hollow structure prepared from 0.036 mmol of triblock copolymer: (a, b) low-magnification, (c) high-magnification and (d) high-magnification for one broken hollow microsphere.

Source: Tao *et al*., (2008)

The surface of microspheres is covered by the ends of the rod-like particles. These rod-like particles are ~350 nm in length and 30-50 nm in diameter, and they can be assembled into the shell of hollow microspheres.

1.5. Objectives

1.5.1. To prepare the modified-ZnO particles with sodium dodecyl sulfate (SDS) and poly(ethylene oxide)-block-poly(propylene oxide) (PEO-*b*-PPO).

1.5.2. To study the dependence of morphology on optical properties of SDS and PEO-*b*-PPO diblock copolymer modified-ZnO particles.

CHAPTER 2

INSTRUMENTATION

2.1. X-ray Powder Diffraction

X-ray diffraction (XRD) is a non-destructive technique primarily used for phase identification of a crystalline material and this technique provides the information on unit cell dimensions. Most of solid materials can be described as a crystalline and when X-ray interacts with a crystalline phase, a diffraction pattern is generated as a result of the interaction between the incident X-ray and the atomic architecture of a solid.

2.1.1 Fundamental principles of XRD

X-rays are electromagnetic radiation with typical photon energies in the range of 10-100 eV or wavelength between roughly 0.01 - 10 nm. This wavelength lies between the ultraviolet light and gamma rays in the electromagnetic spectrum. For diffraction applications, only relatively short wavelengths X-ray in a range of a few angstroms to 0.1 angstrom are used. Because the wavelength of X-ray is comparable to the size of atoms, they are ideally suited for probing the structural arrangement of atoms and molecules in a wide range of materials. The energetic X-rays can penetrate deeply into the materials and provide information about the structure, such as crystallite size and lattice parameter, etc.

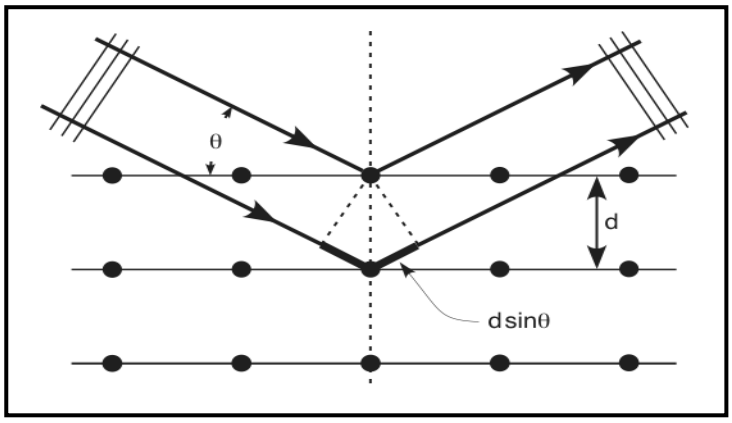

Figure 24. Bragg diffraction condition.
Source: http://upload.wikimedia.org/wikipedia/commons/0/0a/Bragg_diffraction.png

If an incident X-ray beam encounters a crystal lattice, general scattering occurs as seen in figure 24. Although most scattering interferes with itself and is eliminated (destructive interference), diffraction occurs when scattering in a certain direction is in phase with scattered rays from other atomic planes. Under this condition, the reflections combine to form new enhanced wave fronts that mutually reinforce each others (constructive interference). In 1912, W.L. Bragg recognized a predictable relationship among several factors. The relation by which diffraction occurs is known as the Bragg law or Bragg equation, and it can be expressed below:

$$2d \sin\theta = n\lambda \qquad (1)$$

where n is a small integer giving the order of diffraction analogous to a ruled grating, (an integer), λ is a wavelength of the characteristic line X-rays from the X-ray tube (usually the CuK_α doublet with Cu$K_{\alpha 1}$ = 0.1540562 nm), d is a distance in a nanometer between a set of parallel lattice planes, and θ is an angle between an incident collimated X-ray beam and an atomic lattice plane in the crystal.

Each crystalline solid has a unique atomic architecture and it consequently has a unique characteristic X-ray powder pattern. These patterns can be used as “fingerprints” for identification of solid phases.

This Bragg law relates the wavelength of electromagnetic radiation to the diffraction angle and the lattice spacing in a crystalline sample. These diffracted X-rays are then detected, processed and counted. By scanning the sample through a range of 2θ angles, all possible diffraction directions of the lattice should be attained due to the random orientation of the powdered material. Conversion of the diffraction peaks to *d*-spacings allows the identification of the mineral because each mineral has a set of unique *d*-spacings. Typically, this is achieved by comparison of *d*-spacings with standard reference patterns.

The X-ray diffraction pattern of a pure substance is, therefore, like a fingerprint of the substance. The powder diffraction method is thus ideally suited for characterization and identification of polycrystalline phases (Scintag Inc., 1999).

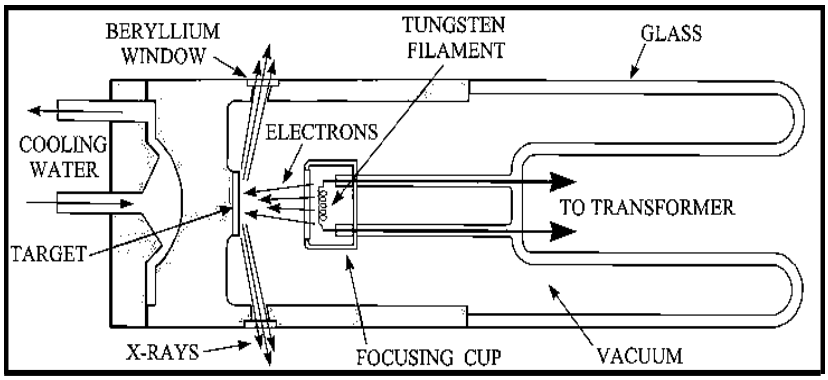

Figure 25. Schematic cross section of an X-ray tube.
Source: http://pubs.usgs.gov/of/2001/of01-041/htmldocs/images/xrdtube.jpg

X-ray diffractometers consist of three basic elements: an X-ray tube, a sample holder, and an X-ray detector. X-rays are generated in a cathode ray tube by heating a filament (cathode) to produce electrons, accelerating the electrons toward a target by applying a voltage (normally in order of 30 kV to 50 kV), and bombarding the target material (anode) with electrons (Figure 25). When electrons have sufficient energy to dislodge inner shell electrons of the target material, characteristic X-ray spectra are produced (Figure 26a). These spectra consist of several components, the most common being K_α and K_β (Figure 26b).

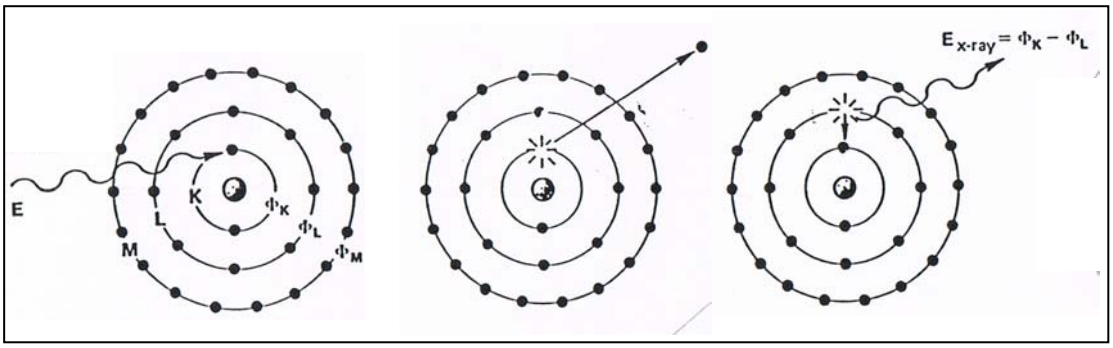

(a)

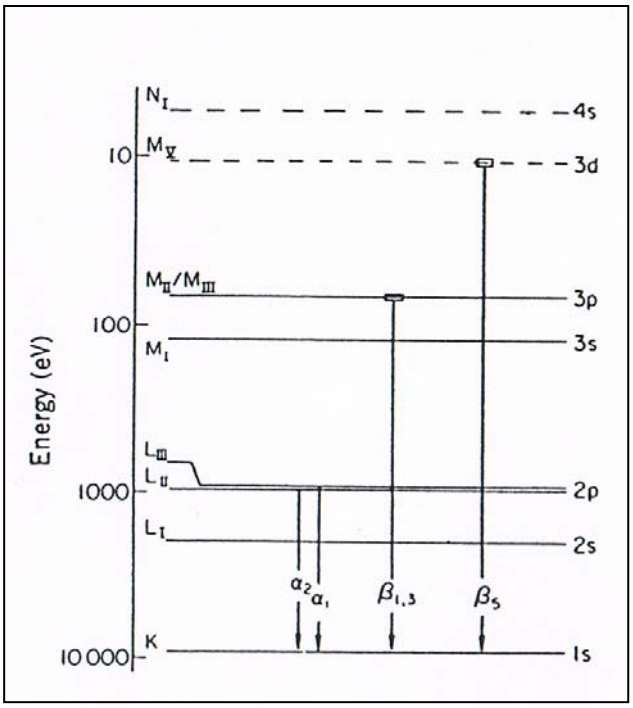

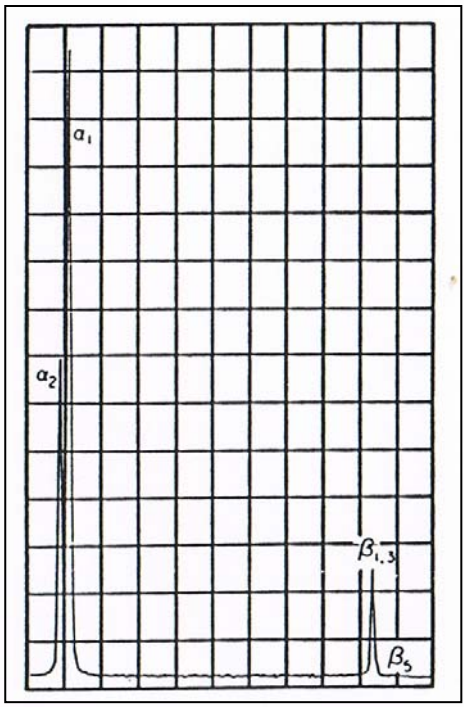

(b) (c)

Figure 26. Schematic diagrams (a) an incoming electron displaces a K-shell electron. If an L-shell electron moves to replace it, a K_α X-ray is produced. If an M-shell electron moves to replace it, a K_β X-ray is produced. (b) energy-level diagram for an atom illustrating the excitation of the K, L, M and N shells and the formation of K_α, K_β, L_α and M_α X-rays, and (c) X-ray spectrum consists of two different radiations continuous and characteristic radiation for copper.

Source: Jenkins *et al*., (1996)

K_α consists, in part, of $K_{\alpha1}$ and $K_{\alpha2}$. $K_{\alpha1}$ has a slightly shorter wavelength and twice the intensity as $K_{\alpha2}$ (Figure 26c). Copper is the most common target material for single-crystal diffraction, with CuK_α radiation = 1.5418 Å. Filtering, by foils or crystal monochrometers, is required to produce monochromatic X-rays needed for diffraction. $K_{\alpha1}$ and $K_{\alpha2}$ are sufficiently close in wavelength such that a weighted average of the two is used.

After producing from X-ray tube, X-rays are collimated and directed onto the sample. As the sample and detector are rotated, the intensity of the reflected X-rays is recorded. When the geometry of the incident X-rays impinging the sample satisfies the Bragg equation, constructive interference occurs and a peak intensity occurs. A detector records and processes this X-ray signal and converts the signal to a count rate which is then output to a device such as a printer or computer monitor.

The geometry of an X-ray diffractometer is such that the sample rotates in the path of the collimated X-ray beam at an angle θ while the X-ray detector is mounted on an arm to collect the diffracted X-rays and rotates at an angle of 2θ. The instrument used to maintain the angle and rotate the sample is termed a goniometer. This arrangement is called the Bragg-Brentano parafocusing geometry (Figure 27) and data is collected at 2θ.

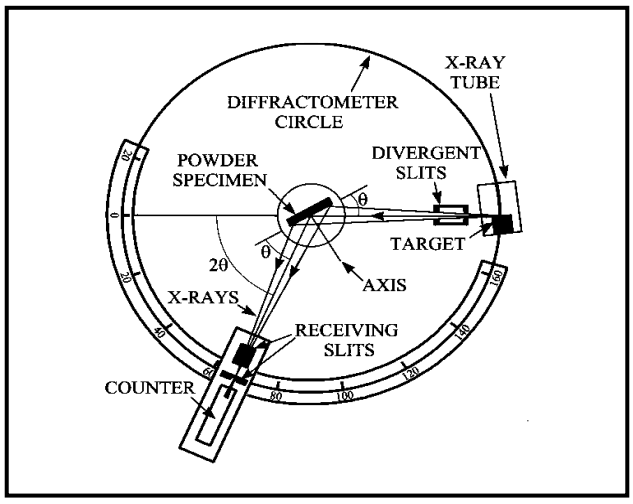

Figure 27. Geometric arrangement of the Bragg Brentano diffractometer.
Source: http://pubs.usgs.gov/of/2001/of01-041/htmldocs/images/xrdschem.jpg

It is well-known that the XRD technique provides the information on lattice parameter. If Miller indices can be assigned to the various reflections in the powder pattern, it becomes possible to determine the cell constant. These are directly related to 2θ and *h, k, l* through the relationships derived from the combination of Bragg's law and *d*-spacing expession and summarized in the table 1.

Table 1. Expression for *d*-spacing in the different crystal systems

Crystal System	Expression for d_{hkl} terms of lattice parameters and Miller indices
Cubic	$\frac{1}{d^2} = \frac{h^2 + k^2 + l^2}{a^2}$
Tetragonal	$\frac{1}{d^2} = \frac{h^2 + k^2}{a^2} + \frac{l^2}{c^2}$
Orthorhombic	$\frac{1}{d^2} = \frac{h^2}{a^2} + \frac{k^2}{c^2} + \frac{l^2}{d^2}$
Hexagonal	$\frac{1}{d^2} = \frac{4}{3}\left[\frac{h^2 + k^2 + hk}{a^2}\right] + \frac{l^2}{c^2}$
Monoclinic	$\frac{1}{d^2} = \frac{1}{\sin^2\beta}\left[\frac{h^2}{a^2} + \frac{k^2 \sin^2\beta}{b^2} + \frac{l^2}{c^2} - \frac{2hl\cos\beta}{ac}\right]$

Source: Hammond, (1990)

Crystallite size is one kind of effects that can change diffraction peak widths. As the crystallites in a powder get smaller, the diffraction peaks at a powder pattern get wider. The crystallite size is easily calculated as a function of peak width (specified as the full-width at half maximum peak intensity, FWHM), peak position and wavelength of X-ray. This is known as the Scherrer's formular:

$$D = \frac{0.9\lambda}{\beta \cos\theta} \quad (2)$$

where D is the average crystallite size, λ is the wavelength of incident X-ray, θ is the Bragg angle of diffraction lines, β is the full-width half-maximum in radians

2.1.2 Sample preparation for XRD

XRD samples should be well-ground in a mortar and pestle or a ball mill. This creates a uniform particle size and ensures that all possible crystallite orientations are present in the sample. The well-fine sample is then mounted into the sample holder. Sample's requirement for powder XRD depends on the nature of the material. A typical sample holder makes of an aluminum plate with a circle hole in the center. Normally, the sample holder is a 20 mm of diameter and a 2 mm thick. It can be modified when the sample quantity is a problem. For materials that diffract strongly (many inorganic materials), a few milligrams of the sample is then spread on the tape and smoothed flat. The tape is primarily amorphous and so does not generally interfere with the pattern being collected.

2.2. Scanning Electron Microscope

A scanning electron microscope (SEM) is basically type of electron microscope that three-dimensional-like image of the specimen surface is formed. The electrons interact with the atoms that make up the sample producing the signals that contain information about the sample's surface, topography, microstructure and particle size distribution.

2.2.1 Fundamental principles of SEM

In SEM, primary electrons are emitted by thermonically or field emission from a cathode filament (W or LaB_6) or a field emission gun (W-tip) and after that accelerated with high energy typically 1-30 KV. The electron beam must be demagnified by electron lenses and places a much smaller focused electron spot on the specimen. Two pairs of electromagnetic deflection coils (scan coils) are used to sweep the beam across the specimen (Figure 28). The magnification (M) of the image is the ratio of length of the raster on the viewing screen to the corresponding length of rester on the specimen.

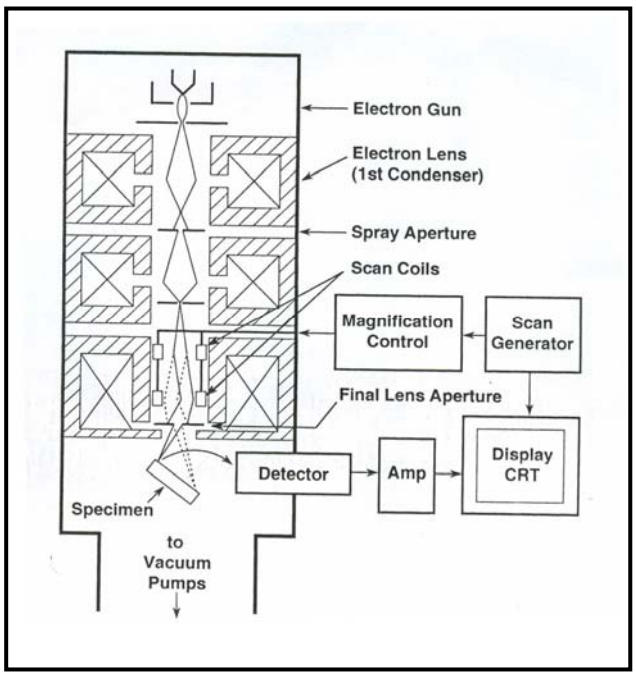

Figure 28. Schematic for a generic SEM.
Source: Goldstein *et al*., (2003)

The types of signals produced when the electron beam enters the specimen, include secondary electrons (SE), back scattered electrons (BSE), characteristic X-rays, (cathodoluminescence), specimen current and transmitted electrons as shown in figure 29. Each signal requires specialized detector for its detection that is not usually all present on a single machine. Backscattered and

secondary electrons, the principal signals used to form image in SEM, are generated within the interaction volume.

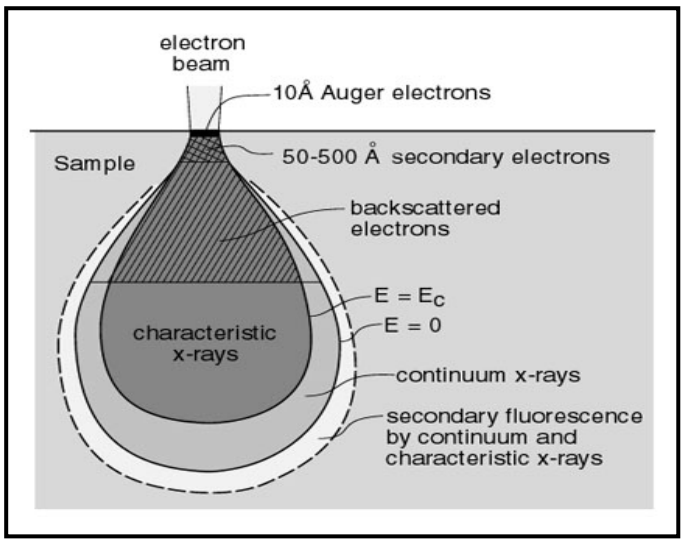

Figure 29. Generalized illustration of interaction volumes for various electron-specimen interactions.

Source: www4.nau.edu/.../Microprobe-SEM/Signals.html

Secondary electrons (SE) are loosely bound outer shell electrons from the specimen atoms which receive sufficient kinetic energy during an inelastic scattering of electrons to be ejected from the atom and set into motion. They are used for surface topographic (shape, size, surface texture) studies. The secondary electron coefficient varies with the specimen tilt angle so this effect introduces a number component to topographic contrast in the secondary electron signal.

Backscattered electrons (BSE) consist of high-energy electrons originating in the electron beam, that are reflected or back-scattered out of the specimen interaction volume by elastic scattering interactions with specimen atoms. Since heavy elements (high atomic number) backscatter electrons more strongly than light elements (low atomic number), and thus appear brighter in the image, BSEs are used to detect a contrast between areas with different chemical compositions. (http://en.wikipedia.org/wiki/Scanning_electron_microscope-10/11/2008).

2.2.2 Sample preparation for SEM

Even with a conducting specimen such as a metal, the remaining beam current must flow from the specimen to ground to avoid the accumulation of charge in the junction. It must be noted that if the path from the specimen surface to ground is broken (non-conductive sample), the electron injected into the specimen by the beam will accumulate, and the specimen will develop a high negative electrical charge relative to ground. In fact, the high resistivities of insulators prevent the smooth motion of the electron injected by the beam through the specimen to ground, so that the electrons accumulate in the immediate vicinity of the beam impact, raising the local potential. The resulting diverse set of phenomena is referred to as "charging" and leads to strong effects in SEM images.

The best and simplest way to overcome the charging problems is to deposit a thin metal layer on the surface of the sample. Sputter coating is a popular and relatively simple way of applying a coating layer of metals and their alloys to nonconductive substrates. The target material is exposed to an energized gas plasma formed from a heavy inert gas such as argon. The target surface is eroded by the plasma and atoms are ejected and collide with residual gas molecules. Target atoms have a short mean free path and provide multidirectional coating on a stationary specimen.

2.3. UV-Vis spectroscopy

Ultraviolet-visible (UV-Vis) spectroscopy uses light in the visible and near ultraviolet ranges to excite the outer electrons. At these wavelengths, molecules undergo electronic transitions. When visible or ultraviolet light is absorbed by the valence electrons of the material, these electrons are promoted from their ground states to higher energy excited states (Figure 30). The difference between the initial and final intensities is recorded. When plotted into a spectrum as wavelength against absorbance (A), the absorbance is defined by using the Beer-Lambert law as follow:

$$A = -\log (I/I_0) \quad (3)$$

where A is the measured absorbance, I_0 is the intensity of incident light at a given wavelength, and I is the transmitted intensity, respectively. Most spectrometers display an absorbance on the vertical axis, and the commonly observed range is from 0 (100% transmittance) to 2 (1% transmittance). The wavelength of maximum absorbance is a characteristic value designated as λ_{max}.

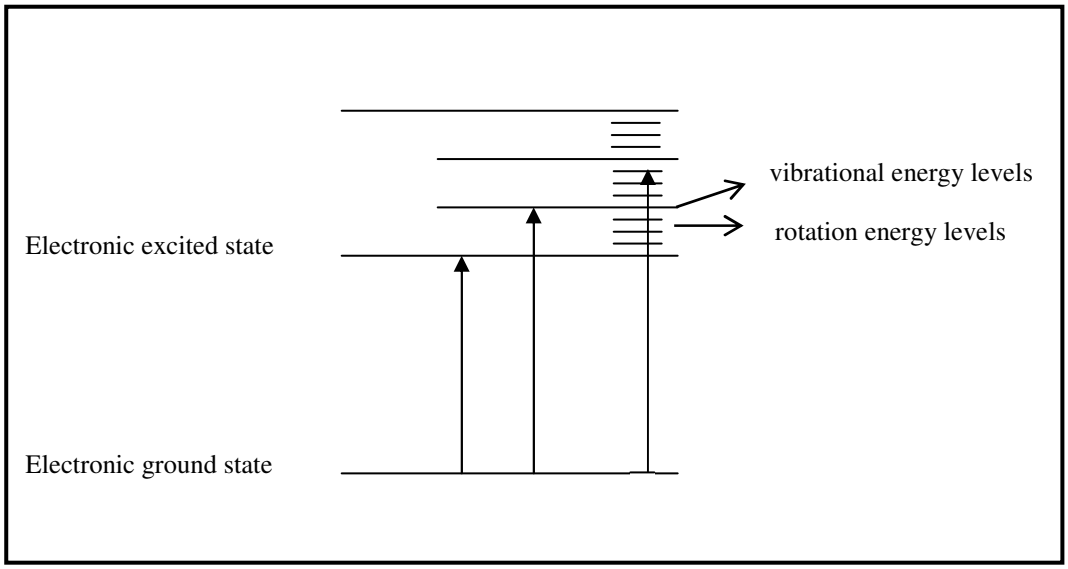

Figure 30. Illustration of the electronic transitions process during light absorption.

In this experiment, a diffuse reflected light from the sample relative to $BaSO_4$ as a white standard was corrected using an integrating sphere method as shown in figure 31.

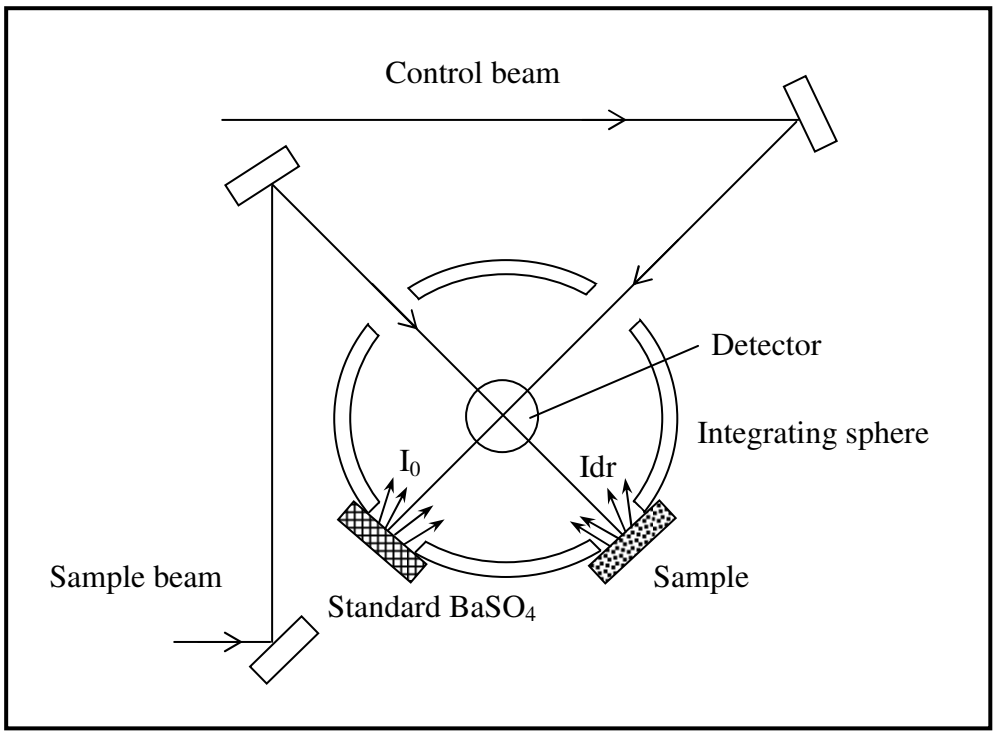

Figure 31. Solid sample measurment using the integrating sphere method.
Source: Optional Accessories for Shimadzu UV-Vis spectrophotometers

In a crystal, the band gap is defined as the minimum energy between the occupied valence band and empty conduction band. The Tauc gap is found by extrapolating the linear part of a plot of $(\alpha E)^{1/2}$ against the photon energy ($h\nu$). The intercept of this line with photon energy axis gives the value of the Tauc optical gap.

2.4. Photoluminescence

Luminescence is an emission of photon (in ultraviolet, visible or infrared region) from an electronically excited species. Various types of luminescence are classified to the mode of excitation (Valeur, 2002). Photoluminescence (PL) is a process in which a chemical compound absorbs the photon (electromagnetic radiation), thus jumping to a higher electronic energy state, and then radiates photons, returning to a lower energy states. Photo-excitation causes electrons within the material to move into permissible excited states. When these electrons return to their

equilibrium states, the excess energy is released and may include an emission of light, or luminescence.

Photoluminescence is a non-destructive and powerful technique used for characterization, investigation and detection of defects as well as measurement the band-gaps of materials. In semiconducting materials, PL involves the irradiation of the sample to be characterized with photon energy greater than band-gap energy of that material. Free electrons are created in the conduction band together with the free holes in valance band. When these carriers energetically relax down the band edge, it may do so through radiative (release of a photon) or non-radiative (no photon production) recombination. The detected luminescence signals could result from the band-to-band recombination, intrinsic crystalline defects, dopant impurities, or other extrinsic defect levels by several radiative transitions between the conduction band and valence band, exciton, donor and acceptor levels, as shown in figure 32.

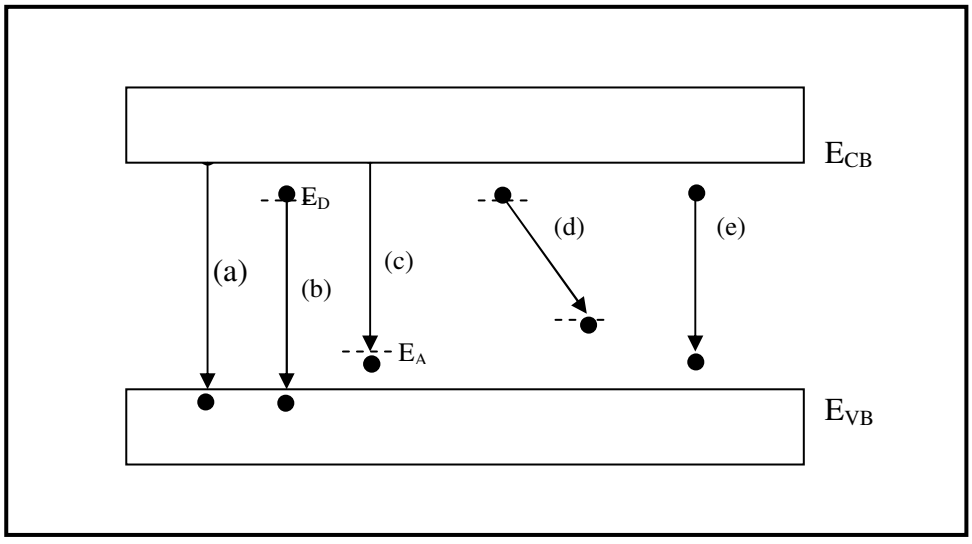

Figure 32. Schematic illustration of common recombination process. (The conduction band, E_{CB}, occupied by free electrons, and the valance band, E_{VB}, occupied by free holes, are represent in addition to donor, E_D, and acceptor, E_A trapping centers within the forbidden gap).

The first described transition is radiative band-to-band or direct recombination (Figure 32(a)), which dominates at room temperature and can be used to roughly estimate the band gap energy (E_g) of materials. The band-to-band transition contains the recombination of free electrons and free holes. This transition occurs when an electron falls from its conduction band state into the empty valence band state associated with the hole. For indirect band gap semiconductors, a band-to-band recombination process is unlikely because the electrons at the bottom of the conduction band have a non zero crystal momentum with respect to the holes at the top of the valence band.

Such transition involving the electrons trapped on the donors and holes, are known as bound-exciton (Figure 32(b)). An electron bound to a donor can recombine directly with a free hole from a valence band. This kind of recombination is called free-to-bound (FB) transition (Figure 32(c)).

When both donor and acceptor impurities are present in semiconductors, coulombic interaction between a hole bound to an acceptor recombines with an electron bound to a donor in donor-acceptor pair (DAP) transition (Figure 32(d)). Both the donor and the acceptor are neutral before the recombination (i.e. the dornor positively and the acceptor negatively charged).

Excitonic recombination can occur following the generation of an electron-hole pair. Coulombic attraction lends to the formation of an excited state in which an electron and the hole remain bound to each other in a hydrogen-like state, refered to as a free exciton (Figure 32(e)).

The basic components of a photoluminescence spectrometer are shown schematically in figure 33. The excitation source is a special xenon flash tube, which produces an intense, short duration pulse of radiation over the spectral range of the instrument. Energy from the source is focused by the ellipsoidal mirror and reflected by the toroidal mirror onto the entrance slit of the excitation monochromator. A narrow wavelength band emerges from the exit slit, with the center wavelength being

determined by the setting of the grating, the angle of which is controlled by a stepper motor. The majority of the excitation beam is transmitted to the sample via the focusing toroidal mirror, a small proportion is reflected by the beam splitter onto the referent photodiode. Energy emitted by the sample is focused by the toroidal mirror onto the entrance slit of the emission monochromator and go to detector.

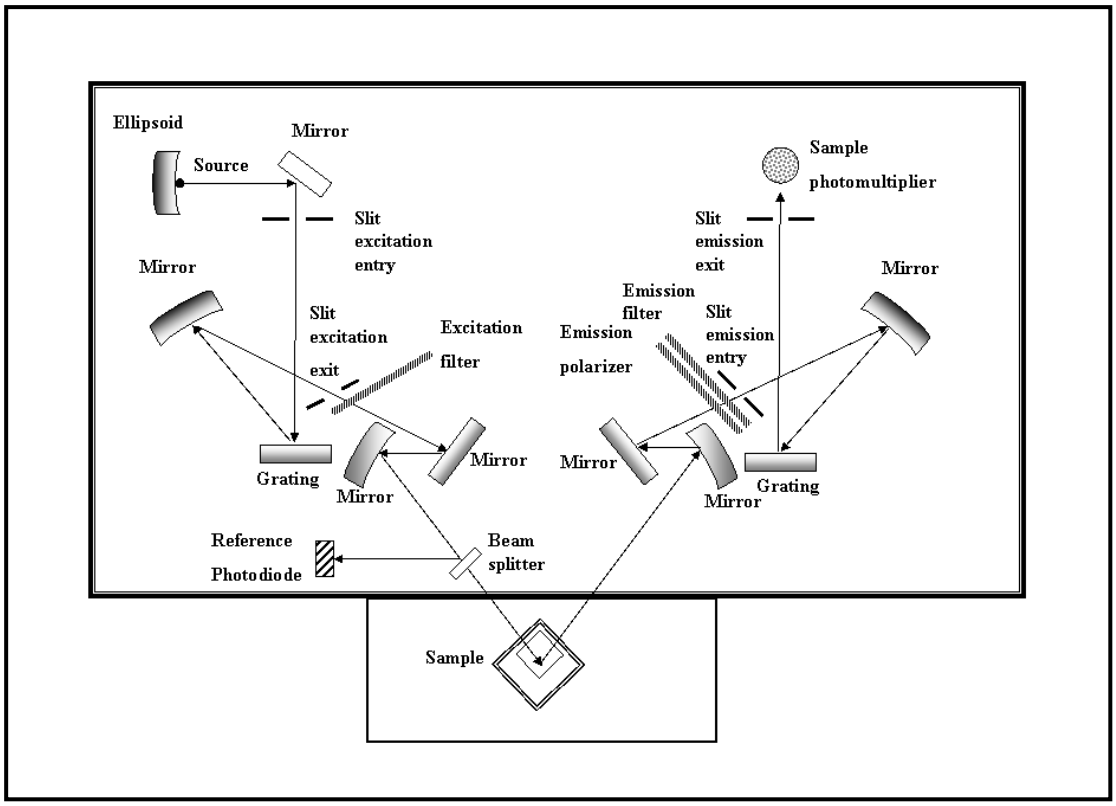

Figure 33. The optical layout.

Source: Perkin Elmer Inc., (2000)

CHAPTER 3

EXPERIMENTAL

3.1. Chemicals and Reagents

Chemicals and reagents used in this work were purchased from various suppliers as shown in Table 2.

Table 2. List of chemicals and reagents.

Chemicals and reagents	Supplier
Zinc acetate dihydrate, AR grade	Fluka, Japan
Sodium dodecyl sulfate, AR grade	Fluka, Japan
Sodium hydroxide, AR grade	Merck, Germany
Jeffamin® M-1000 Polyetheramine or Polyethylene oxide -b- polypropylene oxide	Huntsman, USA
Hydrochloric acid 37%, AR grade	J.T. Baker, USA
Ethanol 99.9% AR grade	Merck, Germany

3.2. Instruments

3.2.1. X-ray diffraction (XRD)

X-ray diffraction patterns were recorded from the Philips X'Pert MPD diffractometer.

3.2.2. Scanning electron microscope (SEM)

The shape and size of all samples were measured by a JEOL, JSM-5800 LV scanning electron microscope.

3.2.3. Field emission scanning electron microscope (FESEM)

The shape and size of sample was measured by a Hitachi, S-4700 field emission scanning electron microscope.

3.2.4. Thermogravimetric analyzer (TGA)

Weigh loss as a function of temperature was studied by a Perkin Elmer, TGA 7 thermogravimetic analyzer.

3.2.5. Ultraviolet-visible (UV-Vis) spectrophotometer

Absorption spectra of ZnO powders were measured from a Shimadzu, UV- 2450 spectrophotometer.

3.2.6. Luminescence spectrometer

Room temperature luminescence of ZnO powder was investigated by a Perkin Elmer, LS 55 luminescence spectrometer.

3.2.7. Fourier-transformed infrared (FTIR) spectrophotometer

Organic impurity in prepared ZnO powder was detected by a Perkin Elmer, Spectrum GX Fourier-transformed infrared spectrophotometer.

3.2.8. Other equipments and apparatus

3.2.8.1. Analytical balance

A Mettler Toledo, AB204.S balance with significant of ± 0.0001 g was used to weigh chemicals all experiments.

3.2.8.2. pH meter

In order to control the pH of solution, a Mettler Toledo, seveneasy pH meter was used to measure a pH value and to indicate the volumn of NaOH which was added in the solution.

3.2.8.3. Oven

A Memmert oven was used to dry the sample at 100 ^{o}C for 1 h before calcination.

3.2.8.4. Furnace

A Carbolite RWF1300 furnace was used to calcine the sample with a suitable temperature for 1 h.

3.3. Procedure

3.3.1. Preparation of 0.20 M of Zn^{2+} solution

Zn^{2+} solution was prepared by dissolving 6.58 g of $Zn(C_2H_3O_2)_2.2H_2O$ in 150 mL of distilled water.

3.3.2. Preparation of 0.40 M of NaOH

Sodium hydroxide solution was prepared by dissolving 2.40 g of NaOH in 150 mL of distilled water.

3.3.3. Synthesis of ZnO

3.3.3.1. SDS - modified solution

4.32 g or 8.64 g of SDS was added into a homogeneous Zn^{2+} solution with continuous stirring so that the mole ratio of Zn^{2+}: SDS equal to 1:0.5 and 1:1, respectively, were obtained. 0.40 M NaOH was added dropwise to each SDS-modified Zn^{2+} solution until the pH value reached 8, 10 or 12. The mixtures or solutions were continuously stirred at 70 ^{o}C for 1 or 5 h before being cooled to room temperature. The precipitates were filtered, rinsed with distilled water several times then collected and dried at 100 ^{o}C for 1 h and finally calcined at a suitable temperature for 1 h.

3.3.3.2. PEO-*b*-PPO - modified solution

3.00 g of PEO-*b*-PPO (MW 1000) was added into a homogeneous Zn^{2+} solution with continuous stirring so that the mole ratio of Zn^{2+} : PEO-*b*-PPO = 1:0.1 was obtained. 0.40 M NaOH was added dropwise to each PEO-*b*-PPO-modified Zn^{2+} solution until the pH value reached 8, 10 or 12. The mixtures or solutions were continuously stirred at 70 ^{o}C for 1 h before cooling to room temperature. The precipitates were filtered, rinsed with distilled water several times then collected and finally dried at 100 ^{o}C for 1 h.

3.3.4. Characterization of ZnO powder

3.3.4.1. Phase identification

Phase formation and crystal structure evolution were characterized by XRD technique. The samples were ground and pressed in a sample holder. The XRD measurement was operated in a normal mode without rotating the sample. Intensity was measured at an interval of 0.02^{o} over 2θ range of 28-72^{o} using CuK_{α} radiation. The XRD operating parameters for all samples are shown in Table 3.

Table 3. XRD operating parameters.

Parameters	Value
Step size	0.02
Time per step	1 s
Divergent slit	0.5^o
Anti-scattering slit	1^o
Receiving slit	0.4 nm
Voltage	40 kV
Current	30 mA

3.3.4.2. Morphology of ZnO powder

Samples were mounted on a carbon tape which was placed on a braze stub. Because of a lack in conductivity of ZnO powder, they were coated with Au for 3 s by sputtering method. A morphology of sample was examined using an accelerating voltage of 20 kV. Both shape and size of samples were investigated from the secondary electron micrograph at the suitable magnification.

3.3.4.3. Absorption study

Solid samples were ground and pressed in a sample holder. A diffuse reflected light from the sample relative to white $BaSO_4$ standard was corrected from 200-800 nm with $\Delta\lambda$= 0.5 nm using an integrating sphere method.

3.3.4.4. Luminescence study

Solid samples were ground and placed onto the silica window of a sample screw holder. Photoluminescent spectra were detected in a range of 200-800 nm.

3.3.4.5. Thermal behavior

Thermal study was investigated by TGA technique. Weigh loss as a function of temperature was studied in a range of 50-1300 ^{o}C under nitrogen atmosphere with heating rate of 10 ^{o}C per minute.

3.3.4.6. Organic impurity identification

The functional groups of impurity phase were identified by FTIR in a transmission mode at 4500-400 cm^{-1}. The solid samples were ground with KBr and pressed to form a platelet.

CHAPTER 4

RESULTS AND DISCUSSION

The effect of sodium dodecyl sulfate (SDS) and poly(ethylene oxide)-*b*-poly(propylene oxide) (PEO-*b*-PPO) copolymer on morphological control of nanocrystalline ZnO particles and their optical properties have been investigated by different techniques such as X-ray diffractometer, scanning electron microscope, UV-Vis spectrophotometer and photoluminescence spectrometer.

In this work, the single step of hydrolysis reaction of $Zn(C_2H_3O_2).2H_2O$ at low temperature was used to synthesize the nanocrystalline ZnO particles. By this method, a number of processing steps are reduced and the calcination process at high temperature is not required. After stopping the reaction, as-prepared samples from the PEO-*b*-PPO-modified $Zn(C_2H_3O_2)_2.2H_2O$ solution with a pH range between 8 - 12 show a single phase in good agreement with the wurtzite ZnO structure. Nevertheless, the single phase formed from the SDS-modified $Zn(C_2H_3O_2)_2.2H_2O$ solution at pH 12 only. Then, the results of different stabilizers or capping agents in controlling the ZnO shape will be discussed separately.

4.1. Use of SDS

4.1.1. Structure of as-prepared ZnO powders

4.1.1.1. Without SDS

After the as-prepared samples were dried at 100 ^{o}C for 1 h, the phase identification was detected by XRD in a range of 28 – 72 degree as shown in figure 34. All diffraction peaks of the as-powders prepared from the precursor solution at a pH value between 8-12 were similar to hexagonal or wurtzite ZnO structure with a space group $P6_3mc$. The obtained structure was in good agreement with the JCPDS

file of ZnO (JCPDS 36-1451). With the result obtained, it was evident that none of impurity phase was observed in XRD patterns. From figure 34, the diffraction peaks of ZnO samples were broadened when pH values were increased because of the decreasing of their crystallite size. The crystallite size of ZnO particles calculated by the Scherrer equation were 53.34 ± 3.25 nm (pH 8), 48.98 ± 2.24 nm (pH 10) and 41.98 ± 5.02 nm (pH 12). The reduction of crystallite size is in accordance with a decrease of ZnO particle sizes observing by SEM as shown in figure 35.

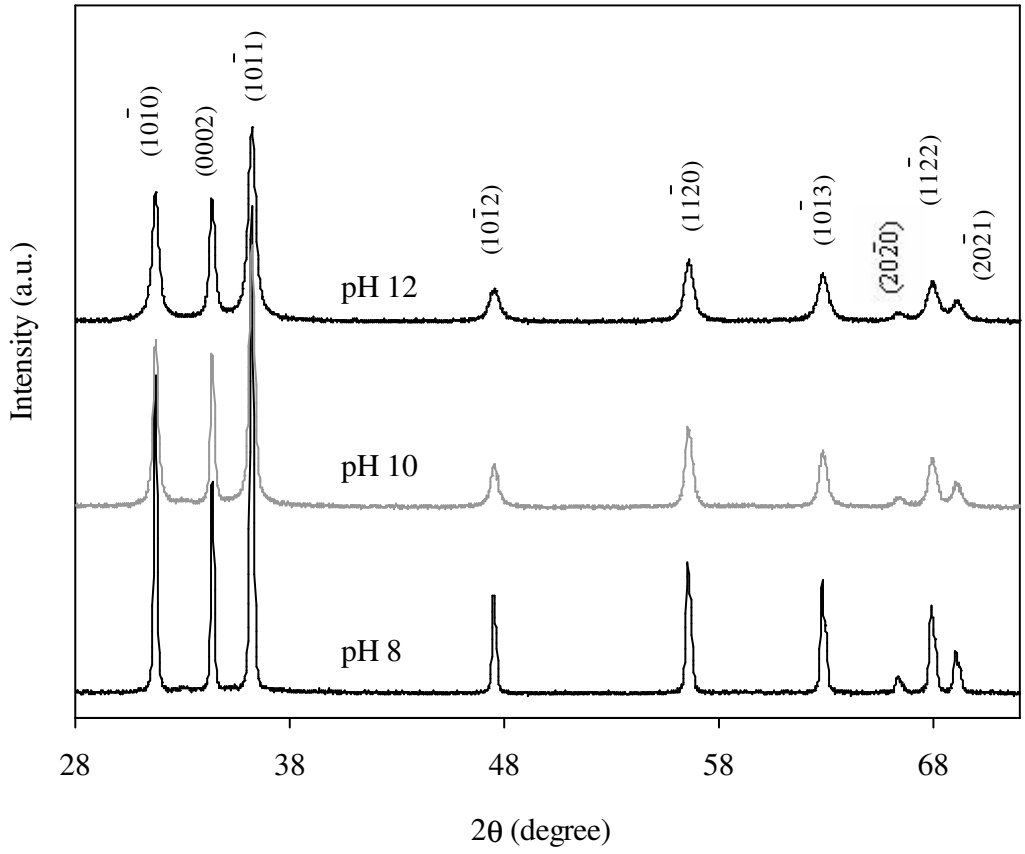

Figure 34. XRD patterns of as-prepared ZnO powders without addition of SDS in the solutions at the pH value of 8 – 12 before calcination process.

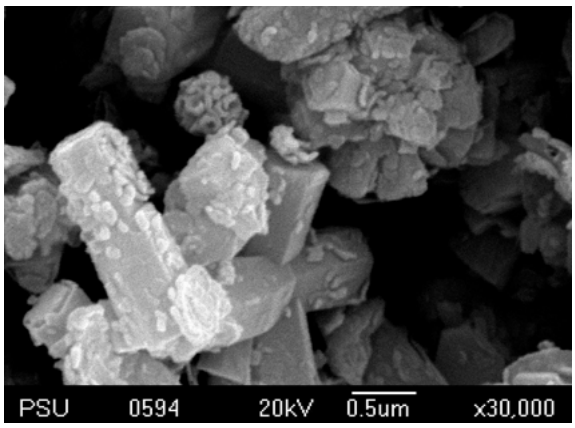

pH 8

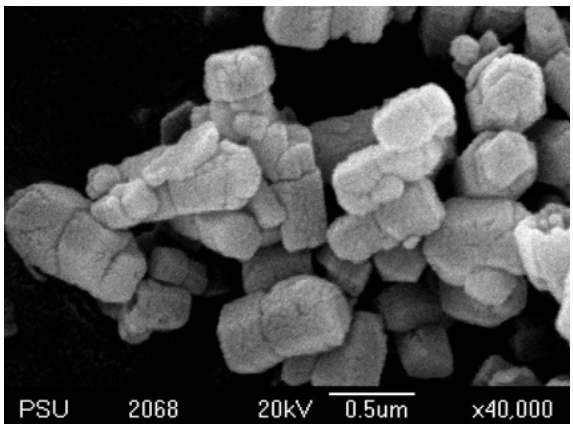

pH 10

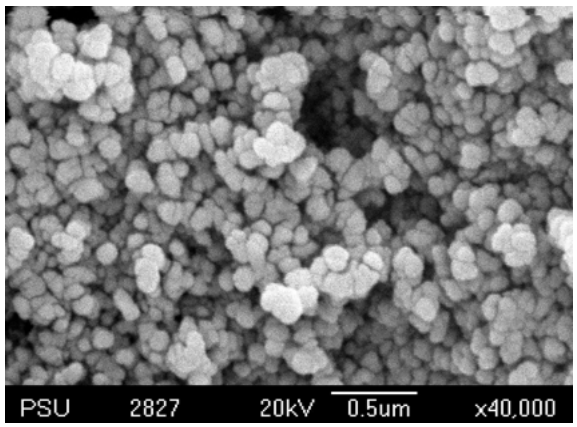

pH 12

Figure 35. SEM images of ZnO powders without addition of SDS in the solutions at the pH value of 8 – 12 before calcination process.

4.1.1.2. With SDS

To study the effect of SDS, the mole ratio of Zn^{2+}:SDS at 1:1 was first considered to evaluate a possibility of morphological control and aging time (if ZnO is not formed).

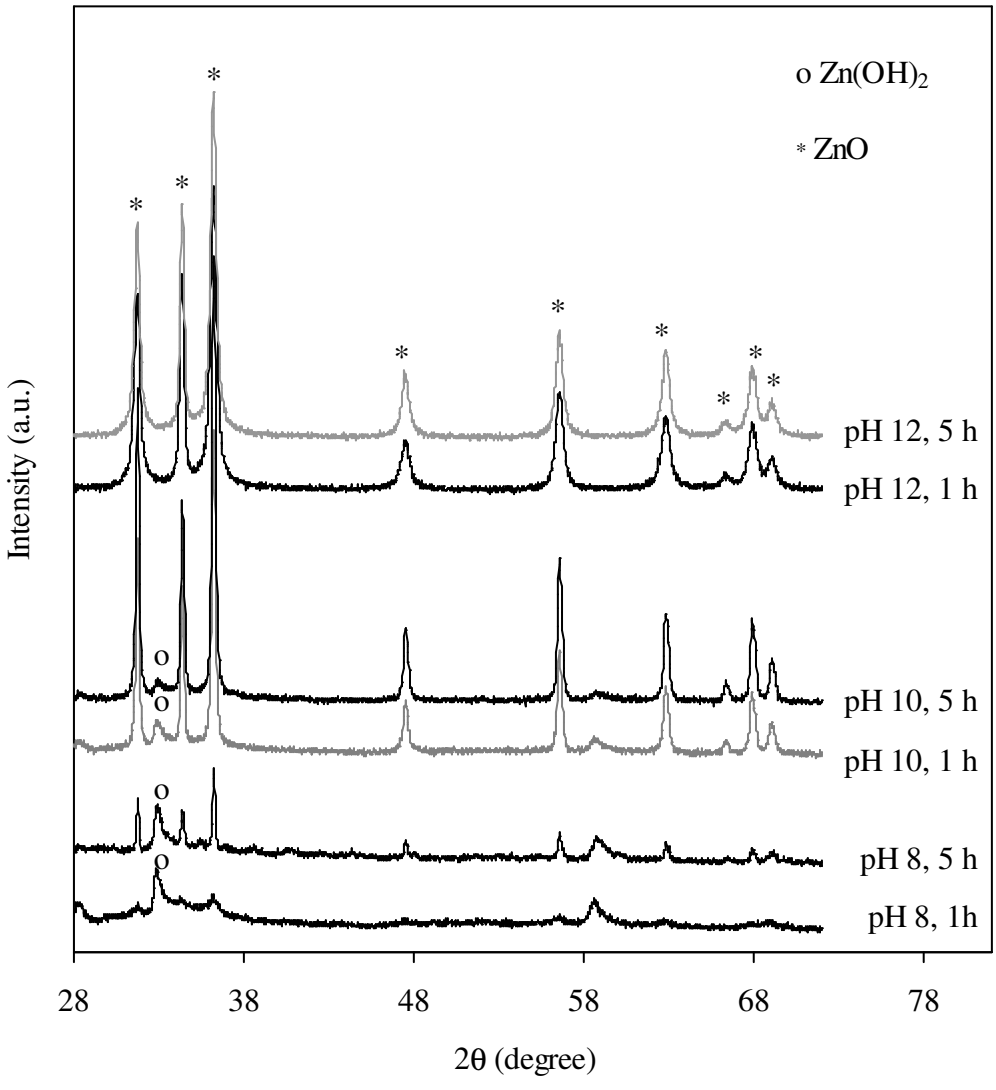

Figure 36. XRD patterns of as-prepared powders synthesized at a mole ratio of Zn^{2+}:SDS = 1:1 in the pH range of 8 – 12 at different aging times before calcination process.

From a previous section, pure ZnO phase prepared from the solution without addition of SDS formed before calcinations process. On the other hand, the as-powders prepared from the SDS-modified $Zn(C_2H_3O_2)_2.2H_2O$ solution at a pH value of 8-12 with a mole ratio of Zn^{2+}:SDS = 1:1 showed a variety of XRD patterns as shown in figure 36. As seeing in figure 36, a single phase of ZnO occurred at a pH value of 12 only. In contrast, the as-powders prepared from the solutions at a pH value of 8 and 10, showed the diffraction pattern of both ZnO and $Zn(OH)_2$. Herein, the ratio of the present ZnO and $Zn(OH)_2$ phases was estimated by peak intensity. This ratio increased as higher pH of solution was used. Indeed, $Zn(OH)_2$ is not a stable phase and it then transformed to ZnO indicated by a decreasing of peak intensity of $Zn(OH)_2$ and an increasing of peak intensity of ZnO when an aging time was prolonged.

Owing to the presence of $Zn(OH)_2$ as an intermediate phase in the XRD patterns, the thermal behavior of sample was recorded by TGA with a heating rate of 10 ^oC/min under a nitrogen atmosphere to study the sample decomposition. Figure 37 shows the nature of the pyrolysis process of SDS-modified ZnO particles prepared from precursor solution with a mole ratio of Zn^{2+}: SDS equal to 1:1 at pH 8. The first weight loss of 3.45% near 100 ^oC was ascribed to the release of adsorbed moisture. The second weight loss of 29.5% between 153 and 185 ^oC was ascribed to the dehydration of crystal water and the pyrolization of excess SDS. The third weight loss of 13.14% between 577 and 700 ^oC indicated that the entire SDS had been pyrolized so the SDS molecules bonded with the as-precipitates were eliminated by the heat and the ZnO phase formed simultaneously and completely. The last weight loss at a temperature over 1,100 ^oC might be referred to the decomposition of the nanocrystalline ZnO particles. From the result obtained, the calcination temperature was selected at 900 ^oC. Under this condition, the XRD patterns of the calcined samples (pH = 8 and 10) showed only a single ZnO phase (data will be shown in the section 4.1.2.1.).

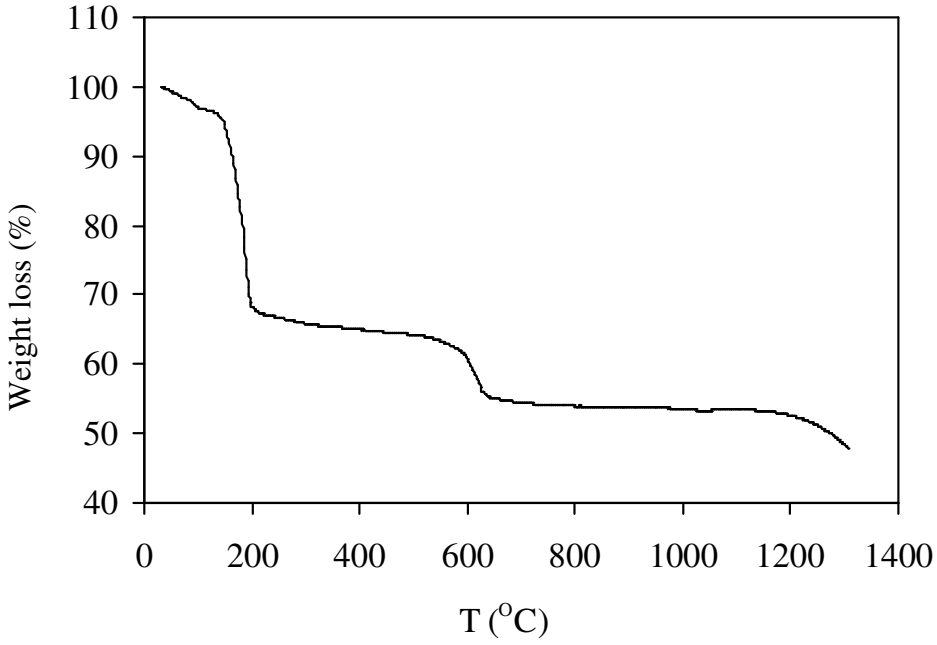

Figure 37. TGA curve of as-prepared powder from solution at pH 8 and a mole ratio of Zn^{2+}:SDS = 1:1.

4.1.2. Structure and morphology of calcined ZnO powders

4.1.2.1. Without SDS

After as-prepared ZnO powders were calcined at 900 ^{o}C in a conventional furnace, phase identification and morphology of the powders were examined by XRD and SEM techniques. From XRD patterns in figure 38, the diffraction peaks of the hexagonal wurtzite ZnO structure with a space group $P6_3mc$ were still observed.

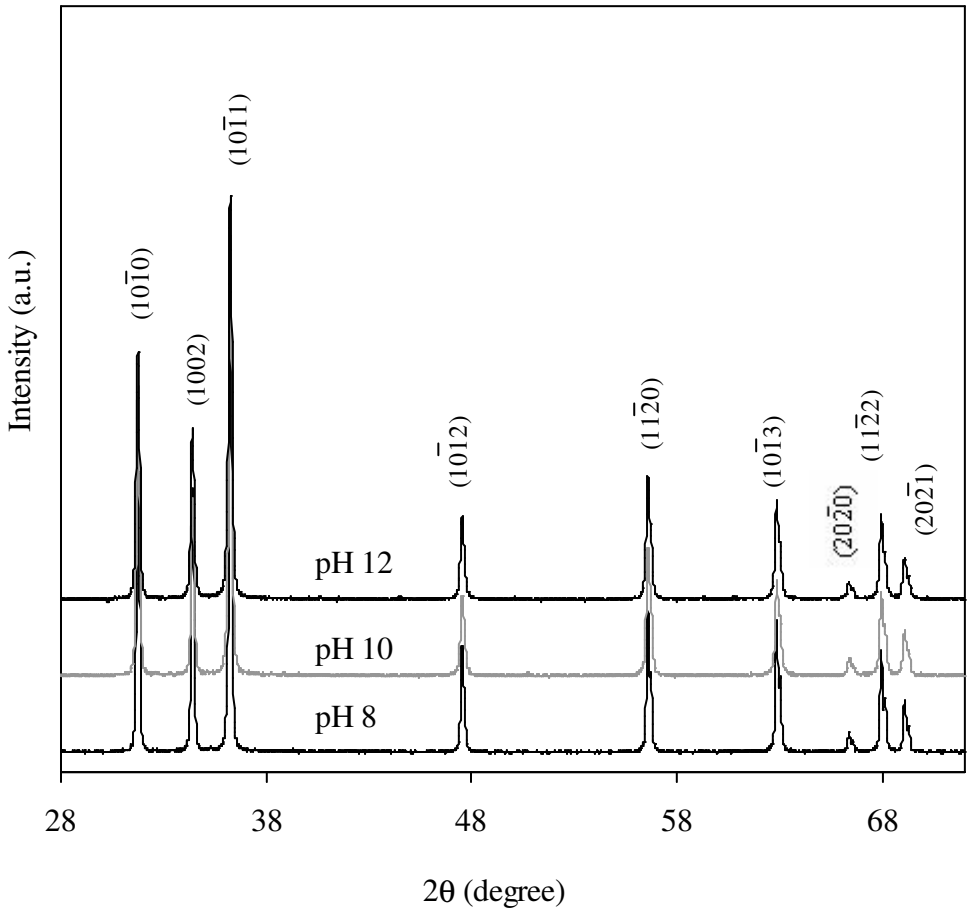

Figure 38. XRD patterns of calcined ZnO powders prepared at pH 8 – 12.

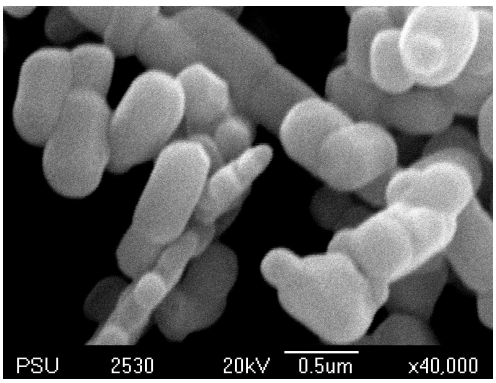

pH 8, 1h

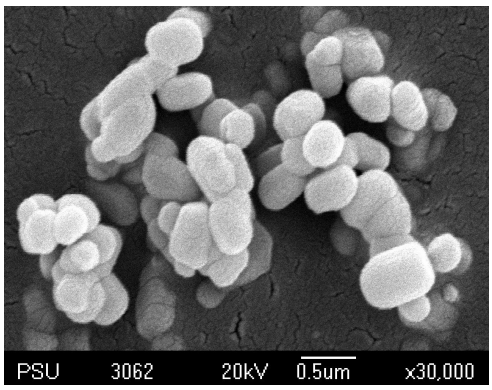

pH 8, 5h

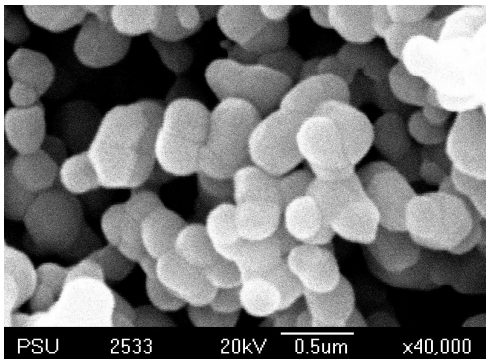

pH 10, 1h

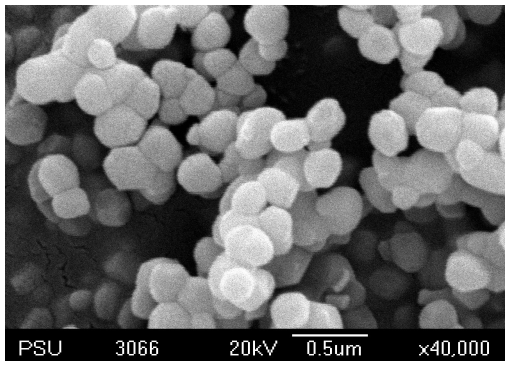

pH 10, 5h

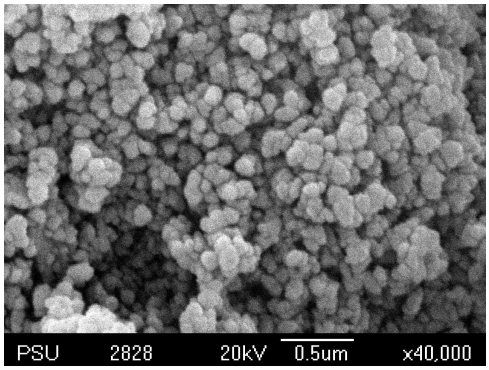

pH 12, 1h

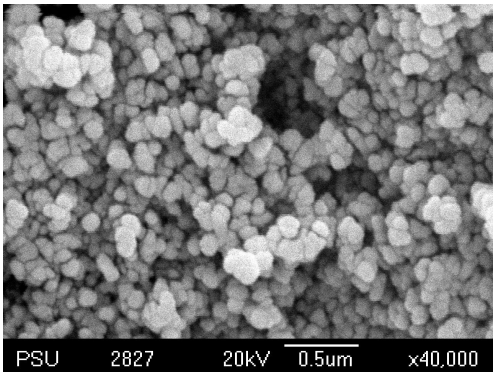

pH 12, 5h

Figure 39. SEM images of calcined ZnO powders prepared at different pH values and aging times from the precursor solution without addition of SDS.

From figure 38, an increase of peak intensity comes from a crystalline phase formation at high temperature. The crystallite size of the calcined ZnO particles were 49.26 ± 0.95 (pH 8), 48.39 ± 0.83 (pH 10) and 45.31 ± 1.18 (pH 12) nm when calculating from the peak broadening. The decrease of crystallite sizes was in good agreement with the reduction of particle size observed by SEM.

In this study, variety of ZnO shapes can be observed in SEM images as shown in figure 39. At pH 8, a typical small rods of ZnO were observed. The length of these rods decreased when a pH of solution was increased as seen in the SEM image of ZnO prepared from the solution at pH 10. At pH 12, the ZnO particles altered to an agglomerated spherical shape. Normally, small particles are easy to agglomerate to form a bigger particle so as to reduce a total surface energy.

4.1.2.2. With SDS

In this section, the SDS concentration and the aging time were varied in order to study the effect of SDS on morphological change of ZnO.

From the TGA curve in the figure 37, the suitable calcining temperature for ZnO formation was selected at 900 ^{o}C except the sample was prepared from the precursor solution at pH 12, it was examined without calcining process because ZnO phase occurred directly. In this section, the effect of SDS concentration and aging time on morphology of ZnO was studied under different conditions as described in Table 4.

Table 4. Variation of SDS concentration, aging time and pH of solution for synthesis ZnO powders.

pH of solution	mole ratio of Zn^{2+}:SDS	aging time (h)	calcining temperature (^{o}C)
8	1:0.5	1	900
	1:0.5	5	900
	1:1	1	900
	1:1	5	900
10	1:0.5	1	900
	1:0.5	5	900
	1:1	1	900
	1:1	5	900
12	1:0.5	1	-
	1:0.5	5	-
	1:1	1	-
	1:1	5	-

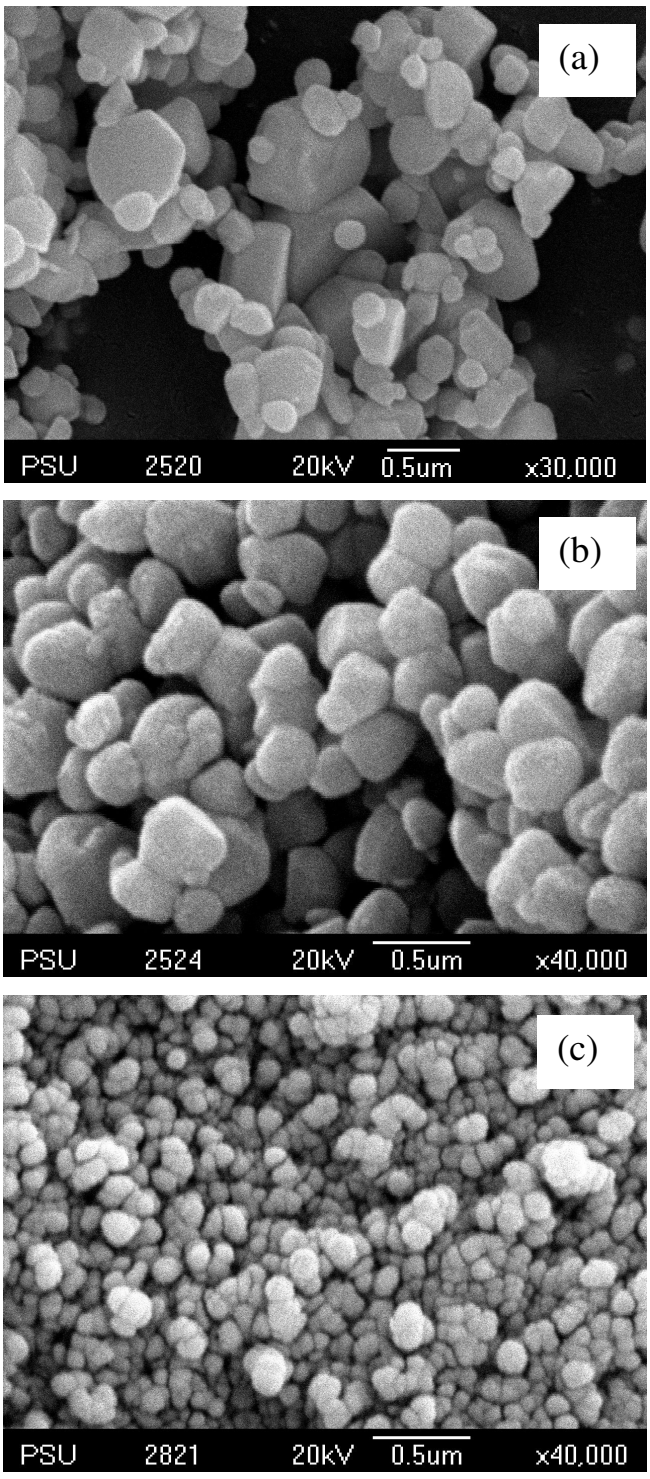

Figure 40. SEM images of calcined ZnO particles prepared from SDS modified-$Zn(C_2H_3O_2)_2.2H_2O$ solution with a mole ratio of Zn^{2+}:SDS =1:0.5 and aging time for 1 h at different pH values (a) pH 8, (b) pH 10 and (c) pH 12.

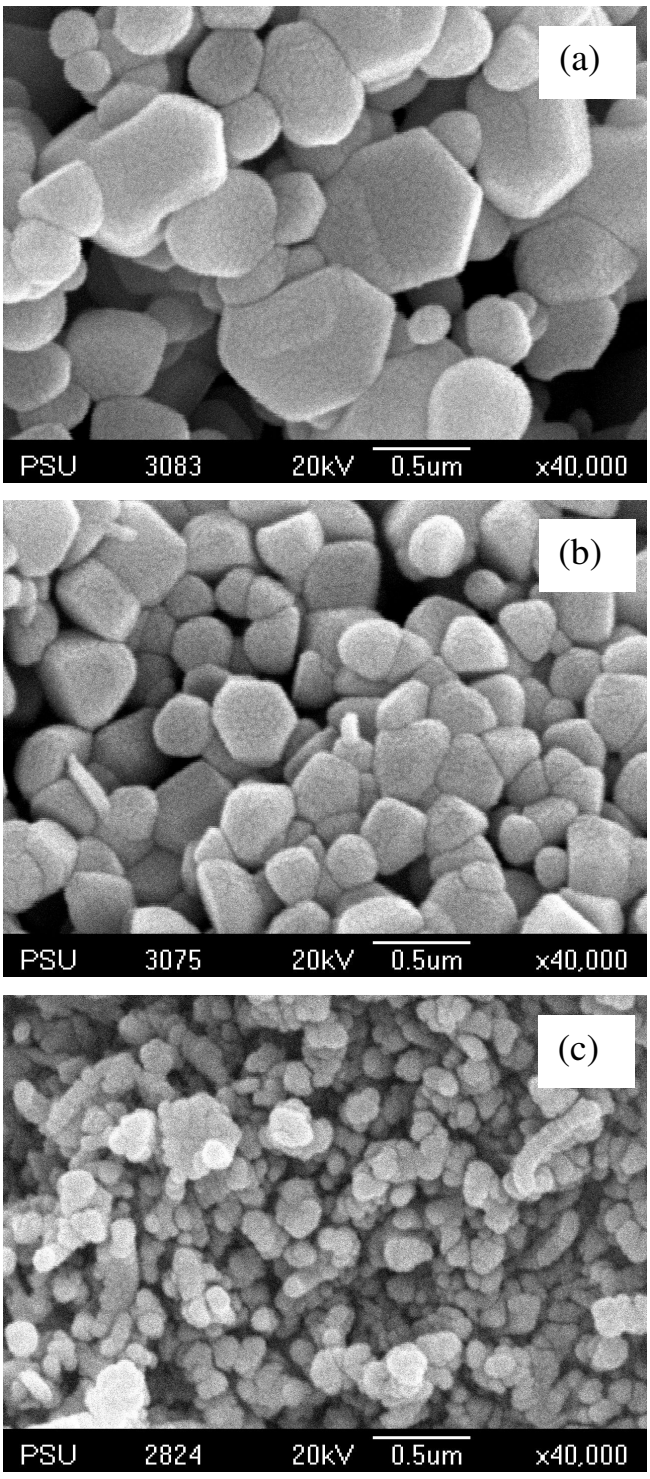

Figure 41. SEM images of calcined ZnO particles prepared from SDS modified-$Zn(C_2H_3O_2)_2.2H_2O$ solution with a mole ratio of Zn^{2+}:SDS =1:1 and aging time for 1 h at different pH values (a) pH 8, (b) pH 10 and (c) pH 12.

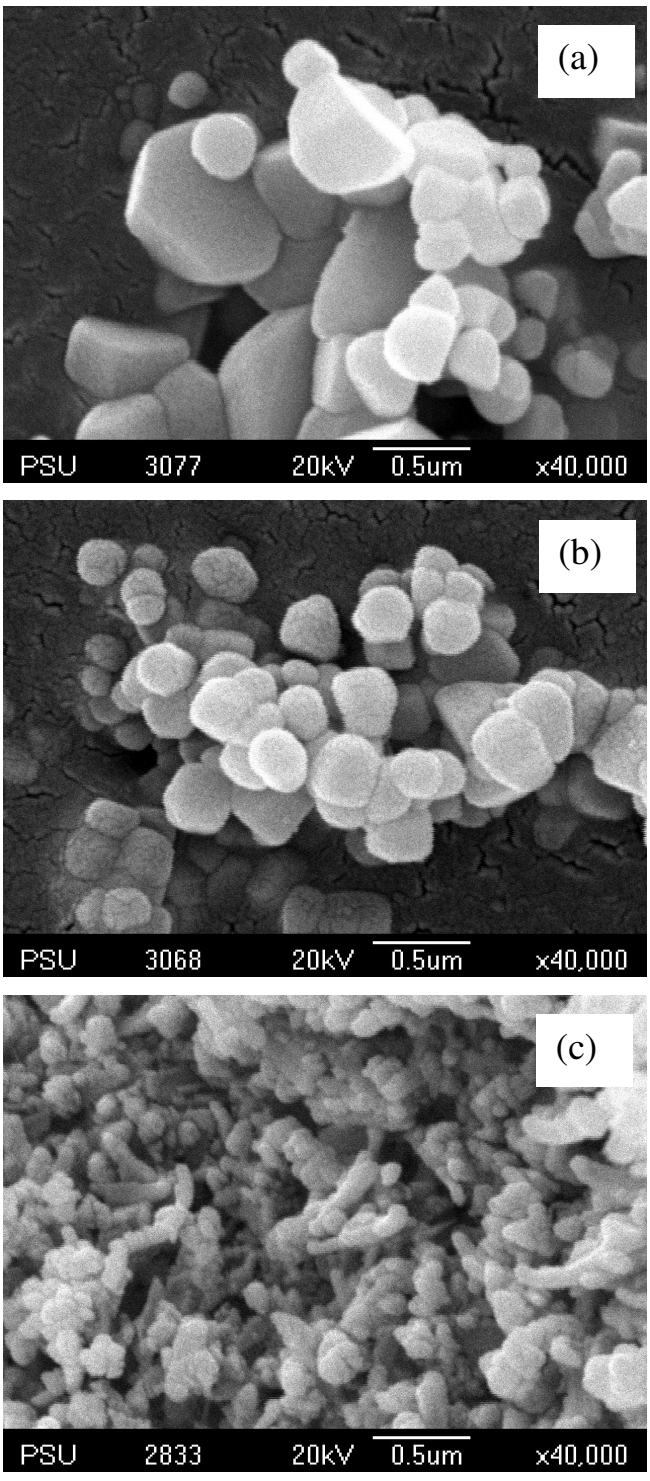

Figure 42. SEM images of calcined ZnO particles prepared from SDS modified-$Zn(C_2H_3O_2)_2.2H_2O$ solution with a mole ratio of Zn^{2+}:SDS = 1:0.5 and aging time for 5 h at different pH values (a) pH 8, (b) pH 10 and (c) pH 12.

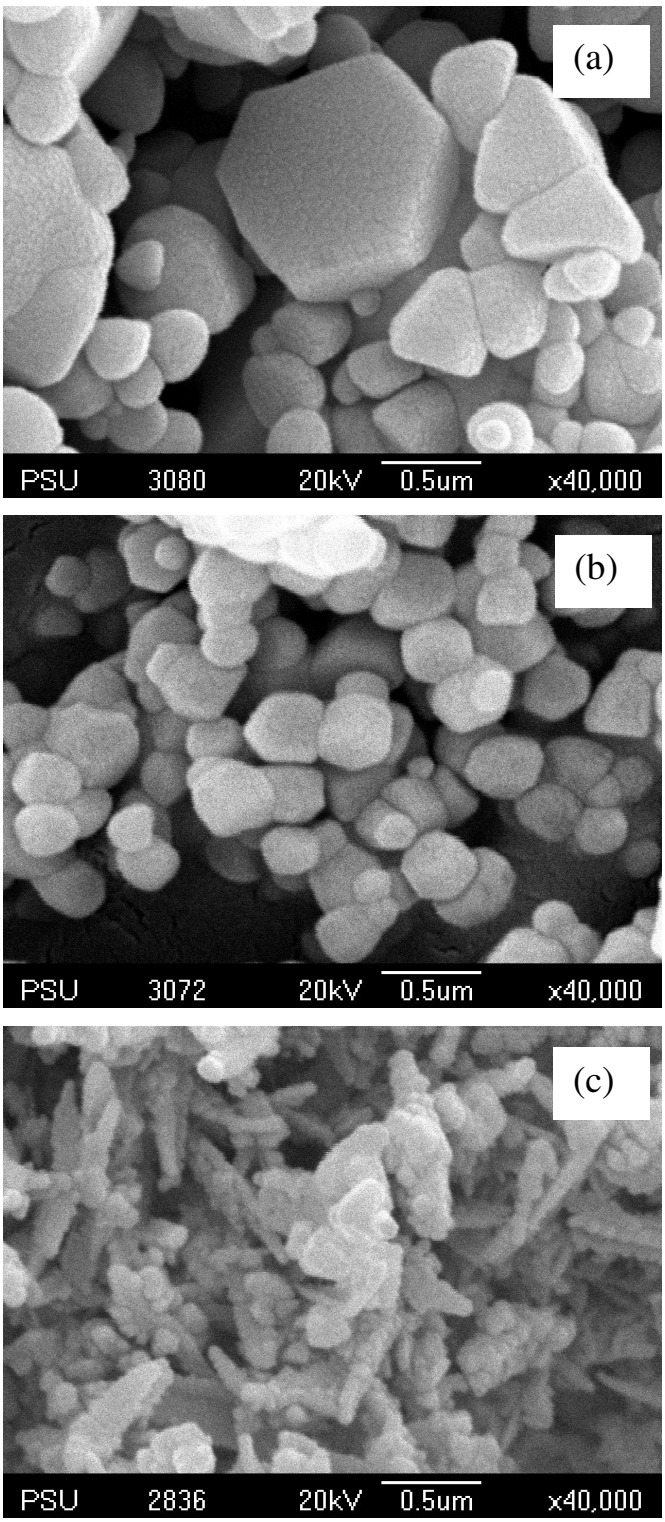

Figure 43. SEM images of calcined ZnO particles prepared from SDS modified-$Zn(C_2H_3O_2)_2.2H_2O$ solution with a mole ratio of Zn^{2+}:SDS =1:1 and aging time for 5 h at different pH values (a) pH 8, (b) pH 10 and (c) pH 12.

The SEM images of calcined ZnO (pH 8, 10) and as-prepared ZnO (pH 12) particles synthesized from the SDS-modified-$Zn(C_2H_3O_2)_2.2H_2O$ solution at different mole ratios of Zn^{2+}:SDS and aging times were presented in figure 40 – 43. From the SDS-modified $Zn(C_2H_3O_2)_2.2H_2O$ solution, the calcined ZnO particles prepared from the precursor solutions at pH 8 and 10 formed a hexagonal prism-like shape however a small rod-like shape was observed from as-prepared ZnO particles (pH 12)

At pH 8, a diameter of hexagonal facet of the hexagonal prism-like particle increased as a function of SDS concentrations. This diameter further increased when an aging time was prolonged. A hexagonal prism-like ZnO particle prepared from precursor solution at pH 10 was smaller in size compared to ZnO particle occurred at pH 8. As aging times and SDS concentrations were increased, the shape of ZnO particles formed a small hexagonal prism obviously. However, the dimension of these particles did not significantly change when an aging time and SDS concentration were increased. At pH 12, the hexagonal prism-like shape of ZnO particles tended to form a spherical-like shape when a mole ratio of Zn^{2+}: SDS was increased. With increasing of aging time to 5 h, the rod-like shape agglomerated from the small spherical particles, can be observed in SEM images.

4.1.3. The mechanism for ZnO formation

In this section, the possible mechanism for ZnO formation has been proposed. From the previous results, the ZnO particles prepared from the solution without addition of SDS at pH 8-12 can form. When the SDS was added into the solution at pH 8 and 10, both ZnO and $Zn(OH)_2$ phases formed as clearly observed in XRD pattern.

The formation of ZnO particles from the hydrolysis of Zn^{2+} ions in an aqueous media has been known that it is very complex process. Many polyvalent cation species between Zn^{2+} ions with OH^- ions can form and strongly depend upon the pH of the solution. At equilibrium, the fraction of ion species existing as Zn^{2+}, $Zn(OH)^+$, $Zn(OH)_2$, $Zn(OH)_3^-$ and $Zn(OH)_4^{2-}$ over a range of pH between 6 – 14 at 25 ^oC was shown in figure 44.

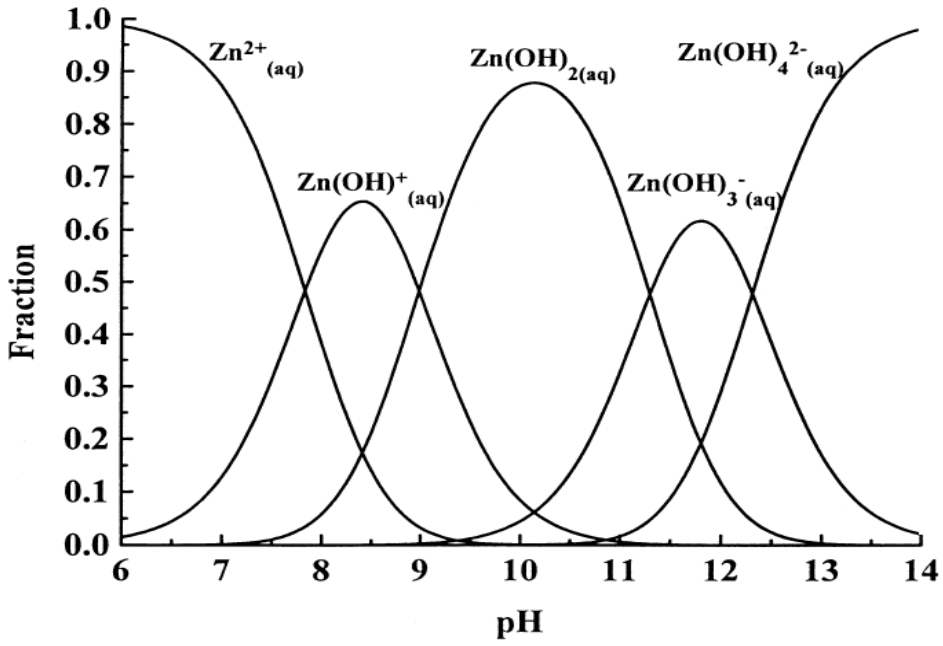

Figure 44. Fraction of Zn (II) ions species between pH 6 - 14 at 25 ^oC.
Source: Degen *et al*., (2000)

However, the precipitation of ZnO particle has been usually described through a term of growth unit that might be either $Zn(OH)_2$ or $Zn(OH)_4^{2-}$ ions depending on a pH of solution, temperature and synthetic method. The growth of ZnO particle from $Zn(OH)_2$ species has been usually suggested through the dissolution-reprecipitation mechanism however it is still ambiguous. For a novel process, although many explanations in growing of ZnO particle from $Zn(OH)_4^{2-}$ ions are very simple to understand, this mechanism can be used under a strong alkaline solution. This was proven by Y. Wei *et al* (Xie *et al*., 2008). They proposed that ZnO can grow from the $Zn(OH)_2$-$Zn(OH)_4^{2-}$ species if the mole ratio of Zn^{2+}:OH^- was in a range of 1:4-1:7 and the precursor existed only $Zn(OH)_4^{2-}$ ions if a mole ratio of Zn^{2+}:OH^- was between 1:8-1:9.

In the absence of SDS, particle size of ZnO depended upon OH^- concentration or pH of the solution if the condition was done at the same temperature. At pH 8, $Zn(OH)_2$ acted as the growth species formed and transformed to ZnO. Considering the anisotropic growth as mentioned in Chapter 1, so the particle was induced to form a bipyramidal-like shape. However, another shape such as tetrapod and radial shapes could occur by a linking of bipyramidal ZnO as clearly seen in figure 35, because of the inhomogeneity of the reaction. At pH 10, the growth species were partially dissolved and the size was then smaller. $Zn(OH)_2$ species can easily dissolve to $Zn(OH)_4^{2-}$ when increasing of the OH^- concentration and then they transformed to ZnO. Under strong alkaline solution, another shape was observed due to a different growth species as presented in figure 35.

At pH 12, the white precipitate (colloidal) as $Zn(OH)_2$ could form after mixing the Zn^{2+} and OH^- solutions. These species are rather instable at high pH value and could further dehydrated and transformed to ZnO as described in many publications (Xie *et al*., 2008; Xiao *et al*., 2008; Yamabi *et al*., 2002; Jitianu *et al*., 2007). Rate of ZnO transformation depended on temperature and pH of the solution. In this work, the ZnO formation was completed within 1 h. However, the experiment was not done at an aging time less than 1 h. It was evident that the $Zn(OH)_2$ phase

was not detected by XRD if the samples were prepared from the solution with/without addition of SDS at pH 12.

Based on a speciation diagram of ZnO (figure 44), $Zn(OH)^+$ ions are dominant species at pH 8. So, it can interact with OH^- ion easily to form $Zn(OH)_2$ whereas $Zn(OH)_2$ species are the most population observing from a speciation diagram at pH 10. However, by using a simple calculation at 25 ^oC, the maximum $Zn(OH)_2$ precipitation was achieved only when the pH value is between 8 and 11 (Goia *et al*., 2007). From the XRD patterns of as-prepared ZnO samples synthesized from solution without SDS molecules at pH 8 and 10, it was found that no secondary phase other than ZnO was observed but the existence of both ZnO and $Zn(OH)_2$ phases can be detected when preparing the sample from the SDS-modified $Zn(C_2H_3O_2)_2.2H_2O$ solution. In this study we proposed that SDS molecules probably adsorbed on the $Zn(OH)_2$ surface and this phenomena could depress a conversion of $Zn(OH)_2$ to ZnO. Thus, the $Zn(OH)_2$ phase was still observed in XRD pattern even through the solution was aged for 5 h. However, these species can be destabilized at higher pH value by dehydration and transformation to ZnO reactions. Then, the ZnO phase is the most population observing from XRD pattern for the sample prepared from the precursor solution at pH 10. In the absence of SDS molecules, $Zn(OH)_2$ species can dissolve and ZnO subsequently formed. Therefore, $Zn(OH)_2$ phase cannot be detected in the XRD patterns (Li *et al*., 2005).

As a matter of fact, $Zn(OH)_2$ is a good adsorbent and it is possible to be adsorbed by SDS molecules. This adsorption can be detected by FT-IR spectrophotometer. The comparison of IR transmittance spectra of SDS and all as-powders prepared from SDS-modified $Zn(C_2H_3O_2)_2.2H_2O$ solution at different pH values was displayed in figure 45. The band at around 1200 cm^{-1} assigned to S=O stretching vibration of $-SO_4$ from SDS molecule (Singh *et al.,* 2008; Michaelis *et al.,* 2006). The peaks at around 2920, 2852, 1468 and 1083 cm^{-1} are due to C-H stretching and bending. A broadening peak at around 3440 cm^{-1} is proposed due to H-OH stretching. The peak at 470 cm^{-1} is a characteristic peak of Zn-O stretching (Singh *et al.,* 2008), which is not observed in spectrum of pure SDS. It is noteworthy that no

characteristic peak of SDS is observed from the IR spectrum of ZnO sample prepared from the solution at pH 12. This result is in good agreement with the results from XRD analysis as previously mentioned. From these results, the characteristic of vibrational frequency of SDS was found in the samples prepared from the solutions at pH 8 and 10. Therefore, the obtained result could insist that the SDS could adsorb on $Zn(OH)_2$ surface. On the other hand, if the dissolution rate of $Zn(OH)_2$ species to $Zn(OH)_4^{2-}$ is very fast, the SDS molecules could not adsorb because of the electrostatic repulsion between the negative charge of hydrophilic group of SDS and $Zn(OH)_4^{2-}$ species. Then, no SDS was detected in the as-prepared sample prepared from precursor solution at pH 12.

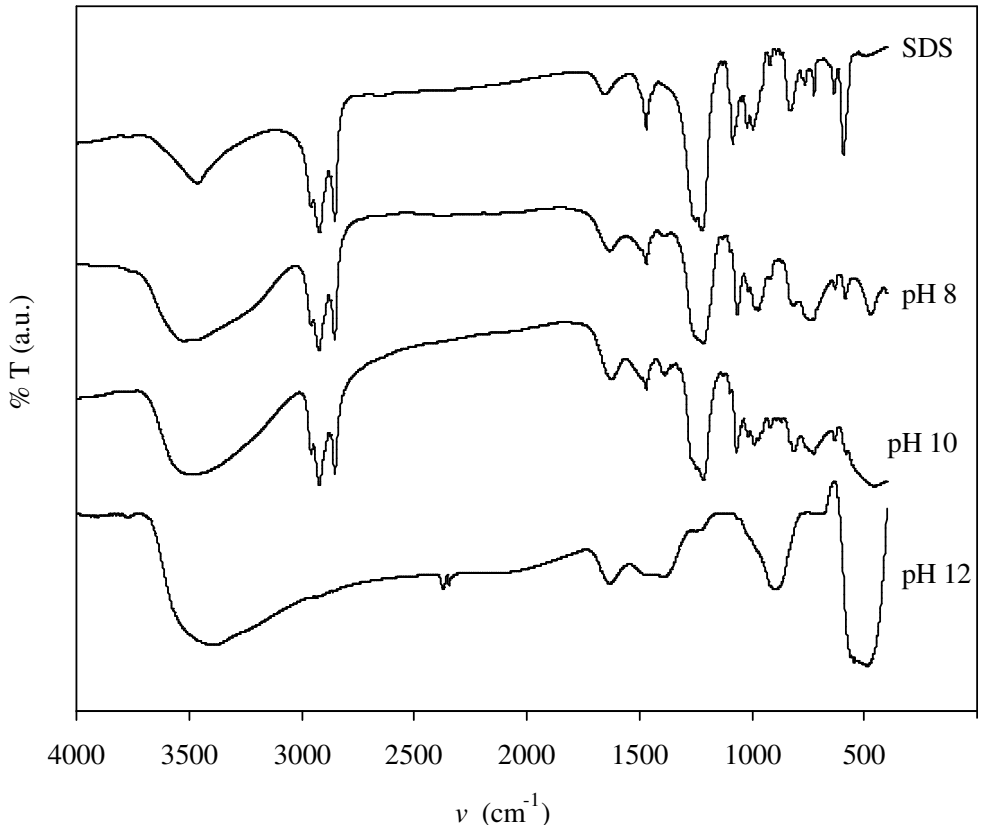

Figure 45. FT-IR spectra of SDS (a) and the as-powders prepared from the SDS-modified Zn^{2+} solution at (b) pH 8, (c) pH 10 and (e) pH 12.

Indeed, ZnO is a polar crystal which a positive polar (0001) plane rich in Zn^{2+} cations and a negative polar $(000\bar{1})$ plane rich in O^{2-} anions. By the solution method, the velocity of crystal growth in the different direction was reported to be: $V(0001) > V(\bar{1}01\bar{1}) > V(\bar{1}010) > V(\bar{1}011) > V(000\bar{1})$ (Li, *et al*., 2005). The hydrophilic group of SDS in the solutions at pH 8 and pH 10 may adsorb with Zn^{2+} of $Zn(OH)_2$ due to the electrostatic interaction. After $Zn(OH)_2$ transformed to ZnO, this position is the (0001) plane in ZnO crystal. So the growth along the *c*-axis or (0001) plane was retarded. Furthermore, the growth along the opposite face was not favorable due to the lowest growth rate on $(000\bar{1})$ face. For this reason, particle could grow in the *ab* or prism plane, giving rise to a formation of hexagonal prism-like shape. If the dissolution rate of $Zn(OH)_2$ species is faster, the smaller diameter of hexagonal-prism shape formed (pH = 10). In this experiment, the aggregated rod-like structure formed at pH 12 as shown in figure 43(c). It was observed that small rod-like structures were mostly made up of particles by the self-aligned spherical particles (Yang *et al*., 2007). Moreover, we also found that the individual rod-like structure within a local region seem to be randomly oriented. At pH 12, SDS molecules cannot adsorb on the growth unit ($Zn(OH)_4^{2-}$) because of the electrostatic repulsion, and then the growth along the *c*-axis of the anisotropic crystal is favorable (Li *et al*., 1999). This is in good agreement with another publication in which no hexagonal prism shape (high diameter and short length) could form at high pH (Li *et al*., 2008). Herein, the incorporated SDS in as-prepared ZnO powder was not either observed in XRD pattern and IR spectrum.

4.1.4. Optical properties of ZnO powders

4.1.4.1. Band gap estimation

To estimate the band gap value, the absorbance characteristic of nanocrystalline ZnO powders prepared from the solution modified with SDS was investigated by a UV-Vis spectrophotometer. The absorption was measured as a

function of wavelength in a range of 200-800 nm. All prepared ZnO powders showed a highly transparent mode in a visible region as shown in figure 46 – 48.

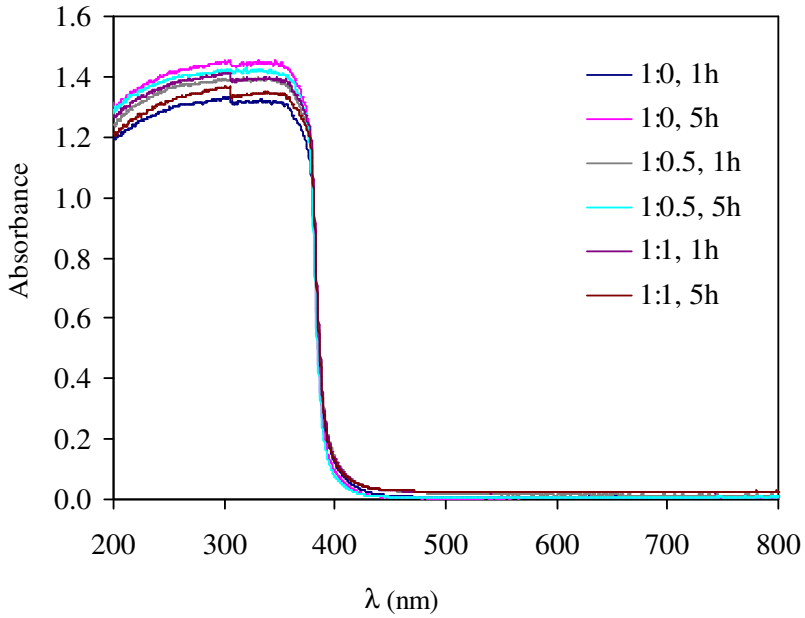

Figure 46. Absorption spectra of calcined ZnO powder prepared at different mole ratios of Zn^{2+}: SDS and aging times at pH 8.

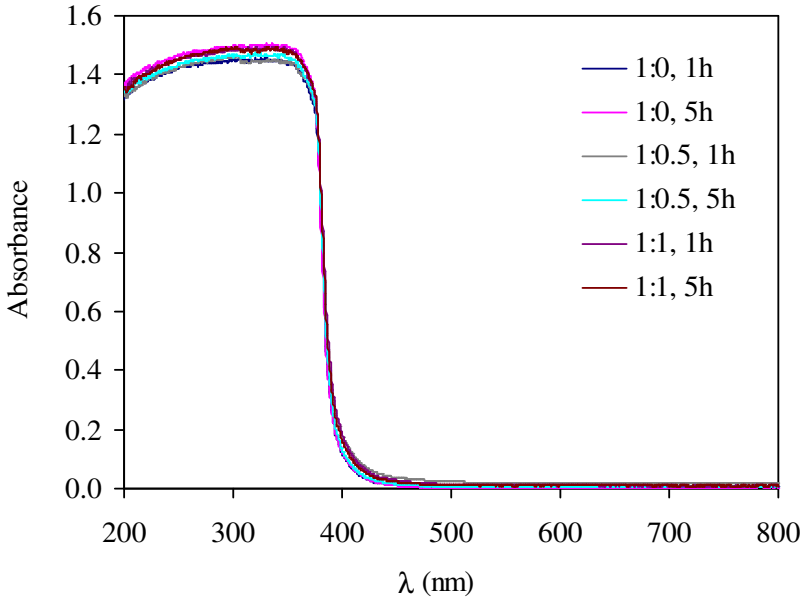

Figure 47. Absorption spectra of calcined ZnO powder prepared at different mole ratios of Zn^{2+}: SDS and aging times at pH 10.

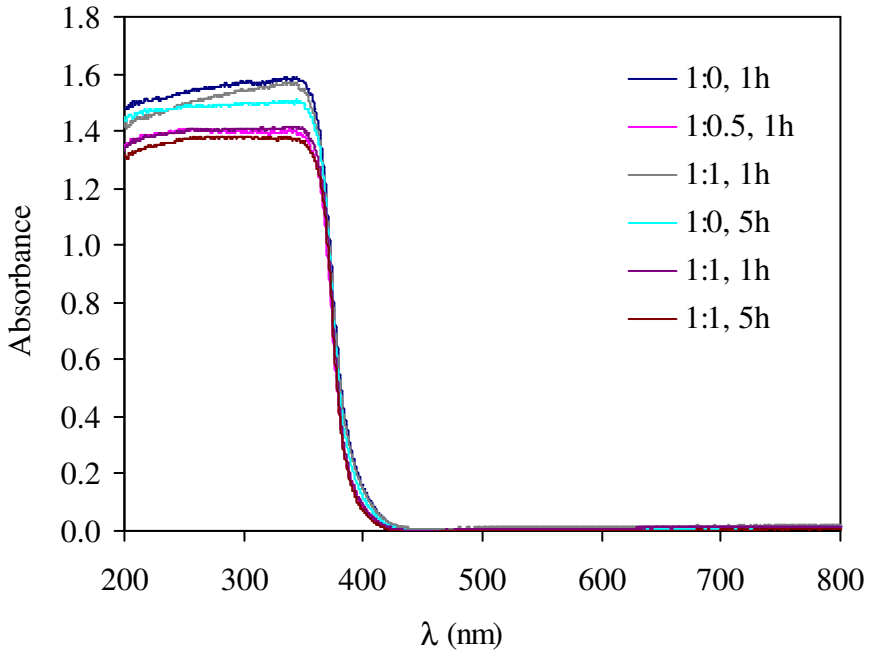

Figure 48. Absorption spectra of as-prepared ZnO powder prepared at different mole ratios of Zn^{2+}: SDS and aging times at pH 12.

Based on the absorption spectra, the direct band gap of nanocrystalline ZnO powders could be estimated from the relationship: (Serpone *et al*., 1995)

$$(\alpha h\nu)^2 = E_D(h\nu - E_g) \tag{4}$$

where α is the optical absorption coefficient, h is the Planck's constant, ν is the frequency of the incident photon, E_D is the constant and E_g is the direct band gap. In general, the absorption coefficient (α) could be evaluated by the following equation

$$\alpha = \frac{A}{d_s'} \tag{5}$$

where A is the measured absorbance and d_s' is the thickness of samples (0.4 cm) and E ($h\nu$) or photon energy could be approximated by

$$E = h\nu = \frac{1240}{\lambda} \quad (6)$$

where λ is the measured wavelength in nm.

From figure 46 – 48, the absorption below 400 nm is assigned to the intrinsic band gap absorption of ZnO due to electron transition from valence band to conduction band. Estimated direct band gap according to K-M model was calculated from a plot of $(\alpha h\nu)^2$ *vs.* photon energy ($h\nu$) as described above. Extrapolation of the linear part until its intersects the $h\nu$-axis gives an E_g value. Figure 49 – 51 showed the graph of $(\alpha h\nu)^2$ *vs.* $h\nu$ for all nanocrystalline ZnO powders obtained in this study. The values of direct band gap obtained from the linear portion of the curves were presented in table 5.

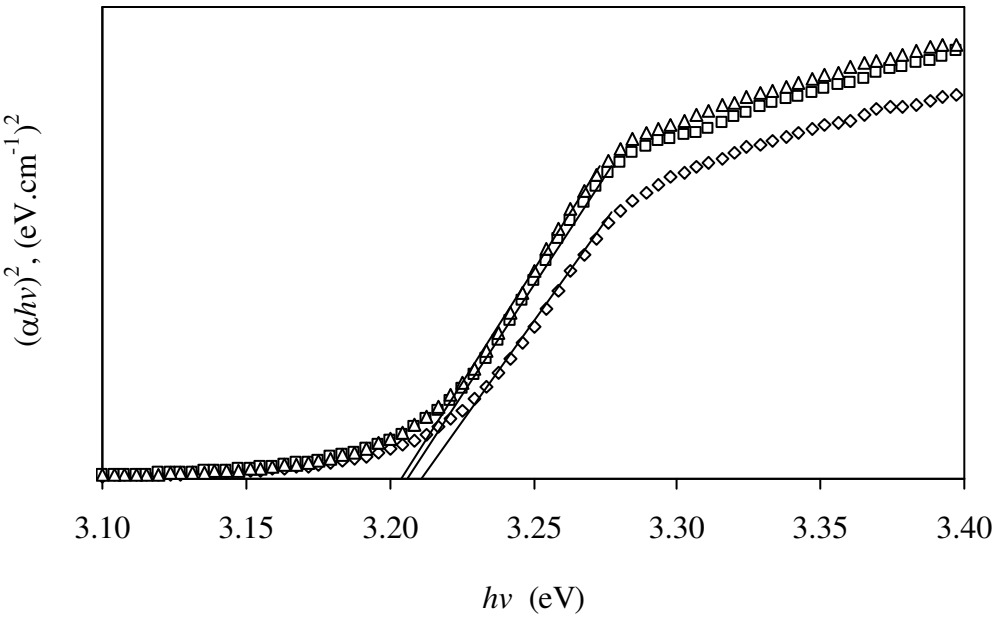

Figure 49. Evolution of $(\alpha hv)^2$ *vs. hv* of calcined ZnO particles prepared from the solution at pH 8 for 1 h. The mole ratios of Zn^{2+}:SDS are 1:0 (◇), 1:0.5 (□) and 1:1 (Δ), respectively.

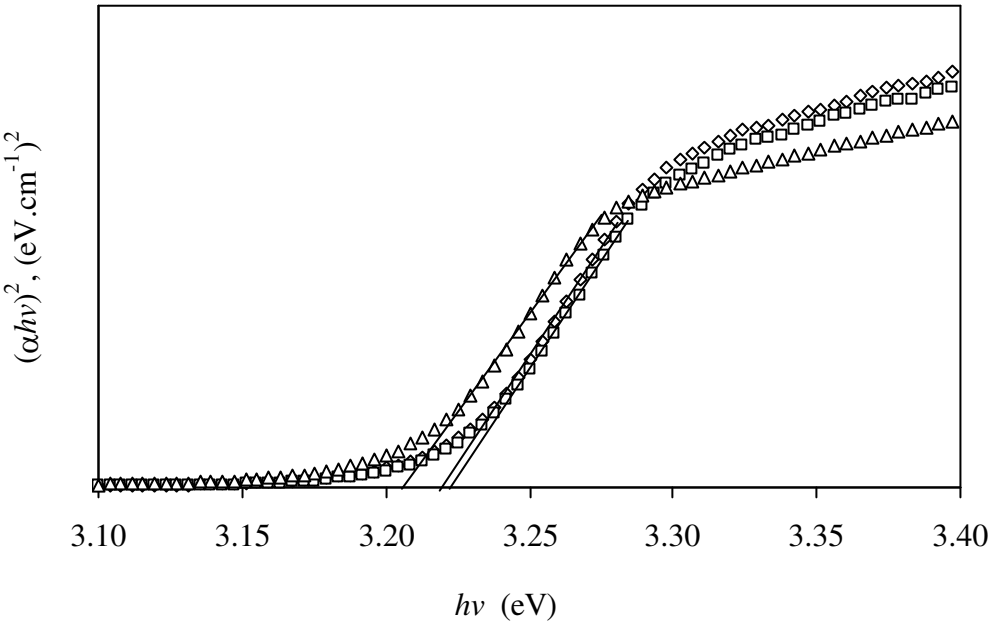

Figure 50. Evolution of $(\alpha hv)^2$ *vs. hv* of calcined ZnO particles prepared from the solution at pH 8 for 5 h. The mole ratios of Zn^{2+}:SDS are 1:0 (◇), 1:0.5 (□) and 1:1 (Δ), respectively.

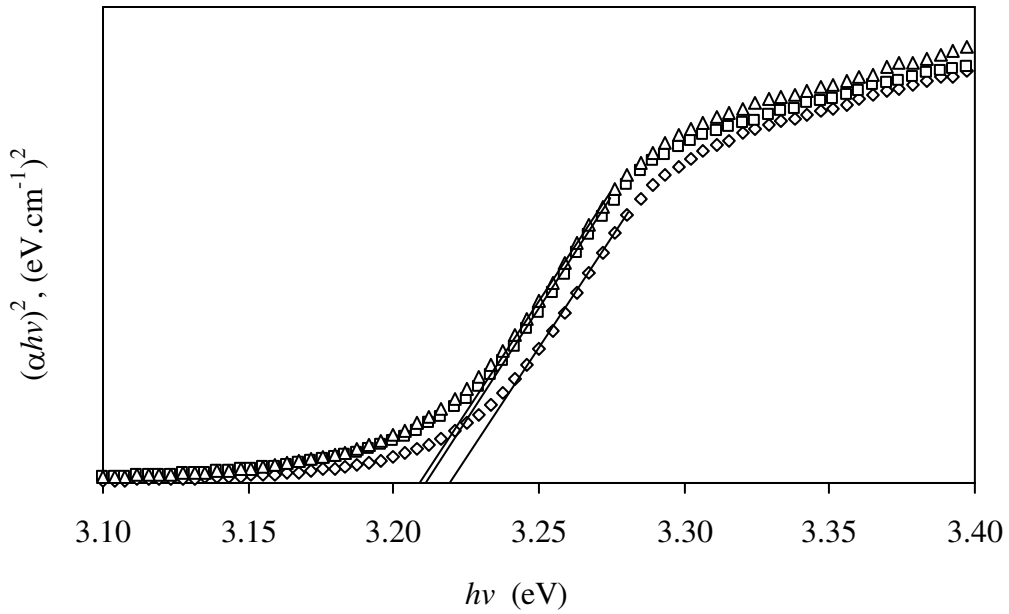

Figure 51. Evolution of $(\alpha hv)^2$ *vs. hv* of calcined ZnO particles prepared from the solution at pH 10 for 1 h. The mole ratios of Zn^{2+}:SDS are 1:0 (◇), 1:0.5 (□) and 1:1 (Δ), respectively.

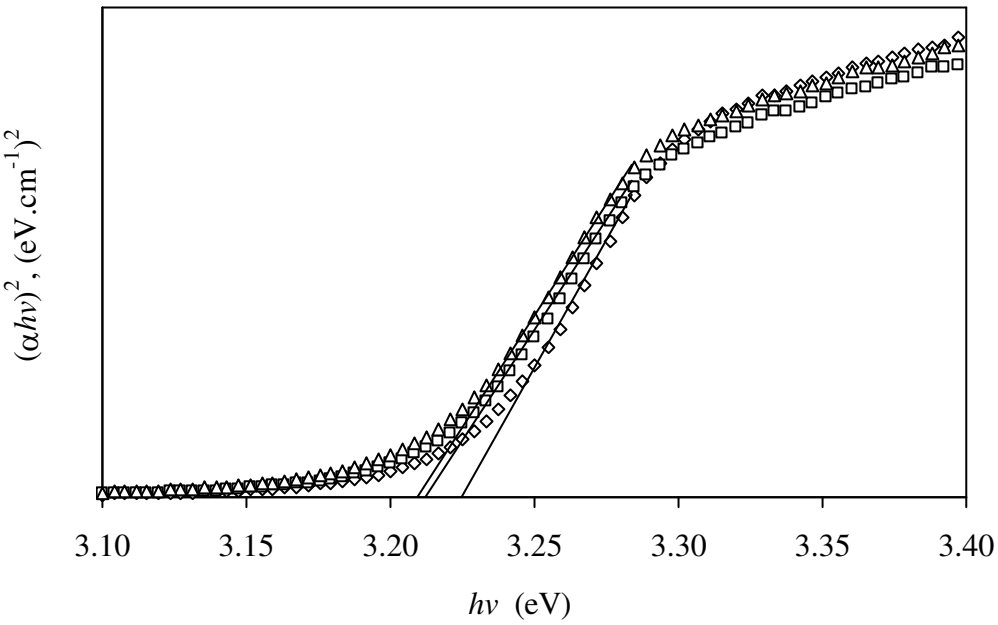

Figure 52. Evolution of $(\alpha hv)^2$ *vs. hv* of calcined ZnO particles prepared from the solution at pH 10 for 5 h. The mole ratios of Zn^{2+}:SDS are 1:0 (◇), 1:0.5 (□) and 1:1 (Δ), respectively.

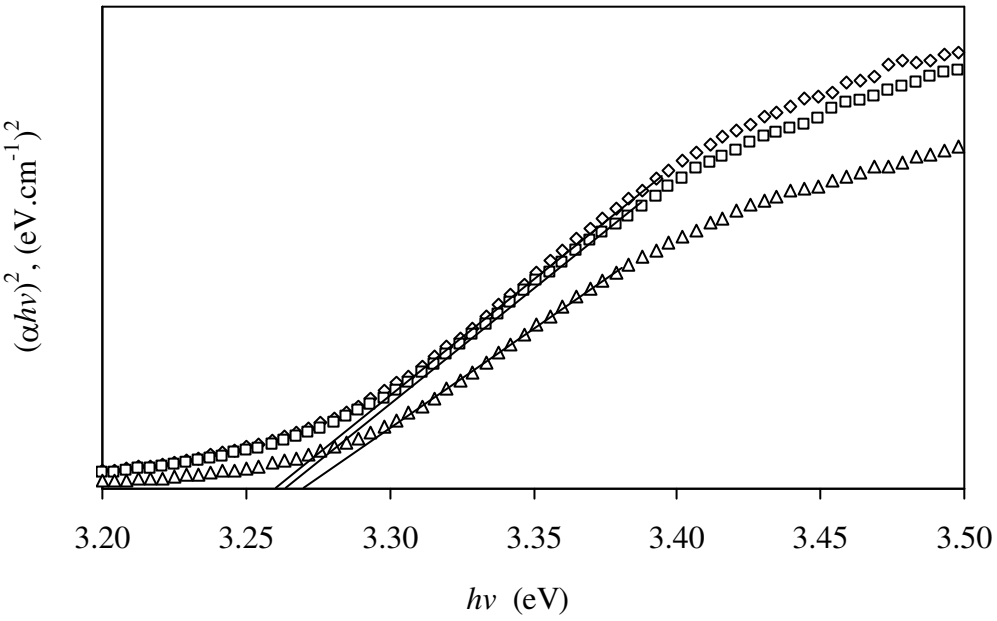

Figure 53. Evolution of $(\alpha hv)^2$ *vs. hv* of as-prepared ZnO particles prepared from the solution at pH 12 for 1 h. The mole ratios of Zn^{2+}:SDS are 1:0 (◇), 1:0.5 (□) and 1:1 (Δ), respectively.

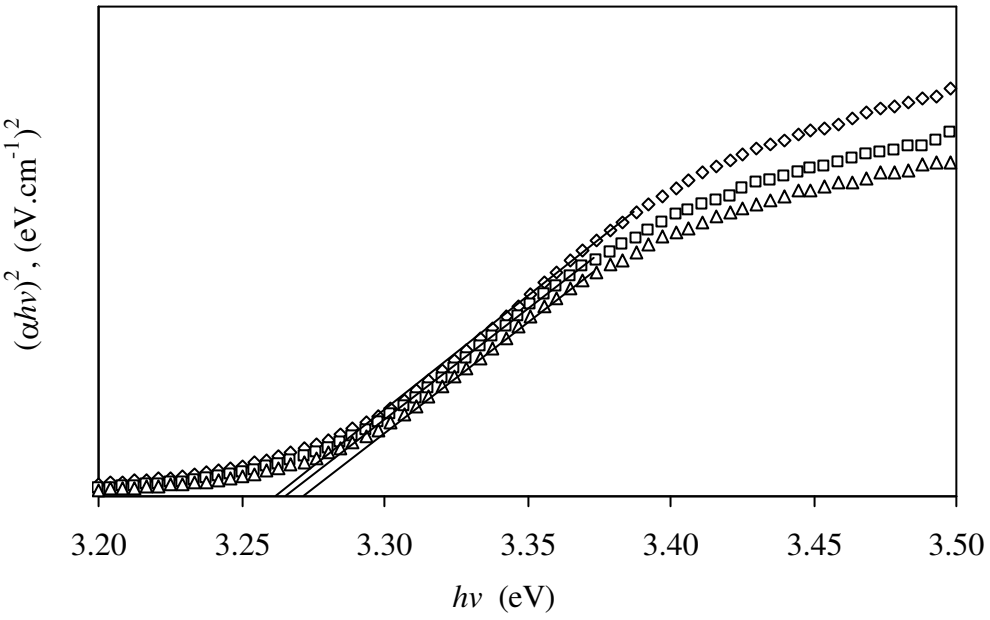

Figure 54. Evolution of $(\alpha hv)^2$ *vs. hv* of as-prepared ZnO particles prepared from the solution at pH 12 for 5 h. The mole ratios of Zn^{2+}:SDS are 1:0 (◇), 1:0.5 (□) and 1:1 (Δ), respectively.

Table 5. Estimated energy band-gap of ZnO powders.

aging time (h)	pH of solution	mole ratio of Zn^{2+}:SDS		
		1 : 0	1: 0.5	1:1
1	8	3.216	3.209	3.205
	10	3.217	3.211	3.207
	12	3.260	3.263	3.269
5	8	3.223	3.221	3.206
	10	3.224	3.213	3.209
	12	3.262	3.266	3.271

Small red-shift in E_g value was observed for calcined ZnO samples prepared from the solution at pH 8 and 10 with increasing SDS concentration. In the same condition, the blue-shift can be however observed for as-powders prepared from the solution at pH 12. These evidences may be explained by a particle size of each sample. In general, a smaller particle size generates a larger energy band-gap by a contraction of energy bands. From the ZnO samples prepared from the solution with a mole ratio of Zn^{2+}:SDS = 1:1 at pH 8 – 12, the blue-shift in absorption edge was observed for the samples prepared from solution with higher pH value due to a change in morphology and surface microstructure. The estimated band gap values of ZnO prepared from the solutions at pH 8 and 10 were in the same order of another ZnO hexagonal prism shape which was prepared by using poly(sodium 4-styrene-sulfonate) as a stabilizer (less than 3.21 eV) (Ya *et al*., 2008).

4.1.4.2. Emission spectra

In fact, ZnO shows an emission in a visible region whose it usually uses as the light emitting diodes. The emission in ZnO comes from many partways as mentioned in Chapter 1. The emission characteristics, the emission intensities of nanocrystalline ZnO powders prepared from solution modifying with different SDS concentrations and different pH values were investigated by photoluminescence spectrometer with diffuse reflectance method at room temperature. The emission intensities were measured as a function of wavelength in a range of 200-800 nm and the results were given in figure 55-61.

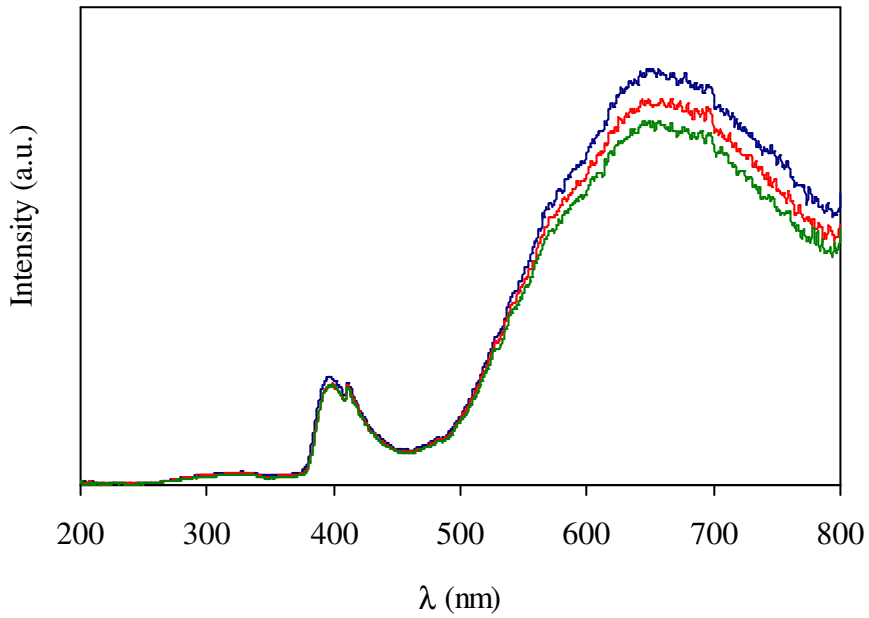

Figure 55. Room temperature PL spectra for calcined ZnO particles prepared from the solution at pH 8 for 1 h. The mole ratios of Zn^{2+}:SDS are 1:0 (blue), 1:0.5 (red) and 1:1 (green), respectively.

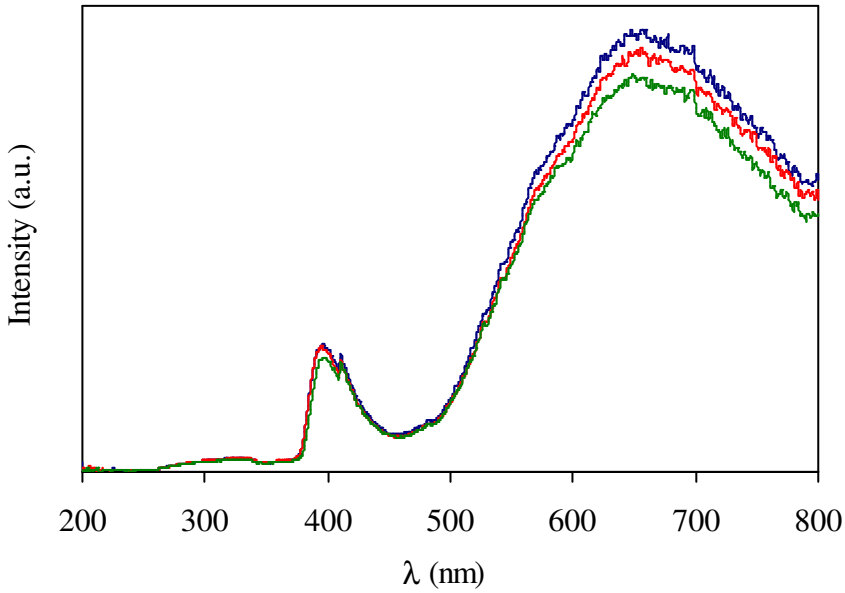

Figure 56. Room temperature PL spectra for calcined ZnO particles prepared from the solution at pH 8 for 5 h. The mole ratios of Zn^{2+}:SDS are 1:0 (blue), 1:0.5 (red) and 1:1 (green), respectively.

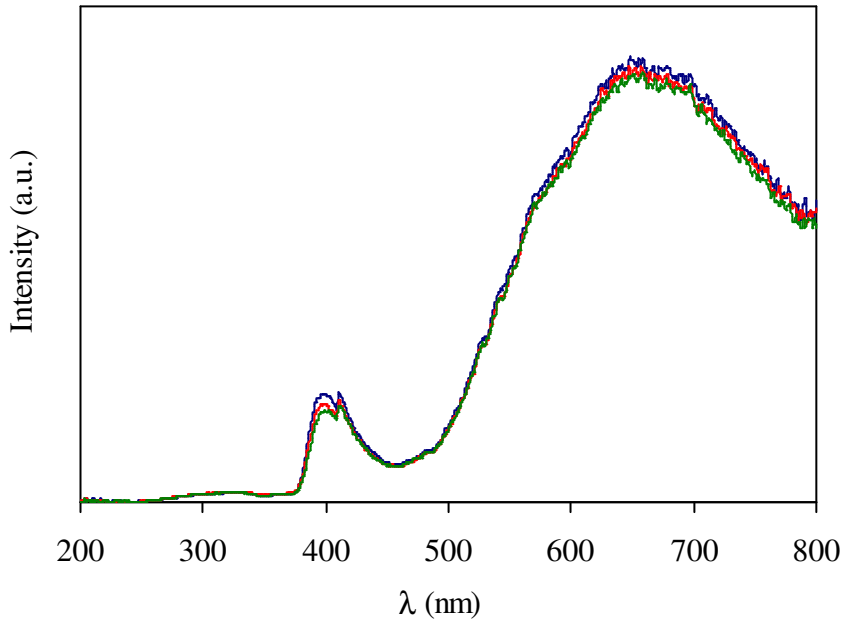

Figure 57. Room temperature PL spectra for calcined ZnO particles prepared from the solution at pH 10 for 1 h. The mole ratios of Zn^{2+}:SDS are 1:0 (blue), 1:0.5 (red) and 1:1 (green), respectively.

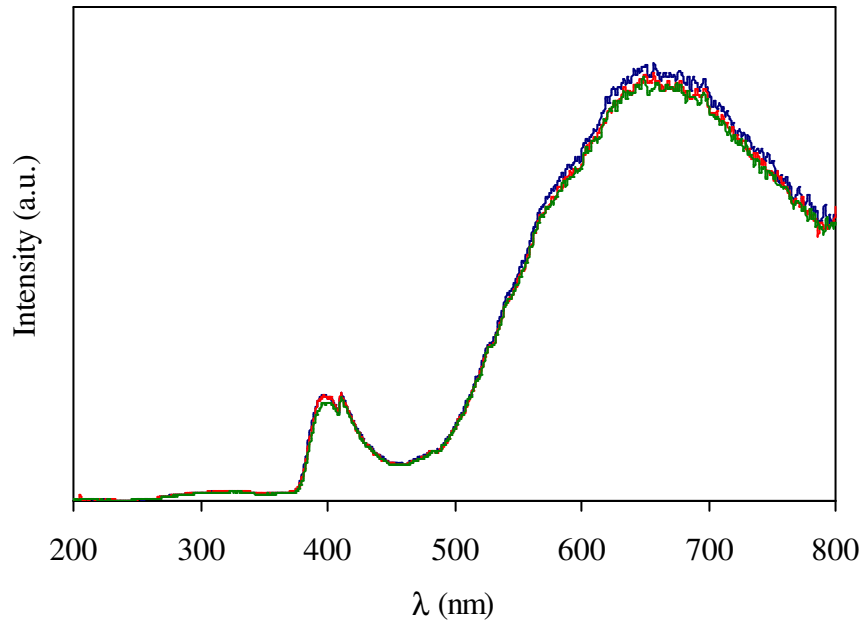

Figure 58. Room temperature PL spectra for calcined ZnO particles prepared from the solution at pH 10 for 5 h. The mole ratios of Zn^{2+}:SDS are 1:0 (blue), 1:0.5 (red) and 1:1 (green), respectively.

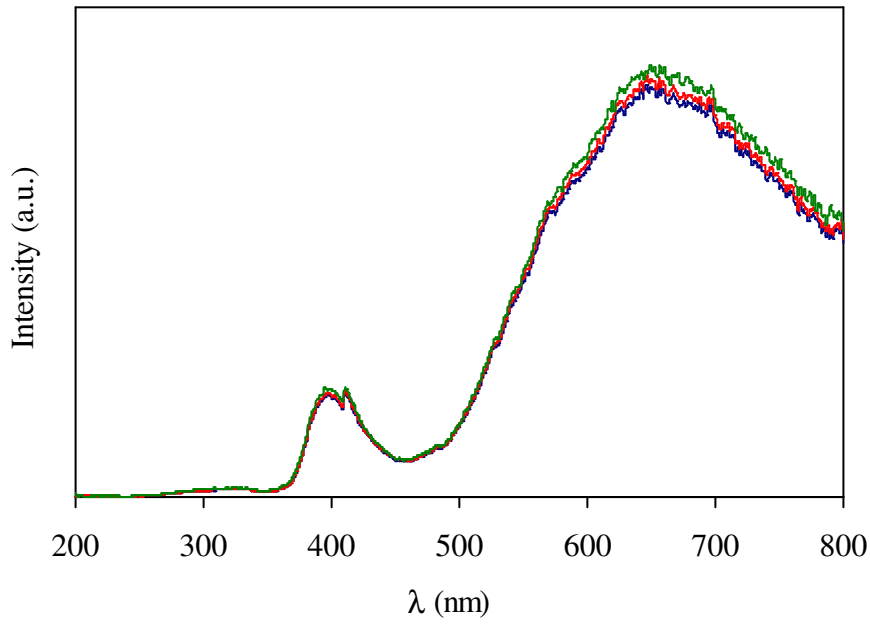

Figure 59. Room temperature PL spectra for calcined ZnO particles prepared from the solution at pH 12 for 1 h. The mole ratios of Zn^{2+}:SDS are 1:0 (blue), 1:0.5 (red) and 1:1 (green), respectively.

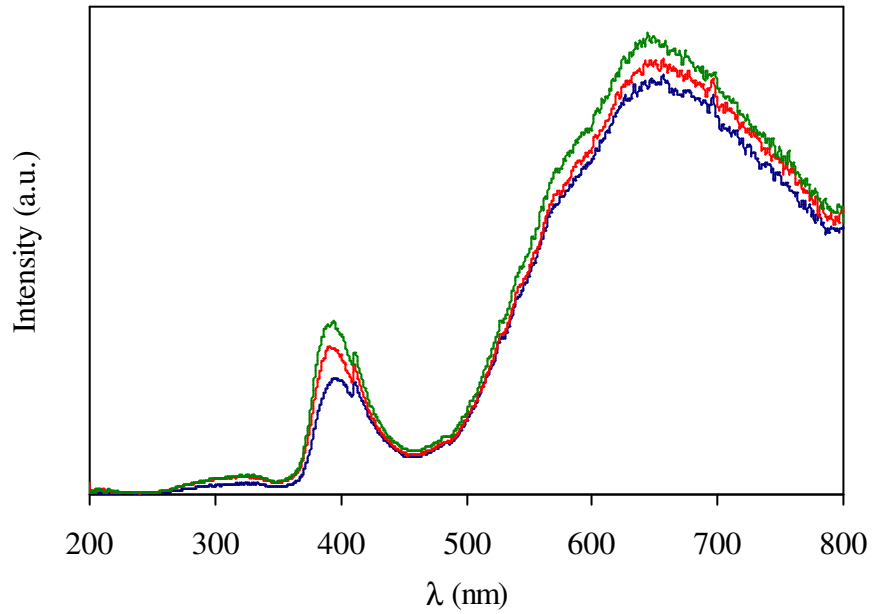

Figure 60. Room temperature PL spectra for calcined ZnO particles prepared from the solution at pH 12 for 5 h. The mole ratios of Zn^{2+}:SDS are 1:0 (blue), 1:0.5 (red) and 1:1 (green), respectively.

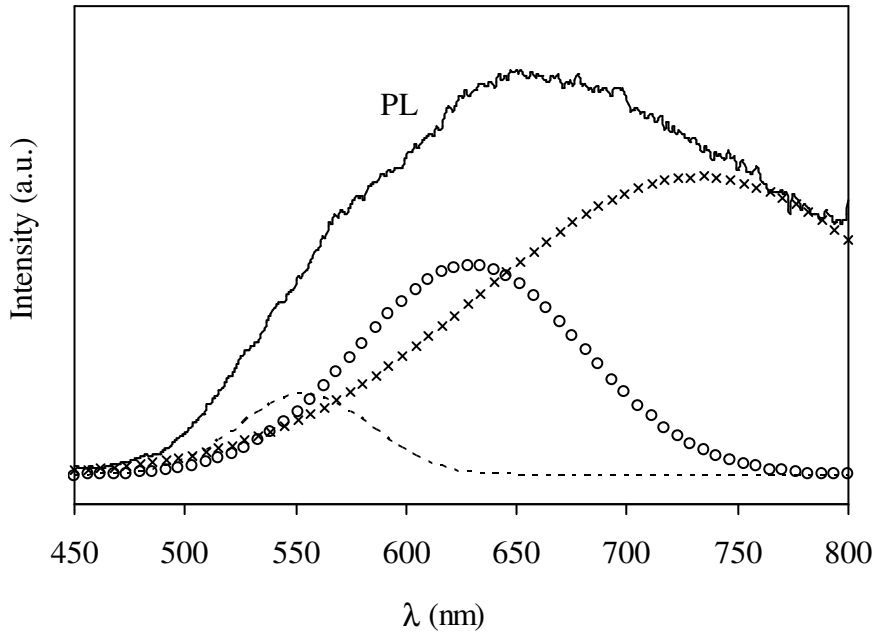

Figure 61. Deconvolution of PL band in visible region.

Figure 55 – 60 showed the room temperature PL spectra of nanocrystalline ZnO particles prepared from solution at different pH values and different concentrations. All the samples showed two emission peaks that are similar to conventional PL spectra of common ZnO particles. The UV emission centered at about 390 nm is well understood as being the near-band-edge emission, whereas the broad visible emission originated from a variety of deep level defects, e.g. oxygen vacancies and zinc interstitials. To analyze the broad band in visible region, it was deconvoluted with the Gaussian functions. The deconvoluted spectrum showed three peaks fitted at 520 nm (green emission), 625 nm (yellow emission) and 720 nm (red emission) as clearly seen in figure 61. The green band is attributed to the radiative recombination of a delocalized electron close to the conduction band with deeply trapped hole in the single-ionized oxygen vacancy (V_O^+). Both yellow and red bands have been previously associated to radiative recombination of a similar electron with deeply trapped hole in the negatively charged interstitial oxygen ion (O_i^-) (Ha *et al*., 2008). Normally, the emission in visible region is usually sensitive to oxygen defects within ZnO crystal. These defects increased with increasing a surface area of ZnO particles. From SEM images, the dimension of ZnO particles reduced with increasing pH of solution. At pH 8, a reduced emission in visible region with increasing SDS concentration can be attributed to a decrease of oxygen defects within ZnO crystal. This is because of lower surface area of larger ZnO particles when higher SDS concentration was used as observed in SEM images. The ZnO particle size prepared from the solution at pH 10 did not significantly reduced, then this emission was slightly quenched with increasing SDS concentration. But, the rod-like ZnO formed by agglomeration of many small particles performed an increase of the emission with increasing SDS concentration owing to the increase in its surface area.

4.2. Use of PEO-*b*-PPO

In this section, the concentration of PEO-*b*-PPO copolymer was fixed at 0.67 M and it was added into Zn^{2+} solution in order to study the effect of this stabilizer on morphological change of ZnO particles. In this investigation, the mole ratio of Zn^{2+}:PEO-*b*-PPO was 1:0.1 and the aging time was 1 h.

4.2.1. Structure of as-prepared ZnO powders

Unlike SDS used, all of as-samples prepared from the PEO-*b*-PPO modified $Zn(C_2H_3O_2)_2.2H_2O$ solutions showed only a single phase of ZnO after drying process at 100 ^oC for 1 h as clearly shown in figure 62. All diffraction peaks of as-powder were quite similar to hexagonal or wurtzite ZnO structure with a space group *P6₃mc* and these patterns are in good agreement with the JCPDS file number 36-1451.

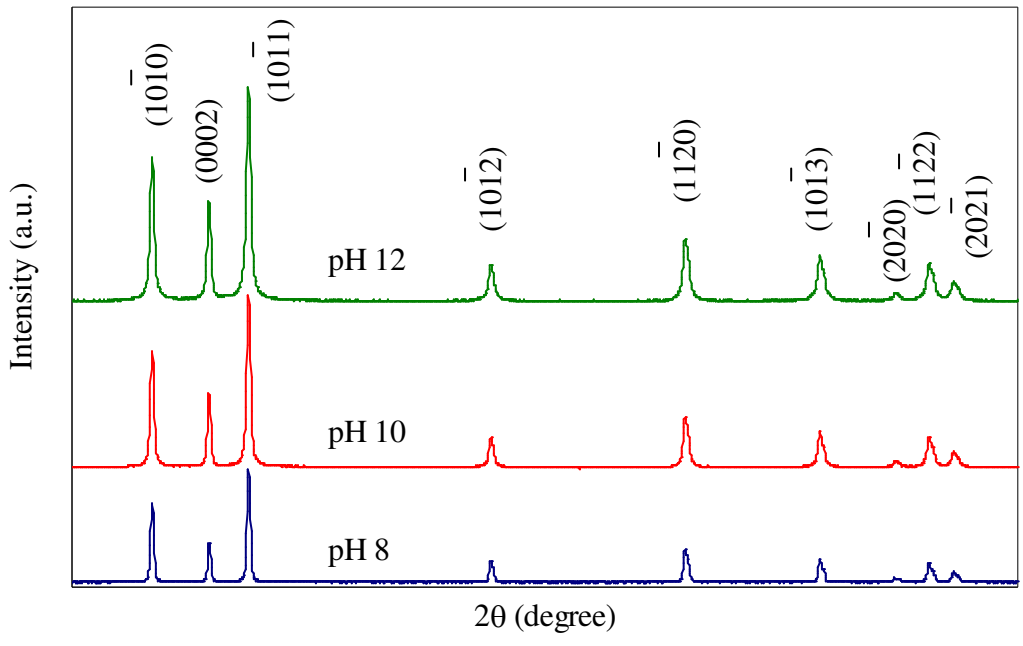

Figure 62. XRD patterns of as-prepared ZnO powders at a mole ratio of Zn^{2+}:PEO-*b*-PPO = 1:0.1 synthesized from the precursor solution at pH range of 8 -12.

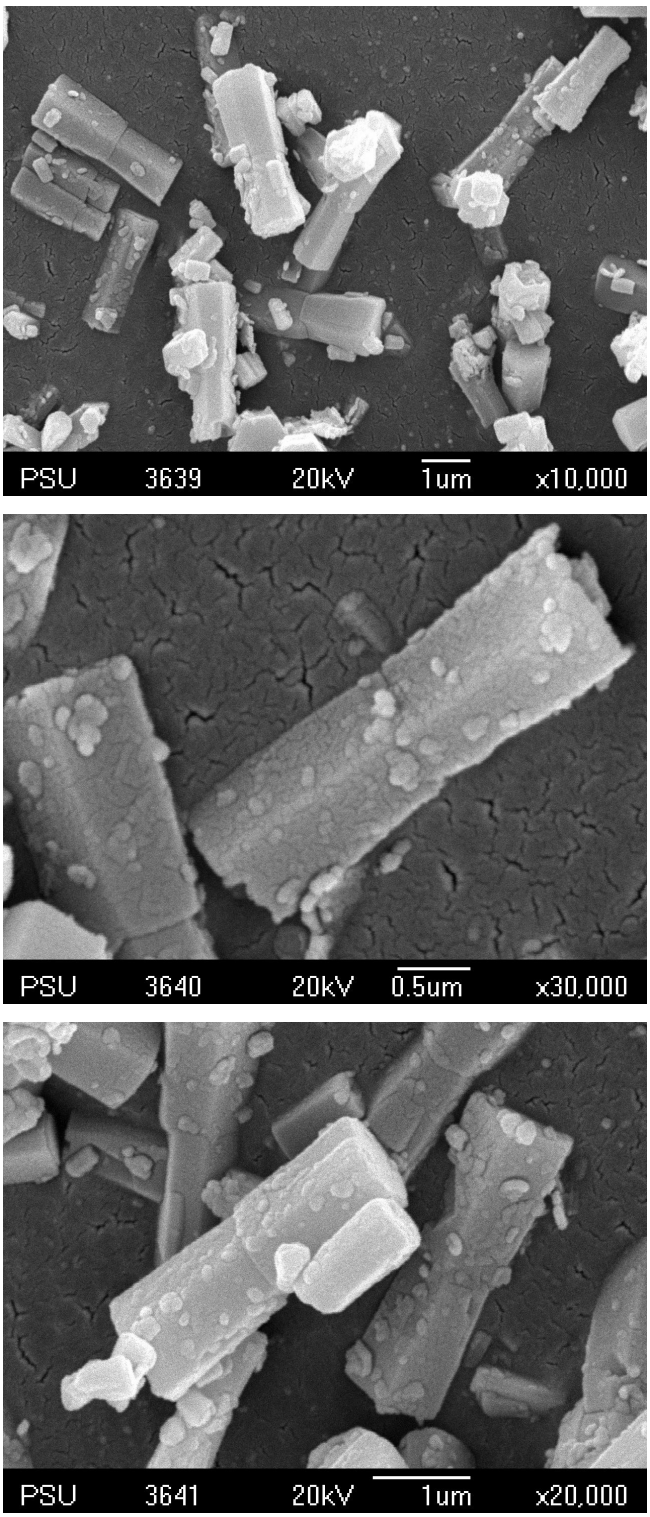

Figure 63. SEM images of as-ZnO powders prepared from the PEO-*b*-PPO modified-$Zn(C_2H_3O_2)_2.2H_2O$ solution with a mole ratio of Zn^{2+}:PEO-*b*-PPO = 1:0.1 at pH 8 and aging time for 1 h.

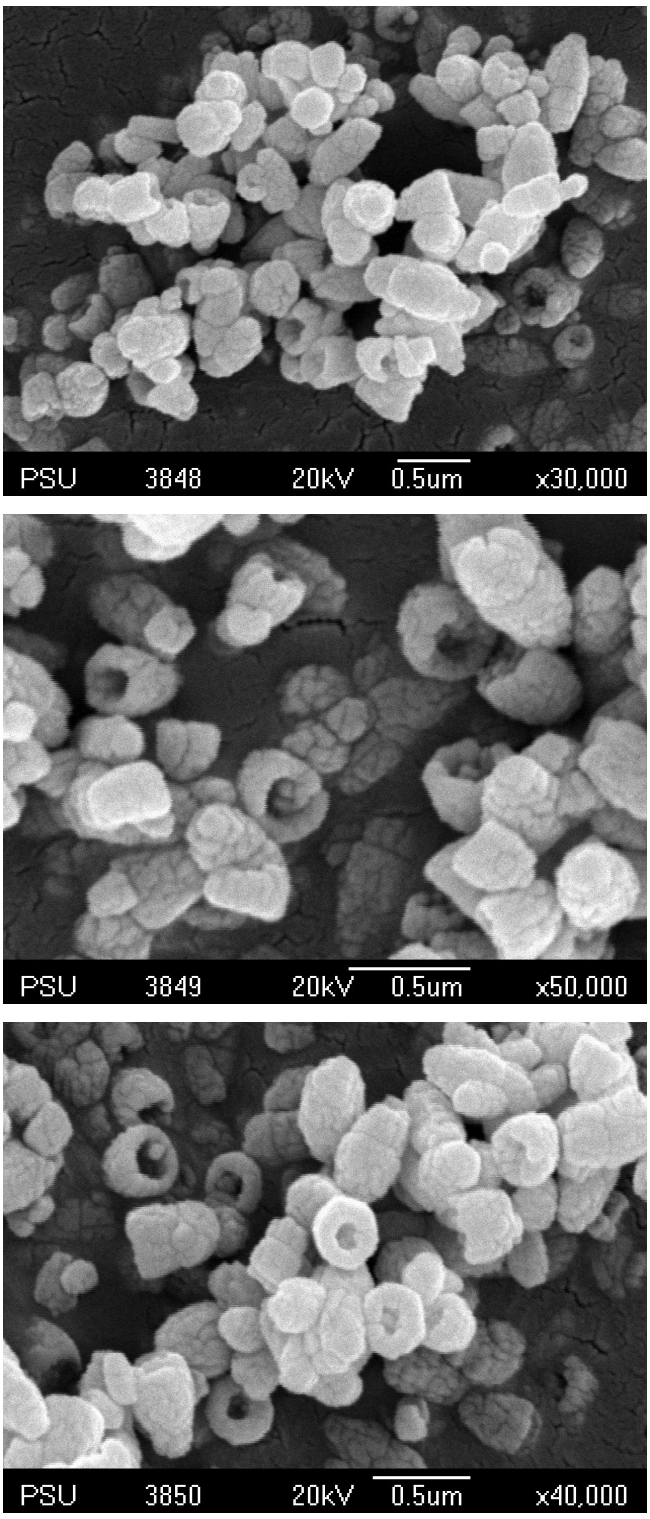

Figure 64. SEM images of as-ZnO powders prepared from the PEO-*b*-PPO modified-$Zn(C_2H_3O_2)_2.2H_2O$ solution with a mole ratio of Zn^{2+}:PEO-*b*-PPO = 1:0.1 at pH 10 and aging time for 1 h.

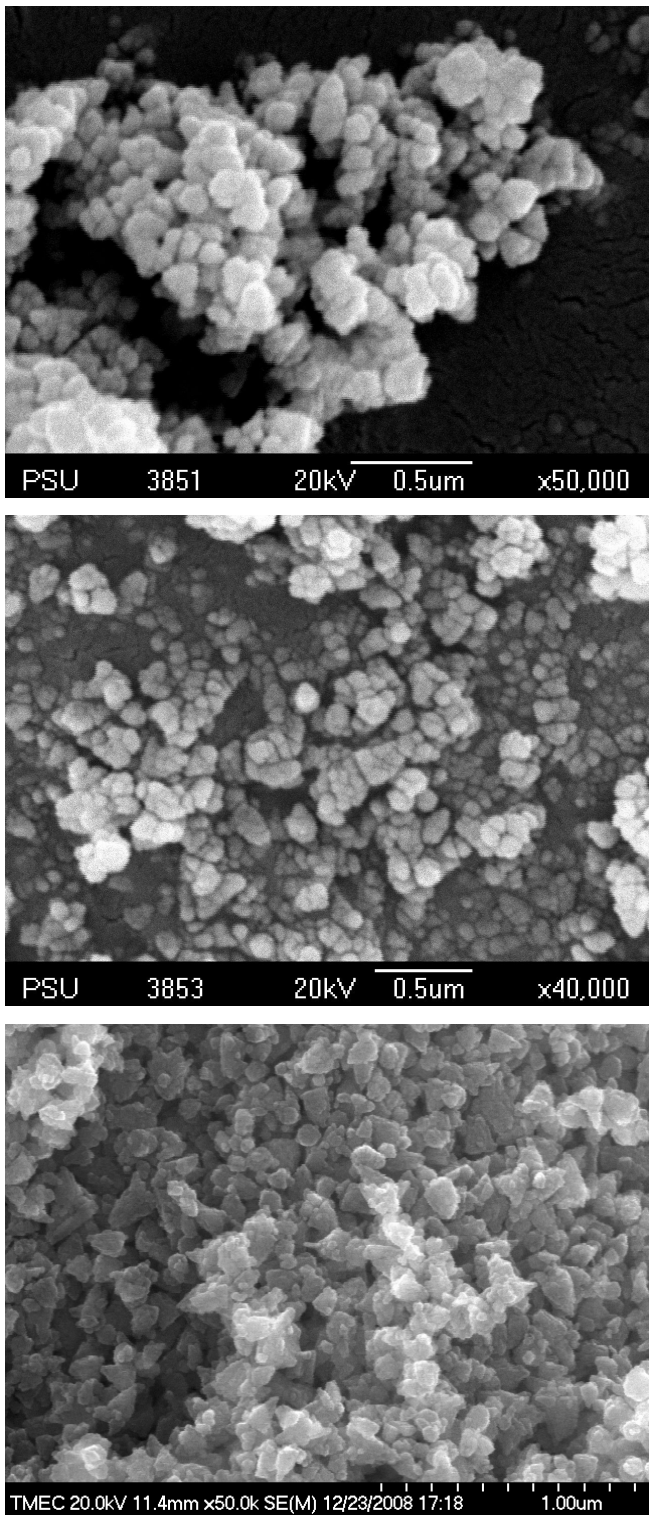

Figure 65. SEM images of as-ZnO powders prepared from the PEO-*b*-PPO modified-$Zn(C_2H_3O_2)_2.2H_2O$ solution with a mole ratio of Zn^{2+}:PEO-*b*-PPO = 1:0.1 at pH 12 and aging time for 1 h.

Base on the Scherrer's equation, the calculated crystallite size of the as-ZnO particles are 53.07 (pH 8), 45.43 (pH 10) and 33.31 (pH 12) nm in accordance with the peak broadening in figure 62. Moreover, the reduction of crystallite size with increasing a pH of solution is in accordence with the reduction of particle size observed from SEM images as presented in figure 63 – 65.

4.2.2. Morphology of as-prepared ZnO powders

Because no impurity phase was detected by XRD technique, the calcination at high temperature is not requirement for these samples. The SEM images of as-prepared ZnO powders synthesized from the PEO-*b*-PPO-modified–$Zn(C_2H_3O_2)_2.2H_2O$ solution with a mole ratio of Zn^{2+}:PEO-*b*-PPO = 1:0.1 for 1 h were presented in figure 63 – 65. From figure 63, a hexagonal biprismatic ZnO structure was observed from the solution at pH 8. On the other hand, the as-prepared ZnO powders synthesized from the solution at pH 10 showed the rugby cone structure (Figure 64). This shape turned to a small rugby or triangle-like shape when the pH value of solution was increased to 12 (Figure 65).

4.2.3. The formation process of ZnO powders

Unlike SDS used, ZnO formed from PEO-*b*-PPO-modified–$Zn(C_2H_3O_2)_2.2H_2O$ solution at pH 8 – 12 was confirmed by XRD analysis. Using polymer or copolymer such as PVP, PEO-*b*-PMAA, PEG, PEO-PMAA-PSSH etc., as stabilizer, the hexagonal biprism shape has been usually reported. The formation of this shape was usually explained by the growth inhibition of (0001) plane. In fact, ZnO is a polar crystal and consists of a positive polar (0001) plane rich in Zn cations, a negative polar $(000\bar{1})$ plane rich in O anions, and a nonpolar $(010\bar{1})$plane (Zhang *et al*., 2008). J. Zhang *et al* proposed that PVP has N and O atoms to coordinate with Zn cations on polar (0001) plane. This adsorption occurred via the interaction between lone pair electrons of N/O atoms and the vacant orbitals of Zn cations. Like PVP, PEO-*b*-PPO can react with Zn^{2+} ions through the coordination between Zn^{2+} ions of the polar (0001) plane and the lone pair electrons on N atoms, resulting in a

formation of hexagonal biprismatic structure. When the pH value was increased, some growth species $Zn(OH)_2$ can transform to $Zn(OH)_4^{2-}$. The ZnO particles then terned to rugby cone shape. However, the growth along the *c*-direction was still retarded by PEO-*b*-PPO copolymer. At high pH value (pH 12), the dissolution of $Zn(OH)_2$ to form $Zn(OH)_4^{2-}$ in the solution became higher and increased the nucleation and growth rate of ZnO particles. Because of the faster crystallization, the smaller particles were observed.

4.2.4. Optical properties of prepared ZnO powders

4.2.4.1. Band gap estimation

To estimate the band gap value, the absorbance characteristics of nanocrystalline ZnO powders prepared from the solution modifying with PEO-*b*-PPO were investigated by a UV-Vis spectrophotometer. The absorbance behavior was measured as a function of wavelength in a range of 200-800 nm. Like a typical ZnO particles, all as-prepared ZnO powders (without calcination) showed a highly transparent mode in a visible region as shown in figure 66. From the spectra, the absorption below 400 nm was assigned to the intrinsic band gap absorption of ZnO due to the electron transition from valence band to conduction band.

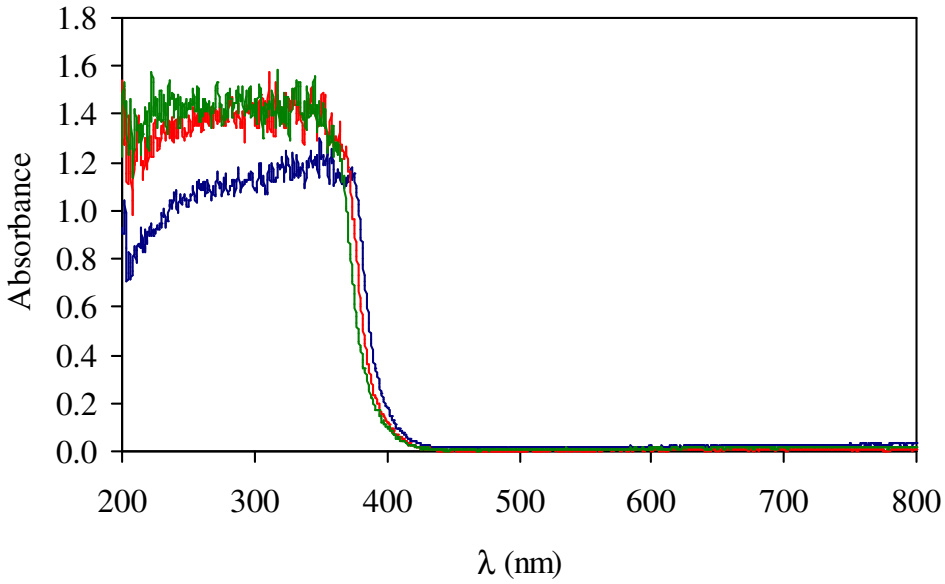

Figure 66. Absorption spectra of as-prepared ZnO powders prepared at a mole ratio of Zn^{2+}:PEO-*b*-PPO = 1:0.1 and pH 8 (blue), 10 (red) and 12 (green).

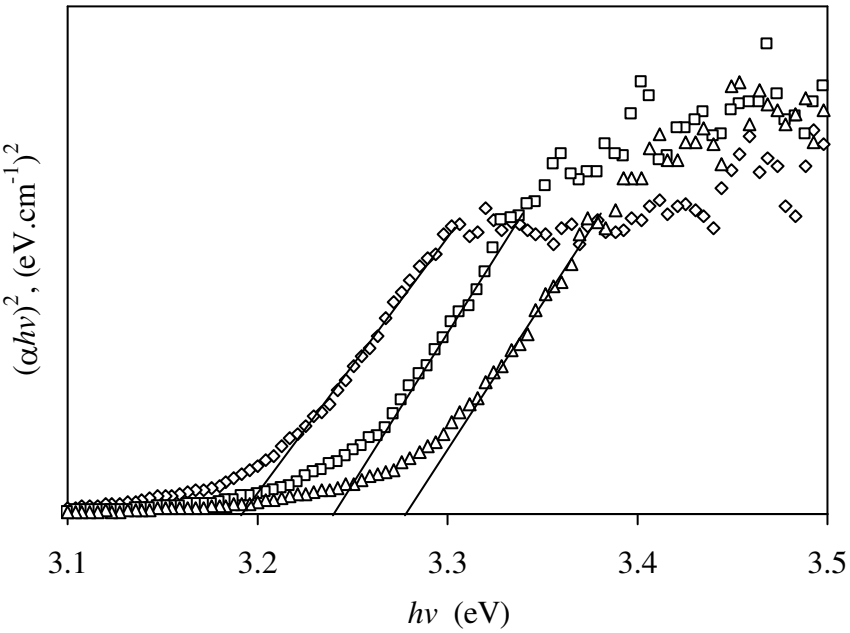

Figure 67. Evolution of $(\alpha hv)^2$ *vs. hv* of ZnO particles prepared at a mole ratio of Zn^{2+}:PEO-*b*-PPO = 1:0.1 and at pH 8 (◇), 10 (□) and 12 (Δ).

Estimated direct band-gap according to Kubelka-Munk model as mentioned in section 4.1.4.1, was calculated from a plot of $(\alpha hv)^2$ *vs.* photon energy (hv) as clearly shown in figure 67. Extrapolation of the linear part until its intersects the hv-axis gives an E_g value. The estimated band gap energies are 3.194, 3.240 and 3.268 eV for ZnO powder prepared at pH 8, 10 and 12, respectively. The blue-shift in absorption edge was observed for the samples prepared at higher pH value due to their morphological change and surface microstructure. Normally, a reduction of particle size might increase the direct band-gap due to a contraction of energy levels or energy bands.

4.2.4.2. Emission spectra

In fact, the ZnO shows an emission in a visible region whose it usually uses as the light emitting diodes. The emission of ZnO comes from many partways as mentioned in Chapter 1. The emission characteristic of synthesized ZnO from many conditions and the emission intensities of nanocrystalline ZnO powders prepared from solution modifying with PEO-*b*-PPO at different pH values were investigated by photoluminescence spectrophotometer with diffuse reflectance method at room temperature. The emission intensities were measured as a function of wavelength in a range of 200-800 nm and the result was given in figure 68.

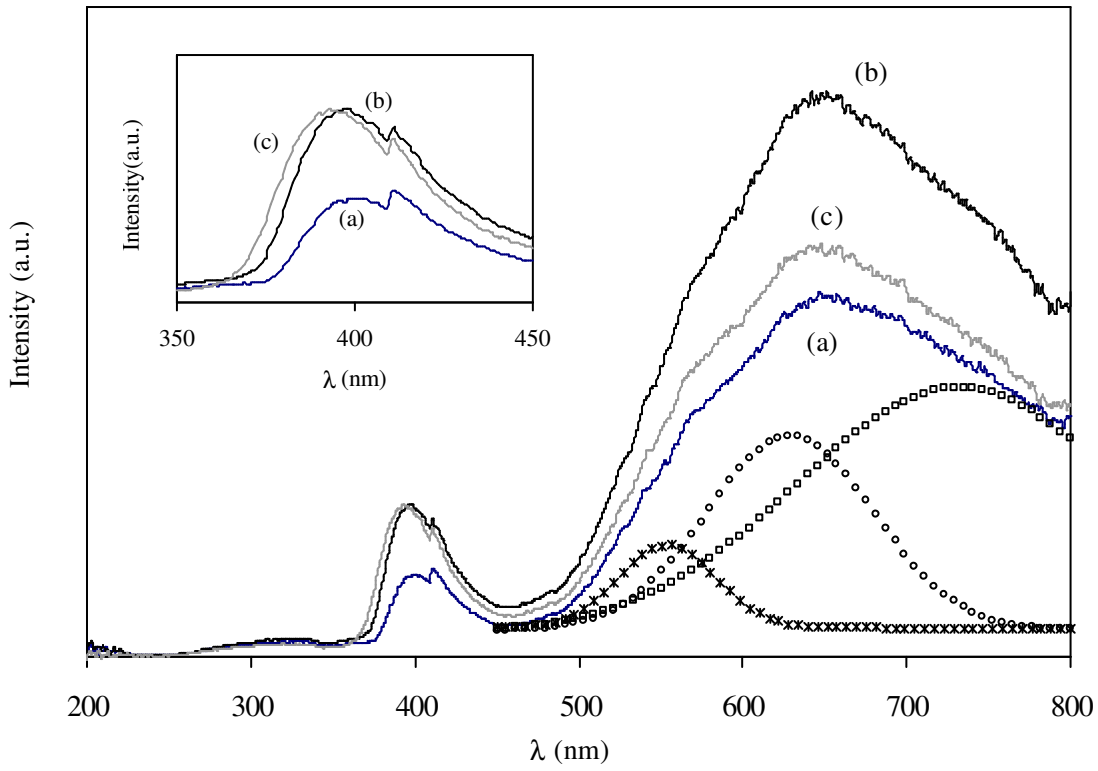

Figure 68. Room temperature PL spectra for as-prepared ZnO particles prepared at a mole ratio of Zn^{2+}:PEO-*b*-PPO = 1:0.1 and pH (a) 8, (b) 10 and (c) 12. The PL spectra of as-prepared ZnO particles exhibit three deconvolutions of defect bands.

Figure 68 showed the room temperature PL spectra of nanocrystalline ZnO particles prepared at different pH values and a mole ratio of Zn^{2+}: PEO-*b*-PPO = 1:0.1. All samples showed two emission peaks that are similar to conventional PL spectra of common ZnO particles. The UV emission centered at about 390 nm is usually referred to band edge excitonic luminescence of ZnO, whereas the broad visible emission originated from the intrinsic defects in nominally undoped ZnO, e.g. oxygen vacancies and zinc interstitials. From these samples, the UV emission peak showed a marked blue shift which corresponded to the increase of the band-edge.

Normally, the emission in visible region is usually sensitive to oxygen vacancies within ZnO crystal (Munoz-Hernandez *et al*., 2009). To analyze the broad band in visible region, it was deconvoluted with the Gaussian function. This spectrum showed three peaks fitted at 520 nm (green emission), 625 nm (yellow emission) and 720 nm (red emission) as seen in figure 61. The green band is attributed to the radiative recombination of a delocalized electron close to the conduction band with deeply trapped hole in the single-ionized oxygen vacancy (V_O^+). Both yellow and red bands had been associated to radiative recombination of a similar electron with deeply trapped hole in the negatively charged interstitial oxygen ion (O_i^-) (Ha *et al*., 2008). Normally, the emission in visible region is usually sensitive to oxygen defects within ZnO crystal. These defects were increased with increasing the surface area of ZnO particles. From SEM images, the morphology of prepared ZnO particles changed from the bi-prism (pH 8) to rugby corn (pH 10) and triangle (12) shape. This evidence can increase the surface area of ZnO particles. Therefore, the more oxygen defects could generate in ZnO prepared from the solution at higher pH, giving rise to an increase of intensity of visible emission. At pH 10, the rugby cone constructed from the agglomeration of small particles and gave the highest surface area. Then, the highest intensity of visible emission was observed for this sample.

CHAPTER 5

CONCLUSIONS

ZnO particles were synthesized through a hydrolysis of zinc acetate dihydrate at 70 ^{o}C in the presence of two stabilizers: sodium dodecyl sulfate or poly(ethylene oxide)-block-poly(propylene oxide) copolymer and pH range was 8-12.

In case of SDS used, only as-sample obtained from the solution at pH 12 showed a single phase of wurtzite ZnO structure while the other as-prepared products showed the mixed phase of both ZnO and $Zn(OH)_2$. At pH 8 and 10, the rate of $Zn(OH)_2$ dissolution to form ZnO particles was inhibited by the adsorption of SDS molecules on $Zn(OH)_2$ surface. However, these stabilized species decreased as a function of pH and only a single ZnO phase was found at pH 12. The characteristic of the vibrational frequency of SDS can be found from the as-samples prepared at pH 8 and 10 only. This can confirm that SDS could adsorb on $Zn(OH)_2$ surface. However, no SDS signal was detected from the as-prepared samples synthesized at pH = 12. The blue-shift in the absorption edge was observed for the ZnO powders prepared at higher pH value due to their morphological change and surface microstructure. The diameter of the hexagonal face decreased with increasing pH value and they changed to a rod-like shape (agglomerated by sphere-like shape) indicating that the surface area of particles could increase. With a higher surface area, the photogenerated holes in the valence band were possibly trapped into the surface defects and increasingly returned to oxygen vacancies. Therefore, the intensity of the emission in the visible region increased with the increase of the surface area or also increase as a function of pH.

For PEO-*b*-PPO copolymer, all as-prepared ZnO powders synthesized from the solutions at a mole ratio of Zn^{2+}:PEO-*b*-PPO = 1:0.1 and a pH range of 8 – 12 showed all diffraction peaks of the hexagonal or wurtzite ZnO structure. The ZnO shape tended to form a biprimatic structure at pH 8, a rugby cone structure at pH 10 and triangle-like shape at pH 12. The UV-Vis spectra showed an absorption band

edge shifted to a shorter wavelength in accordance with an increase of band-gap value owing to the reduction in the particle size. At pH 10, the as-prepared ZnO powders exhibited a strongest PL intensity in a visible region. The rugby cone structure performed a very high surface area, giving rise to an increase of oxygen defects in ZnO crystals.

REFERENCES

Bai, P., Wu, P., Yan, Z., Zhou, J. and Zhao, X. - S. 2007. Self-Assembly of Clewlike ZnO Superstructures in the Presence of Copolymer. J. Phys. Chem. C. 111: 9729-9733.

Cao, G. 2004. Nanostructures & Nanomaterials: Synthesis. Properties & applications. Imperial College Press, London.UK.

Chen, Y. and McIntyre, P.-C. 2007. Lead Zirconate Titanate Ferroelectric Thin Film Capacitors: Effects of Surface Treatments on Ferroelectric Properties. Appl. Phys. Lett. 91:72910.

Degen, A. and Kosec, M. 2000. Effect of pH and impurities on the surface charge of zinc oxide in aqueous solution. Journal of the European Ceramic Society 20: 667-673.

Freepatentsonline. 2007. Zinc oxide based formulation for preventing and treating diarrhea in farm animals (online). Available http://www.freepatentsonline.com/EP1593381.html (15 October 2008)

Gan, X., Gao, X., Qiu, J. and Li, X. 2008. Growth and characterization of ZnO-SDS hybrid thin films prepared by electrochemical self-assembly method. Applied Surface Science. 254: 3839–3844.

GoldBamboo™. 2006. Zinc Oxide Cream, Ointment, and Paste (online). Available http://www.goldbamboo.com/topic-t4989-a1-6Zinc_Oxide.html

Goldstein, J., Newbury, D., Joy, D., Lyman, C., Echlin, P., Lifshin, E., Sawyer, L. and Michael, J. 2003. Scanning Electron Microscopy and X-Ray Microanalysis, 3rd, Springer Science.

Ha, B., Ham, H. and Lee, C.-J. 2008. Photoluminescence of ZnO nanowires dependent on O_2 and Ar annealing. Journal of Physics and Chemistry of Solids. 69: 2453– 2456.

Hammond, C. 1990. Introduction to Crystallography. Oxford University Press. New york. US.

Holister. P., Weener, J.w., Vas, C.R., and Harper, T. 2003. Nanoparticles; Technology White Papers nn 3. Clientifca.

Hsiao, C.C., Huang, K.-Y. and Hu, Y.-C. 2008. Fabrication of a ZnO Pyroelectric Sensor. Sensors. 8: 185-192.

Jenkins, R. and Snyder, R.-L. 1996. Introduction to x-ray powder diffractometry. John Wiley & Sons, Inc. New York.

Jitianu, M. and Goia, D.-V. 2007. Zinc oxide colloids with controlled size, shape, and structure. Journal of Colloid and Interface Science. 309: 78–85.

Joel, A.- J., John, J.- H., Robert, A.- M., Paul, M.- B. and Michael, S.- D. 2003. A multiple-scattering model analysis of zinc oxide pigment for spacecraft thermal control coatings. CAT.INIST (online). Available (http://cat.inist.fr/?aModele=afficheN&cpsidt=15369294)

Kim, G.-S., Ansari, S.-G., Seo, H. –K., Kim, Y.-S., Yang, O.-B. and Shin, H.-S. 2007. Hydrothermal growth of ZnO on annealed electrodeposited titanate film : Influence of zinc nitrate and methenamine. Applied Surface Science. 253: 7197–7202.

Li, P., Liu, H., Xu, F.-X. and Wei, Y. 2008. Controllable growth of ZnO nanowhiskers by a simple solution route. Materials Chemistry and Physics. 112: 393–397.

Li, P., Liu, H., Zhang, Y.–F., Wei,Y. and Wang, X.-K. 2007. Synthesis of flower-like ZnO microstructures via a simple solution route. Materials Chemistry and Physics 106: 63–69.

Li, P., Wei, Y., Lin, H. and Wang, X.-K. 2005. Growth of well-defined ZnO microparticles with additives from aqueous solution. J. Solid State Chem. 178: 855-860.

Li, W.-J., Shi, E.-W., Zhoug, W.-Z. and Yin, Z.-W. J. 1999. Growth mechanism and growth habit of oxide crystals. Cryst. Growth. 203: 186-196.

LUMINESCENCE SPECTROPHOTOMETER. LS55 Users Guide. 2000. Perkin Elmer Inc. UK.

Lyu, S.-C., Zhang, Y., Ruh, H., Lee, H. –J., Shim, H.-W., Suh, E.-K. and Lee, C.-J. 2002. Low temperature growth and photoluminescence of well-aligned zinc oxide nanowires. Chemical Physics Letters 363: 134–138.

Majumder, S.B., Jain, M., Dobal, P.S. and Katiyar, R.S. 2003. Investigations on solution derived aluminium doped zinc oxide thin films. Materials Science and Engineering B. 103: 16-25.

Michaelis, E., Wohrle, D., Rathousky, J. and Wark, M. 2006. Electrodeposition of porous zinc oxide electrodes in the presence of sodium laurylsulfate. Thin Solid Films. 497: 163 – 169.

Mungkornasawakul, P., Rattanakit, N., Sirita, J., Plikomol, A., Sripuan, T., Ounnunkad, S. and Phanichphant, S. 2005. ANTIMICROBIAL ZINC OXIDE NANOPOWDERS. 31st Congress on Science and Technology of Thailand at Suranaree University of Teachnology. 18-20 October 2005.

Munoz-Hernandez, G., Escobedo-Morales, A. and Pal., U. 2009. Thermolytic Growth of ZnO Nanocrystals: Morphology Control and Optical Properties. Crystal Growth & Design. 9: 297-300.

Nav Bharat Metalic Oxide Industries Pvt. Limited. 1978. Our company enjoys a highly diversified clientele. Some of the popular applications of Zinc Oxide are in the following industries: (online). Available http://navbharat.co.in/clients.htm (15 October 2008)

Ni, Y., Wu, G., Zhang, X., Cao, X., Hu, G., Tao, A., Yang, Z. and Wei, X. 2008. Hydrothermal preparation, characterization and property research of flowerlike ZnO nanocrystals built up by nanoflakes. Materials Research Bulletin 43: 2919–2928.

Northern Arizona University. 2006. Planetary Materials Microanalysis Facility (online). Available www4.nau.edu/.../Microprobe-SEM/Signals.html (24 October 2008)

OHBA Laboratory. (online) Available http://www.geocities.jp/ohba_ lab_ ob_ page/ Structure/ZnO_Wurtzite.jpg (19 October 2008)

Oner, M. 1998. Control of ZnO Crystallization by a PEO-b-PMAA Diblock Copolymer. Chem. Mater. 10: 460-463.

Qteish, A. 2000. Self-interaction-corrected local density approximation pseudopotential calculations of the structural phase transformations of ZnO and ZnS under high pressure. J. Phys.: Condens. Matter 12: 5639-5653.

Ratana, T., Amornpitoksuk, P. and Suwanboon, S. 2009. The wide band gap of highly oriented nanocrystalline Al doped ZnO thin films from sol–gel dip coating. Journal of Alloys and Compounds. 470: 408–412.

Samontha, A., Shiowatana, J. and Siripinyanond A. Elemental Size Characterization Of Cosmetic Products Using Sedimentation Field-Flow Fractionation With Inductively Coupled Plasma-Mass Spectrometry. Department of Chemistry. Faculty of Science. Mahidol University: Rama 6 Road. Bangkok. Thailand.

Scintag, Inc.1999. Chapter 7: Basics of X-ray Diffraction (online). Available http://epswww.unm.edu/xrd/xrdbasics.pdf (15 October 2008)

Serpone, N., Lawless, D. and Khairutdinov, R.1995. Size Effects on the Photophysical Properties of Colloidal Anatase TiO_2 Particles: Size Quantization versus Direct Transitions in This Indirect Semiconductor. J. Phys. Chem. 99: 16646-16654.

Serrano, J., Romero, A.-H., Manjon, F.-S., Lauck, R., Cardona, M. And Rubio, A. 2004. Pressure dependence of the lattice dynamics of ZnO: An *ab initio* approach. Physical Review B. 69, 094306: 9.

Singh, S.-C. and Gopal, R. 2008. Laser Irradiance and Wavelength-Dependent Compositional Evolution of Inorganic ZnO and ZnOOH/Organic SDS Nanocomposite Material. J. Phys. Chem. C. 112: 2812-2819.

Sun, G. Cao, M, Wang, Y., Hu, C., Liu, Y., Ren, L. and Pu, Z. 2006. Anionic surfactant-assisted hydrothermal synthesis of high-aspect-ratio ZnO nanowires and their photoluminescence property. Mater. Lett. 60: 2777-2782.

Tao, J., Chen, X., Sun, Y., Shen, Y. and Dai, N. 2008. Controllable preparation of ZnO hollow microspheres by self-assembled block copolymer. Colloids and Surfaces A: Physicochem. Eng. Aspects. 330: 67–71.

U.S. Geological Survey. 2008. (online). Available http://pubs.usgs.gov/of/2001/of01-041/htmldocs/images/xrdschem.jpg (30 October 2008)

U.S. Geological Survey. 2008. (online). Available http://pubs.usgs.gov/of/2001/of01-041/htmldocs/images/xrdtube.jpg (30 October 2008)

Usui, H. 2009. Surfactant concentration dependence of structure and photocatalytic properties of zinc oxide rods prepared using chemical synthesis in aqueous solutions. Journal of Colloid and Interface Science. 336: 667–674.

Valeur, B. 2002. Molecular Fluorescence: Principles and Applications. Wiley VCH. German.

Wahab, R., Ansari, S.-G., Kim, Y.-S., Dar, M.-A. and Shin, H.-S. 2007. Synthesis and characterization of hydrozincite and its conversion into zinc oxide nanoparticles. Journal of Alloys and Compounds xxx: xxx–xxx.

Wikipedia Common. 2009. File: Bragg diffraction.png. (online) Available http://commons.wikimedia.org/wiki/File:Bragg_diffraction.png (31 June 2009)

Wikipedia Foundation, Inc. 2008. Scanning electron microscope (online) Available http://en.wikipedia.org/wiki/Scanning_electron_microscope10/11/2008 (15 Octorber 2008)

Wikipedia Foundation, Inc. 2008. Zinc oxide (online). Avaliable http://en.wikipedia.org/wiki/zinc-oxide (15 October 2008)

Xiao, Q., Huang, S., Zhang, J., Xiao, C. and Tan, X. 2008. Sonochemical synthesis of ZnO nanosheet. Journal of Alloys and Compounds. 459: L18–L22.

Xie, J., Li, P., Wang, Y. and Wei, Y. 2008. Synthesis of needle- and flower-like ZnO microstructures by a simple aqueous solution route. Journal of Physics and Chemistry of Solids. xxx: xxx-xxx.

Xinshu, N., Weiping, D. and Weimin, D. 2004. Preparation and gas sensing properties of ZnM_2O_4 (M = Fe, Co, Cr).Sensor and Actuators B. 99: 405-409.

Xu, J., Pan, Q., Shun, Y. and Tian, Z. 2000. Grain size control and gas sensing properties of ZnO gas sensor Sensors and Actuators B. 66: 277-279.

Ya, J., Li, C. and Liu, S. 2008. Effect of PSS on morphology and optical properties of ZnO. Journal of Colloid and Interface Science. 326: 433–438.

Yang, L., Yang, J., Liu, X., Zhang, Y., Wang, Y., Fan, H., Wang, D. and Lang, J. 2008. Low-temperature synthesis and characterization of ZnO quantum dots. Journal of Alloys and Compounds. 463: 92–95.

Yin, H., Xu, Z., Wang, Q., Bai, J. and Bao., H. 2005. Study of assembling ZnO nanorods into chrysanthemum-like crystals. Materials Chemistry and Physics. 91: 130–133.

Zhang, J., Liu, H., Wang, Z. and Ming, N. 2008. Low-temperature growth of ZnO with controllable shapes and band gaps. Journal of Crystal Growth 310: 2848–2853.

Zhang, Z. and Mu, J. 2007. Hydrothermal synthesis of ZnO nanobundles controlled by PEO–PPO–PEO block copolymers. Journal of Colloid and Interface Science. 307: 79–82.